Finite element simulations of excitonic solar cells and organic light emitting diodes

Williams, Jonathan

Award date:
2008

Awarding institution:
University of Bath

FINITE ELEMENT SIMULATIONS OF EXCITONIC SOLAR CELLS AND ORGANIC LIGHT EMITTING DIODES

J. H. T. Williams, University of Bath

A thesis submitted for the degree of Doctor of Philosophy

University of Bath
Department of Physics

January 2008

Abstract

This work describes the simulation of excitonic solar cells and organic light emitting diodes using the Finite Element Method.

Although solar cells and light emitting diodes have different functions, the former is the time reversal of the latter. This equivalence enables these seemingly disparate functional devices to be simulated analogously. Solar cells based on organic polymers as well as dye-sensitised titanium dioxide are considered and remarkably, these can also be described using a common physical basis, termed the excitonic solar cell. This description accounts for the fact the generation profile of charge carriers in excitonic solar cells is different to that in conventional solar cells such as those made from silicon p-n junctions.

Part I investigates two related timescales relevant to the dye-sensitised solar cell and compares a simple analytical model to the numerical simulations under fast extraction conditions. The transport time is shown to be well described numerically, however, the photovoltage rise time was not successfully obtained and the grounds for this discrepancy are investigated.

Part II surveys devices based on organic materials. Firstly, a parametric study of solar cells with a complex inter-digitated structure are considered and are consistently shown to be limited by low charge transport efficiencies and space charge effects at high illumination intensity. In addition, the open circuit voltage in these devices is described by specified deviations from the built-in voltage. Secondly, experimental current-voltage characteristics of organic light emitting diodes (OLEDs) made from organic dendrimers are simulated. Distinct regions of the dendrimer molecule control different material properties, thus making them ideal candidates for future device applications where different attributes can be separately optimised. The simulations show that the Mott-Schottky model - describing the charge injection barrier height from a metallic electrode - is not adhered to in devices which are prepared and tested under ambient conditions.

Acknowledgments

First and foremost, I would like to thank my PhD advisor Alison Walker for her guidance throughout the course of this work. The project would not have been possible without her broad knowledge and willingness to answer questions.

I thank Adrian Hooper at the University of Bath for his efforts to get the **COMSOL** software working appropriately and to Jenny Nelson at Imperial College London for introducing me to the physics of organic solar cells. My main collaborator throughout the work on the dendrimer OLEDs has been Stuart Stevenson at the University of St Andrews and I must certainly give him and his advisor Ifor Samuel a special mention.

The modelling of the dye-sensitised solar cells was performed in collaboration with Halina Dunn and her advisor Laurie Peter in the Department of Chemistry at this University and I would like to thank them for giving me a chemist's and experimentalist's point of view.

I would also like to thank all the past and present members of the Device Modelling group in the Department of Physics.

Finally I thank all my family and friends, specifically to Frances Ansell for proof reading and to Phil Horner.

Contents

Chapter 1

Introduction

1.1 Preamble

This thesis is concerned with the simulation of novel functional devices. That is, solar cells and light emitting diodes which are not based on highly pure crystalline semiconductors such as silicon and gallium arsenide. Although the majority of the results reported here will be concerned with organic solids alone, work on photoelectrochemical systems based on hybrid organic/inorganic systems containing titanium dioxide (TiO_2) will be discussed also.

The prototypical electronic device is the inorganic p-n junction, comprising two pieces of semiconductor in contact with one another, one with a net positive charge and one with a net negative charge [1]. This simple structure forms the basis of many modern electronic devices including solar cells [2]. In the last two decades however, there has been a surge of interest in making devices from materials utilising organic solids such as polymers [3, 4] and also inorganic photoelectrochemical systems. The Grätzel solar cell is a frequently cited example of the latter [5, 6].

World energy use is rising inexorably. For example, total consumption rose from roughly 47 quads (1 quad is equal to 2.9×10^{11}kWh) in 2000 to just over 53 quads in 2004 according to the US Department of Energy. This is an incredible rise considering the value in 1980 was just 25.5 quads [7]. However, even in 2005, only 0.06% of the energy production of America (the world's largest consumer) came from photovoltaic sources. This compares with 0.12% from wind and 2.7% from hydroelectric sources [8]. These figures seem absurdly small when compared with the amount of solar radiation incident on the surface of the Earth, at 125,000TW [9]. This shows that the Sun

supplies enough energy to the Earth in approximately 7 minutes to provide all the electrical power currently used in one year. Solar cells are a potential route to generating electricity more sustainably but should be considered as a part of the solution rather than as a panacea for the World's energy problems.

Another route to reduce energy usage is to use more efficient electrical devices such as displays and light-emitting diodes, LEDs. For example, in America, lighting is the single largest burden on the energy budget, accounting for 30% of the electricity consumed in 2001 [10]. Solid state lighting (using the light-emitting properties of semiconductors) offers the potential to produce light with considerably higher efficiency than traditional fluorescent and incandescent sources. For example the standard filament light bulb has an efficiency of between 1-4% compared to LED efficiency of between 20-50% [11]. Other advantages of these systems include lifetimes of up to 100 times greater than tungsten based bulbs, toughness which comes from containing no glass and the possibility of using up to 90% less electricity than traditional sources of light [11].

1.2 Photovoltaics

The discovery of the photovoltaic effect is widely attributed to Edmund Becquerel in 1839 when he observed a photocurrent in silver coated platinum in aqueous solution [2, 12, 13]. It is now known that Becquerel had observed a photoelectrochemical effect, although the net result was the same [12]. Selenium was the next material to have noted photovoltaic properties, as discovered by Adams and Day in 1877, although again it was its photoconductivity which was discovered first [12, 13]. In the years that followed, the photovoltaic effect was also noted in many other materials such as cuprous oxides, lead sulphide and thallium sulphide. The photoconductive properties of selenium-based materials, (where the current passed is proportional to the light intensity) made it ideal for light meters and in 1885, the German industrialist Werner von Siemens was quoted as saying that his research had demonstrated ...

> "...for the first time, the direct conversion of the energy of light into electrical energy [12]."

The photoconductive properties of these early materials initially excited researchers because the possible applications in light meters meant the devices could work without a separate battery [2].

One common feature of these early photoactivated devices was the existence of an energy barrier at the metal-semiconductor interface. However, it was not until the 1930s that the modern theory of these interfaces was developed by Mott, Schottky and others [2] and they are now universally known as Schottky contacts. Before this time it was thought that a third interlayer of low conductivity (for example, an oxide) could have been responsible for the observed rectifying action [12]. Schottky contacts were found to be poor photoconverters however due to their large dark currents [12]. Semiconductor-semiconductor junction devices have lower dark currents and it was the development of this technology that lead to the subsequent rapid improvement in device efficiency.

As with the transistor (invented in 1947 [1]) the development of the modern p-n junction solar cell began at Bell Laboratories in America. In 1954 Chapin *et al.* reported a 6% power conversion efficiency, a huge improvement on the previous best result of just 1% from thermoelectric junction devices [14]. This research grew out of the need for extra-terrestrial power generation for the American space programme, then at its very early stages [12]. Also in 1954, a 6% efficient cadmium sulphide p-n junction cell was reported [13, 15] and theoretical work indicating that other material combinations could provide higher efficiencies led to work on p-n junctions made from gallium arsenide, indium phosphide and cadmium telluride. Just four years later, in 1958, the power conversion efficiency of silicon cells had increased by more than a factor of 2 to 14% [13]. None of these, however, managed to overtake silicon as the most widely used photovoltaic material, which it remains to this day. This was undoubtedly due, in part, to the parallel development of silicon for computing applications [2]. Indeed, by the turn of the millennium, the efficiency of single crystal silicon cells had increased to almost 25% [12]. Although the cost of producing electricity from photovoltaic sources has remained high throughout its development, it has opened up the possibility for producing power in a stand-alone fashion, for example, in remote locations where fossil fuel supplies may be scarce [2].

Due to the continuing high costs of silicon based solar cells (which, in 2005 still accounted for 94% of the photovoltaics market), in the last 20 years, there has been much interest in so-called second and third generation solar cell technologies [9]. In 2005, second generation cells accounted for 5.6% of the remaining photovoltaic market after first generation devices [16], where the term second generation describes so-called thin film technologies using material combinations such as cadmium telluride and cadmium selenide [2, 17]. These materials do not require the use of silicon and aim to be produced at significantly reduced cost by, for example, using non-crystalline substrates such as glass, which are not suitable for the highest efficiency first generation cells [9].

Third generation solar cells are altogether different and can be split into two further categories, IIIa and IIIb [16]. Class IIIa cells aim to generate efficiencies well above the 31% theoretical limit of a single junction device [18] by using exotic devices such as hot carrier, impact ionisation, and multiband solar cells [17]. Hot carrier devices, for example, aim to utilise the excess energy of charge carriers after photon absorption and subsequent charge generation by extracting them before they have the chance to thermalise to the band edge. In a first generation silicon device, if a photon of energy greater than the bandgap is absorbed, the excess energy of a photogenerated electron will be dissipated as heat (phonon emission) in a time of the order of femtoseconds [2] and will not be available for conversion into electrical work. Informative reviews of these generation IIIa systems are given in the work of Green [17] and Nelson [2] however these systems will not be considered further here.

Class IIIb solar cells encompass those based on organic polymers [19] as well as dye-sensitised nanocrystalline solar cells (DSSCs). The efficiency of an organic photovoltaic module should be of the order of $\sim$10% power efficient and have a lifetime of betwen 3 and 5 years to become a competitive technology [20]. Indeed, efficiencies of up to 11% have been reported for liquid electrolyte DSSCs [21]. This lifetime is considered to be akin to that of portable consumer electronics which may be powered by the solar cells in question given they can have a shelf life of over one year. The DSSC consists of titanium dioxide (TiO_2) particles as the electron transporter covered in a monolayer of light harvesting dye molecules immersed in liquid redox electrolyte [5, 21], or a solid state hole conductor [22]. The aim of these class IIIb cells is to attain relatively small efficiencies in conjunction with very low cost [16, 20]. It is these class IIIb devices which will form the majority of the work presented here. Both classes of these devices are also collectively referred to as excitonic solar cells [23], which will be discussed in detail in section 1.6.

Saturated plastics (man-made polymers) where all carbon valence electrons are taken up in covalent bonds are the most widely used materials in the world, both by volume and by weight [24]. However, it is only in the last 30 years that interest has developed in unsaturated semiconducting and metallic polymers, culminating in the 2000 Nobel Prize for chemistry, awarded to Heeger, Shirakawa and Macdiarmid

> "for their discovery and development of conductive polymers".

In a seminal paper, Chiang *et al.* demonstrated that the electrical conductivity of polyacetylene could be increased by up to 11 orders of magnitude by the addition of halogen dopants [4].

Molecular photovoltaic systems had been known since the mid 20th century [25] and frequently used the device structure of one layer of organic material contacted to electrodes with different work functions. Reference [26] provides an informative, early (1983) review. A breakthrough occurred in 1986 by the use of a *two* layer structure with a planar interface between them [27]. The realisation was that charges were being created at the interface between the layers of copper phthalocyanine and the organic perylene derivative rather than in the bulk as in inorganic solar cells. An excellent review of the development of organic solar cells can be found in the chapter by Halls and Friend in reference [12]. In 1995 another innovation was achieved by the discovery that intimate blending of two different polymers [28, 29], or a polymer with C_{60} [30] could bring about an improvement in device performance. The initial photogenerated state in an organic material is an exciton, a bound state of an electron and a hole. This state needs to be separated at a material heterojunction and its constituent charges transported to their respective electrodes. The blending of the materials means that the excitons are always generated close to an interface and are less likely to recombine before diffusing to a junction for dissociation. In the polymer-polymer blend case, a power conversion efficiency of 1% was obtained and the cell was found to be 2 or 3 orders of magnitude more efficient than a cell made up of either of the constituent polymers respectively [12].

More recently still, hybrid solar cells made from polymers intermixed with inorganic materials such as TiO_2 have been proposed [31, 32]. These offer the possibility of engineering the morphology of the device to an even greater extent to that which is possible using a bulk heterojunction. Indeed these idealised geometries have been shown to be potentially more efficient than bulk heterojunction or bilayer devices [33].

The quantification of the price of photovoltaic technology is most often considered in terms of the cost per watt, or per watt-peak. This is the power which a solar cell device will supply under standard test conditions of 1kWm^{-2} illumination intensity and a temperature of 298K [7]. The American photovoltaics industry [34] and the US Department of Energy [16] have decided on a target price of less than \$0.5/W and an efficiency of 18-20% for a competitive solar cell technology. However, in 2005, the cost of producing crystalline photovoltaic modules was still at $\sim$\$4/W, an order of magnitude too high. Even in 2007, electricity generated from solar cells is still between 6 and 16 times more expensive than that generated by coal [9].

Whether or not a specific photovoltaic technology becomes competitive in the marketplace will depend not only on the cost, but also on the efficiency and product lifetime [9, 20]. A product only succeeding in two of these will only be suitable for niche applications. This is clear in the case of silicon solar cells where the efficiency and lifetime are certainly competitive but the price has kept them out of domestic generation in the UK.

However, the German government introduced the 100,000 roofs programme in 1999 to aid in the implementation of a significant solar cell component to their electricity needs [35]. The price of electricity generated from solar cells is still high, however demand is now elastic. That is, the market has found a stage where a small change in price has a significant impact on the sales [9]. If this can be coupled to the reduction in unit cost associated with an increase in production (worldwide photovoltaic cell production is currently growing exponentially) then electricity prices of ∼$1/W are within reach for these mainly silicon based, first generation solar cells.

A solar cell functions as a "light in, electricity out" device. The reverse operation, "electricity in, light out" is the light emitting diode or LED. The development of these latter structures will now be considered.

1.3 Displays

The history of electroluminescence (the emission of light caused by a current) can be traced back to the report of the "curious phenomenon" of light emission from a silicon carbide Schottky diode in 1907 [36]. This device showed "unsymmetrical passage of current" [37]. Today this is referred to as as rectification, or diode behaviour. This was therefore the first report of a light-emitting diode, or LED. In 1928 Lossev reported the light-emitting properties of silicon carbide in more detail and performed experiments which concluded that the emission was not due to incandescence (radiation due to finite temperature) [36]. He concluded that the material was suitable for the construction of so-called "light-relays" since the light could be generated and extinguished rapidly.

The postulation and subsequent experimental realisation of semiconducting III-V compounds proved fruitful since they were found to be good optical emitters [36]. By the early 1960s, wafers of gallium arsenide were being used as substrates for epitaxial growth of p-n junctions for use in semiconductor lasers and the first reports of gallium arsenide phosphide LEDs were published [36]. Subsequent work has lead to the development of emitters across the visible spectrum with the development and patent rights of the blue laser diode providing some controversy [38]. This is a testament to the profitability and technological importance of these devices.

In the late 1980s, the modern era of the organic light emitting diode, or OLED, began [39, 40, 41], although Pope had observed electroluminescence in anthracene some 25 years earlier in 1963 [42]. The problem with these very early devices was that the driving voltages were very high (>100V). The use of considerably thinner films enabled the drive voltages to be reduced by an order of magnitude. In references [40, 41] layers of

small molecule organic materials were used, but the real breakthrough by the group of Richard Friend in Cambridge [39] was to use a single layer of an organic polymer, poly(p-phenylene vinylene) as the active layer. Displays based on conjugated polymers similar to those used in reference [39] are already being commercialised [43].

1.4 Outlook

Due to their low materials cost and ease of processing at room temperature, OLEDs and class IIIb photovoltaic devices hold much promise for future applications in consumer electronics and remote area power generation for example. It is one of the goals of these novel concepts in material design that they will be printed on flexible substrates using technology used routinely in the publishing industry. This will enable the manufacture of significantly higher numbers of cells than is currently possible using first generation technology [20]. Recent work on so-called 'supramolecular' systems aims to use materials which self-assemble into desired morphologies [44] and it is even possible to design molecules with desired properties using quantum chemical techniques [45]. Understanding the size of the bandgap of an organic polymer for example is crucial to the design of photovoltaic materials capable of absorbing a greater fraction of the Sun's rays than is currently possible [46, 47].

1.5 Physics of solar cells

The device physics pertinent to the study of solar cells is now considered. Of particular relevance are the maximum limiting efficiency of a solar energy converter and the four parameters

1. Short circuit current
2. Open circuit voltage
3. Fill factor
4. Power conversion efficiency at maximum power point

1.5.1 Limiting efficiency

The maximum efficiency of any thermodynamic heat engine is that of the Carnot cycle,

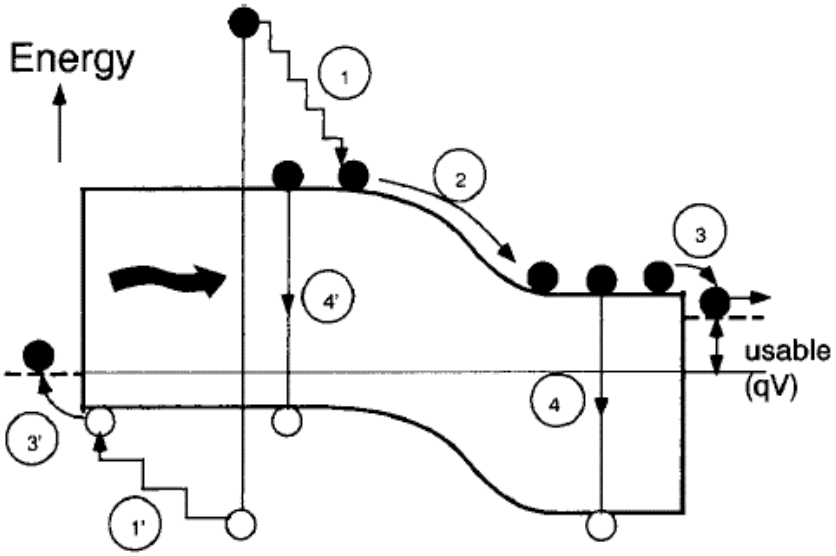

Figure 1.1: Losses in a p-n junction solar cell with respect to the conduction band (top solid line) and the valence band (bottom solid line) as a function of distance from the cathode. (1) Thermalisation to the band edge, (2) junction loss, (3) contact loss, (4) recombination loss. The dashed lines are the electrode work functions and the (un)primed quantities represent processes relevant to (electrons) holes. Process 4 involves an electron and a hole, hence its inclusion in both the p and n sides of the junction. From reference [17].

$$\eta_{Carnot} = 1 - \frac{T_{out}}{T_{in}}. \tag{1.1}$$

The surface of the Sun (T_{in}) is roughly 6000K, so for a solar cell operating at 300K (T_{out}), the Carnot efficiency is 95%. Crucially however, this is for a Carnot *cycle* which assumes that, in equilibrium, the emitted photons from the cell go back to the Sun helping it maintain thermal equilibrium [17, 2]. Regarding these photons as a loss mechanism reduces this figure to 93.3%. This is far higher than the theoretical maximum of 31% for a single junction device as shown by Shockley in 1961 [18]. It is therefore necessary to look at the loss mechanisms in a generic single junction solar cell, such as a classical p-n junction. These are illustrated in figure 1.1.

The thermalisation loss (process (1) in figure 1.1) limits the efficiency to ∼44% [18, 17]. This is because in an ideal semiconductor of bandgap, E_g, all incident photons with energies below E_g will not be absorbed and those with energies above E_g will have the same effect as those at E_g due to process (1) in figure 1.1. The usable voltage obtainable from a solar cell is equal to the difference in potential between the contacts, so this accounts for the loss mechanisms (2) and (3) [2]. To minimise process (3) ohmic contacts can be used as these have zero resistance loss by definition. Process

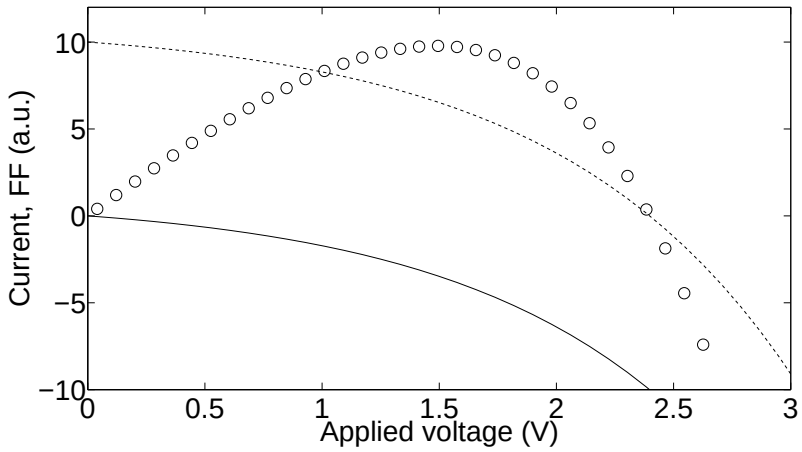

Figure 1.2: Qualitative representations of the current-voltage characteristic in the dark (solid line) and under illumination (dashed line). The output power of the device under illumination is also shown (◯). This is the product of the current and the applied bias and shows a clear maximum since the bias is zero at short circuit and the current is zero at open circuit.

(4), recombination, can be minimised by using materials with long carrier lifetimes [17]. The effect of radiative recombination is also important since a solar cell must emit photons as well as absorb them to remain in equilibrium; this loss is completely unavoidable [2]. The bandgap of the converter material is crucial also because a small bandgap is required for a large photocurrent but a large value is needed for a high open circuit voltage; both of which are important for high efficiency. These factors gives rise to an optimum value of E_g and a maximum efficiency of 31% [18].

Recently, the limiting efficiency of an organic photoconverter has been considered [48], concluding on a figure of ∼20%, roughly twice the figure thought to be needed to break into commercial applications. The improvements which need to be overcome before this figure can be realised include better absorption matching with the solar spectrum, surmounting of the 'exciton diffusion bottleneck' (the dissociation of excitons before they can recombine) and decreasing cell resistance [48]. A more complete review of the detailed balance theory in the context of solar cells is given in reference [49].

1.5.2 Electrical parameters

Figure 1.2 shows the form of the current-voltage characteristic for a solar cell in the dark and under illumination. The short circuit current density, J_{sc} is defined as the current density under illumination at zero applied bias and under these conditions the potential difference between the electrodes is called the built-in bias, V_{bi}. The open

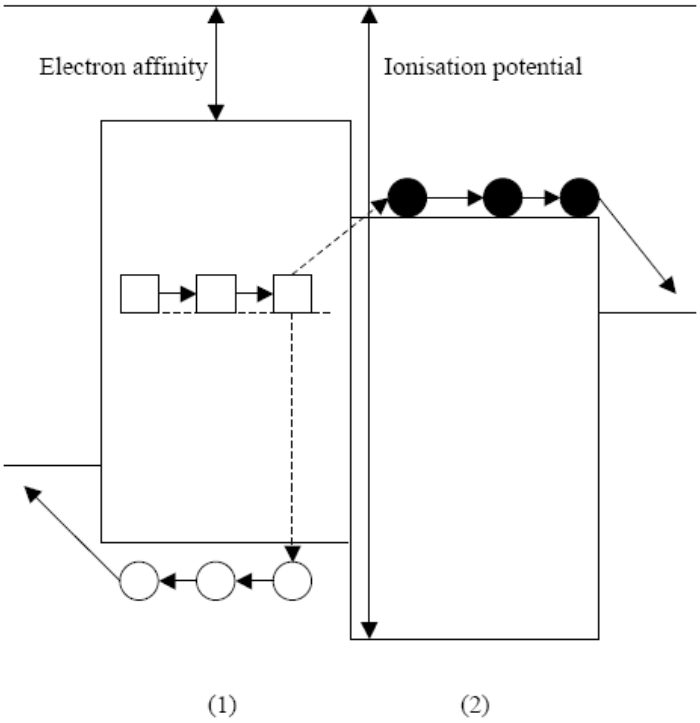

Figure 1.3: Schematic representation of exciton diffusion and dissociation in a two-component organic solar cell. The exciton (squares) moves by diffusion in phase **1** until it meets the material heterojunction. Material **2** has a higher electron affinity and ionisation potential and so the electron (filled circle) is transferred to **2** and the hole (empty circle) stays on **1**. After exciton dissociation, the electron and hole are transferred to their respective electrodes to complete the circuit.

circuit voltage, V_{oc}, is the applied bias at which the photogenerated, extracted current equals the injected current and therefore the total current is zero. Other important quantities for solar cells are the maximum power point power conversion efficiency, η_{mpp} and the fill factor, FF. The efficiency at maximum power point is the power density delivered to the external circuit divided by the incident illumination power density, P_0,

$$\eta_{mpp} = \frac{J_{mpp}V_{ampp}}{P_0}. \tag{1.2}$$

$J_{mpp}V_{ampp}$ is the product of the current density and the applied voltage at the maximum power point. The FF is defined as

$$FF = \frac{J_{mpp}V_{ampp}}{J_{sc}V_{oc}} \equiv \frac{\eta_{mpp}P_0}{J_{sc}V_{oc}}. \tag{1.3}$$

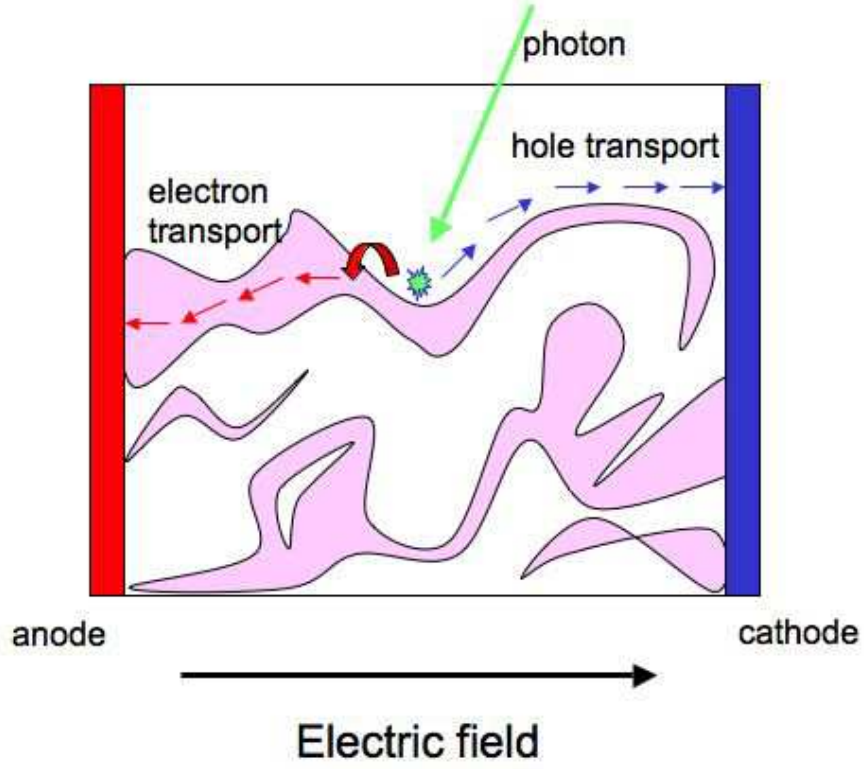

Figure 1.4: A schematic diagram of a bulk heterojunction solar cell showing exciton generation and dissociation as well as the subsequent transport of electron and holes to their respective extracting electrodes. Used with permission from J. Nelson, Department of Physics, Imperial College London.

and is a measure of the 'squareness' of the current-voltage characteristic in figure 1.2 [2].

These four important performance parameters are often stated under AM1.5 illumination conditions. The AM stands for air mass and the 1.5 represents the increased path length of the light through the Earth's atmosphere compared to that with the sun overhead. Specifically, when the angle of incidence (θ) is such that cosec(θ_s)=1.5, θ_s=42^o [2].

The Shockley diode equation for a solar cell under bias (as shown in figure 1.2) gives the current-voltage characteristic of an ideal, single junction, solar cell [1],

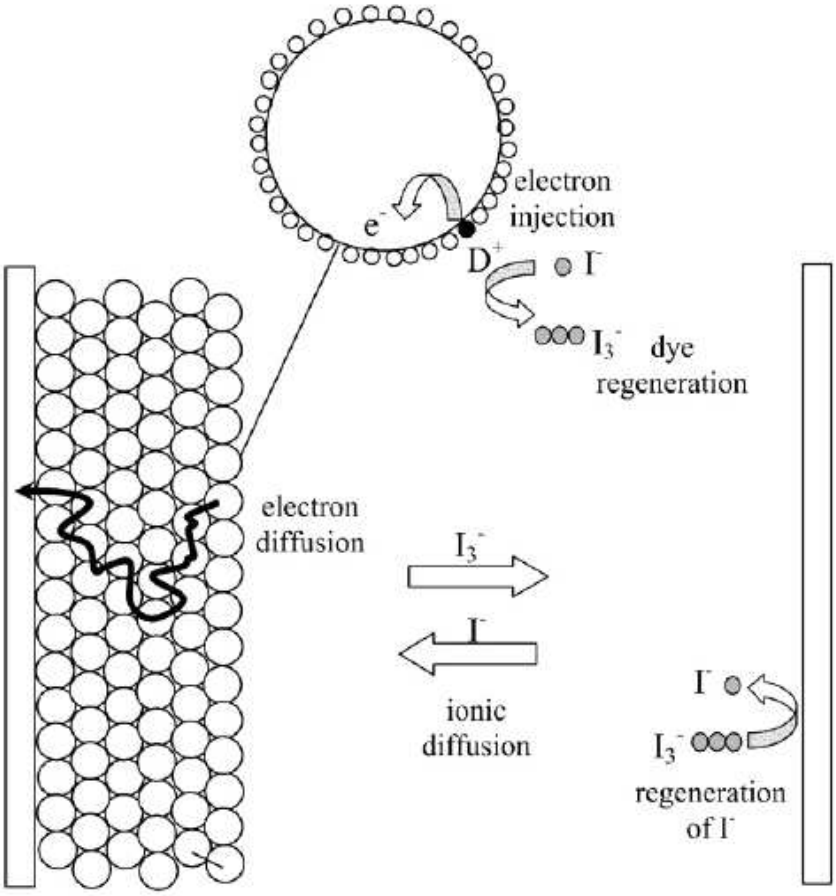

Figure 1.5: The function of the DSSC showing electron injection and diffusion as well as the redox properties of the electrolyte. From reference [21].

$$J = J_0 \left(\exp\left(\frac{eV_a}{k_B T} \right) - 1 \right) + J_{sc}, \tag{1.4}$$

where J_0 is the reverse bias saturation current, e is the electron charge, k_B is Boltzmann's constant, V_a is the applied bias and T is the absolute temperature. Therefore, the applied bias when the total current is zero (the open circuit voltage, V_{oc}) is

$$V_{oc} = \frac{k_B T}{e} \ln\left(\frac{J_{sc}}{J_0} + 1 \right). \tag{1.5}$$

Assuming that J_{sc} is proportional to the light intensity, the open circuit voltage is expected to increase logarithmically [2].

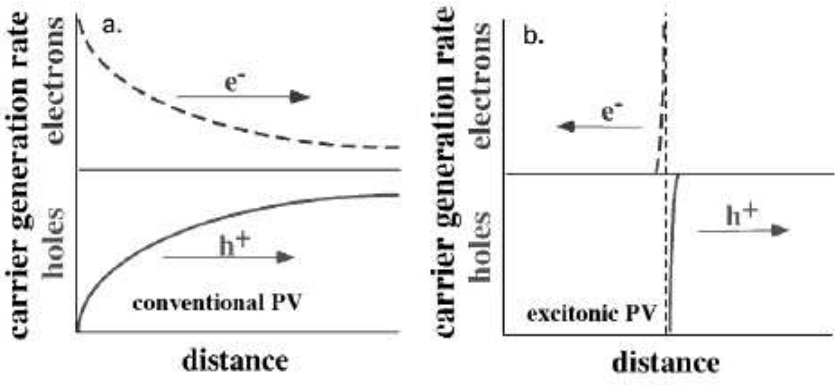

Figure 1.6: Comparison of the photogeneration mechanisms of conventional (left) and excitonic (right) solar cells. From reference [23].

1.6 Excitonic solar cells

In an organic polymer or dendrimer, the initially photogenerated state is a strongly bound electron-hole pair, called an exciton. The exciton is charge neutral and therefore moves by diffusion. The binding energy of this exciton is ∼100meV, which is roughly two orders of magnitude greater than that in inorganic semiconductors [19]. Since the thermal energy at room temperature is ∼25meV, excitons are not usually observed at room temperature in inorganic semiconductors - since they can rapidly dissociate by absorption of a phonon - and the resulting state is therefore a *free* electron-hole pair [23]. The spatial distributions of photogenerated electrons and holes are thus identical in the absence of excitons. Conversely, the thermal energy is not strong enough to dissociate the exciton in an organic polymer at room temperature. Photovoltaic action demands that the exciton be split into its constituent charges and a common way of achieving this is to include a second material in the vicinity of the absorption site.

If one material has a larger electron affinity and ionisation potential (**2**) then the exciton can be separated and the electron may be transferred to (**2**) and the hole left on (**1**), assuming the photogeneration occurred on (**1**) [19], as illustrated in figure 1.3. In fact, the resulting state after exciton dissociation is not a free electron in the acceptor and a free hole in the donor but a bound charge-transfer state known as a polaron pair, which extends across the junction between the two materials. Another possibility is that the exciton is transferred between the phases in a process known as energy transfer. The key point is that charge transfer will occur if the energy of the charge-transfer state is lower than that of an exciton on either material respectively [50]. After charge transfer has occurred and the electron and hole are separated, the charges will then diffuse in different directions as they have opposite spatial derivatives.

This subtle difference between organic and inorganic solar cells has a powerful effect

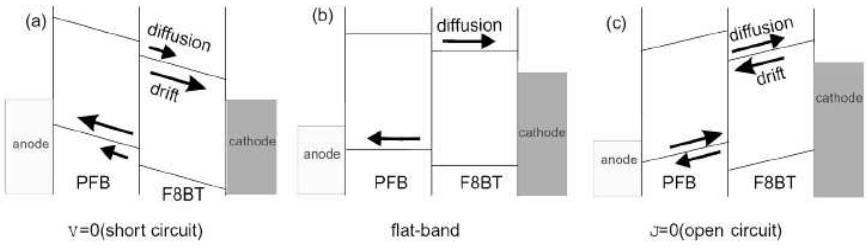

Figure 1.7: Bandstructure of an organic bilayer device at short circuit, flat band and open circuit conditions, from [55]. The acceptor material is poly(9,9'-dioctylfluorene-co-benzothiadiazole) (F8BT) and the donor is poly(9,9'-dioctylfluorene-co-bis-N,N'-(4-butylphenyl)-bis-N,N'-phenyl-1,4-phenylenediamine) (PFB), which are both commonly used organic polymers.

on the performance of the device [23, 51, 52, 53, 54] and crucially, the same excitonic description can be used for the DSSC as well as for organic heterojunction solar cells. Figures 1.4 and 1.5 show schematic diagrams of a bulk heterojunction, polymer blend solar cell and a DSSC respectively.

The common feature of the photogeneration mechanism of excitonic solar cells is that the processes of charge generation and separation happen simultaneously at a material heterojunction. The organic-organic interface separates the exciton into its constituent charges as shown in the right hand pane of figure 1.6 and the same simultaneity of charge separation and generation occurs at the dye-TiO_2 interface in the DSSC. The exciton is created in the dye at the surface of the TiO_2, which is followed by fast electron injection into the conduction band of the TiO_2 [21]. In an inorganic device, such as silicon, electron-hole pairs are generated together in a bulk material and hence they will tend to diffuse in the same direction, as in the left hand pane of figure 1.6. Because the charges need to get to the opposite sides of the device to constitute a photovoltaic effect, the action of an electric field is needed to pull the charges apart. This limits V_{oc} to be less than V_{bi}, whereas values of the V_{oc} greater than V_{bi} are routinely observed in organic devices; as in the work reported by Ramsdale *et al.* [56]. In this case, the reason for the V_{oc} being greater than V_{bi} is that at an applied bias equal to V_{bi}, there is a diffusion current away from the interface which needs to be negated by a drift current at open circuit where the total current is zero [56]. Therefore, there must be an electric field opposing the direction of the built-in field. This can only be the case if $V_{oc} > V_{bi}$ and is illustrated in figure 1.7 for a bilayer polymer device.

In a semiconductor, the movement of charges by drift is driven by the gradient of the electric potential and the diffusion is driven by the gradient of the chemical potential [23]. The former is generally greater in conventional solar cells because both photogenerated electrons and holes will tend to diffuse in the same direction, as noted above. In

organic devices however, carriers are generated at an interface between dissimilar materials leading to a large chemical potential gradient. The dominance of the chemical potential gradient in organics is further enhanced by the generally low charge densities, which reduces the drift current. Also, the converse situation is intensified in inorganics by the high mobilities, which tend to smooth out concentration gradients, hence reducing the diffusion current [23].

All of these factors together can mean that in excitonic devices, the chemical potential gradient can be larger than the electric potential gradient. The DSSC is an extreme example where - since all electric fields are screened below a certain doping level in the TiO_2 [21] - the drift velocity is zero everywhere and movement of charge is driven by chemical potential gradients only. The two fundamental forces, the electric and chemical potential gradients, can be considered together to be aspects of the same, electrochemical, potential. This unified potential is also referred to as the quasi-Fermi level, or free energy [21].

The dye-sensitised solar cell is now considered in part I and organic devices in part II of this work.

Part I: Dye-sensitised solar cells

Chapter 2

Simulation of dye-sensitised nanocrystalline solar cells

In this chapter, the device physics of simulating a DSSC after it has undergone a short (8ns) laser pulse at open circuit is introduced before moving on to simulation results. Reference is frequently made to the transport time and rise time throughout. The former is the time taken for 63% of the excess photogenerated electrons to be extracted from the device and the latter is that needed to extract just enough to charge the capacitance of the underlying substrate. This capacitance has been shown to be significantly smaller than that of the TiO_2 and therefore only a small fraction of the excess electrons are extracted in this case. The origin of the figure of 63% is that $1 - \frac{1}{e}$=0.63, where e is the base of natural logarithms. This assumes that the rise of the photovoltage can be described by a single exponential function.

2.1 Introduction

The functional parts of a DSSC consist of inorganic titanium dioxide (TiO_2), sensitised by a monolayer of highly-absorbing dye molecules, immersed in a iodide/triiodide redox couple solution. There have also been recent efforts to replace the redox liquid with a solid state hole transporter [22]. Upon photoexcitation, electrons are excited from the dye molecule into the conduction band of the TiO_2. This leaves a hole on the dye molecule which is reduced by the redox couple. The TiO_2 conduction band electrons are extracted at the anode and to complete the circuit an electron is injected into the redox couple at the opposite electrode. Power conversion efficiencies as high as 11% have been demonstrated using the liquid-based DSSC [21], which is roughly a factor of

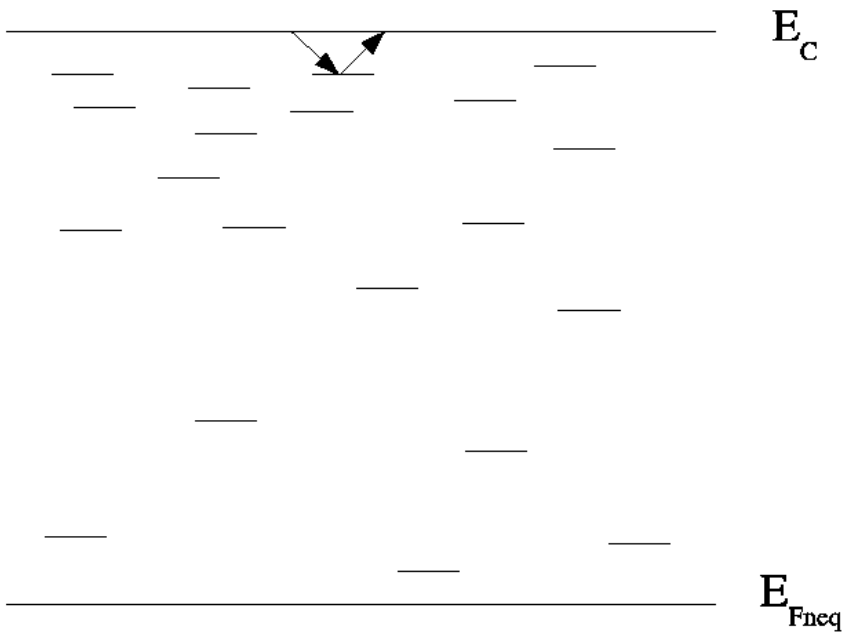

Figure 2.1: Schematic band diagram of the TiO_2 in a DSSC. The top of the figure represents the conduction band level, E_C and the bottom is the equilibrium Fermi level $E_{Fn,eq}$, which is the level up to which electron traps are filled at zero bias and zero light intensity. The small arrows represent the trapping and subsequent de-trapping of a conduction band electron.

two higher than the maximum reported efficiency for polymer blend devices.

Electric fields have been shown to be largely screened in liquid electrolyte DSSCs [57] and therefore the transport of conduction band electrons can be well described by diffusive transport with electric fields playing a relatively minor rôle [21, 58, 59]. This diffusive transport is complicated by the fact that the TiO_2 contains many electron traps in its bandgap. Figure 2.1 schematically illustrates the trapping and detrapping of conduction band electrons with these states.

2.2 Methodology

A new method of characterising the transport behaviour in DSSCs at open circuit has been proposed recently [60]. The experimental method consists of two different measurements on a DSSC held at open circuit V_{oc},

1. A photocurrent measurement.
2. A photovoltage measurement.

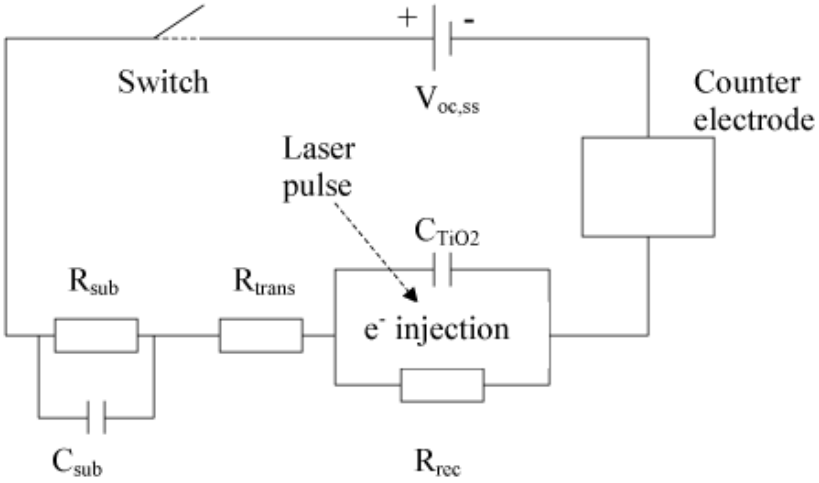

Figure 2.2: Equivalent circuit diagram for the DSSC, the components of which are the capacitance of the TiO_2, C_{TiO2}, its transport resistance, R_{trans}, the capacitance of the underlying substrate, C_{sub}, its resistance, R_{sub}, and the effective resistance due to recombination, R_{rec}. The dashed line represents the incident laser pulse which injects electrons in the TiO_2. The battery symbol illustrates the constant, DC bias on the cell, equal to V_{oc} and the switch is open (solid line) for photovoltage measurements and closed (dashed line) for photocurrent measurements. Adapted from reference [60].

These two experiments can be represented by the equivalent circuit in figure 2.2

In both measurements, the solar cell is held at open circuit with a bias across the cell under illumination. In the photocurrent measurement, the switch in figure 2.2 is closed and the circuit is complete. An additional short pulse of laser light is then incident on the DSSC which injects some electrons into the TiO_2 and raises the voltage by a small amount, typically $\sim$2mV [60]. In equivalent circuit terms, this is the same as the addition of some extra charge to C_{sub}. Because the circuit is complete, the extra charge can flow around the external circuit and the current, $j(t)$, can be integrated to give the amount of charge from the laser pulse, $Q(t)$,

$$Q(t) = \int_0^t j(t')dt'. \tag{2.1}$$

The associated transient response measures the flow of electrons through the TiO_2 film and the corresponding time constant, τ_{trans} can be expressed as

$$\tau_{trans} = R_{trans}C_{TiO2}, \tag{2.2}$$

which is the transport time of the DSSC, using the standard relationship for the time taken to charge a capacitor through a resistor. It is important that the photovoltage rise in the TiO_2 is small because it is the transport properties of the DSSC at open circuit conditions which are of interest.

In the second experiment, the charge is prevented from flowing around the external circuit by opening a switch in figure 2.2. Therefore, when the laser pulse is incident on the DSSC, the extra photogenerated charge will flow into the substrate capacitance, C_{sub}, and the current will stop flowing throughR_{trans} when the voltage across C_{sub} and C_{TiO2} is equal. It has been experimentally verified that the capacitance of the TiO_2, which is due to its high trap density, is much larger than that of the substrate. This means that only a small fraction of the total charge generated by the pulse needs to be given to C_{sub} for the system to regain equilibrium. As for the photocurrent experiment, the current can be integrated to find the charge that has flowed into C_{sub}. This charge can then be divided by the C_{sub} to obtain the photovoltage rise in the substrate, $U_{ph}(t)$,

$$U_{ph(t)} = \frac{\int_0^t j(t')dt'}{C_{sub}} = \frac{Q(t)}{C_{sub}}, \tag{2.3}$$

assuming implicitly that $C_{TiO_2} \gg C_{sub}$. This assumption indicates that the voltage across C_{TiO2} will remain constant as C_{sub} is charged. This amounts to charging the substrate capacitance through the resistance R_{trans} at a constant bias.

The transient response of the system in this case represents the rise time of the photovoltage in the substrate, τ_{rise}, and is given by

$$\tau_{rise} = R_{trans}C_{sub}. \tag{2.4}$$

From equations 2.4 and 2.2, the transport time can be obtained from the rise time if the capacitances are known,

$$\tau_{trans} = \tau_{rise}\frac{C_{TiO2}}{C_{sub}}. \tag{2.5}$$

The goal of this experimental method is to obtain τ_{trans} from a measurement of τ_{rise}.

Once τ_{trans} has been obtained from equation 2.5, the diffusion coefficient, D_n, can be obtained from

$$D_n = \frac{d^2}{\tau_{trans}}, \tag{2.6}$$

where d is the thickness of the TiO_2 layer.

In addition to the consideration of the photovoltage rise, its decay can give τ_n, the conduction band electron lifetime. These two quantities can be combined to define the electron diffusion length, L_n [2, 21],

$$L_n = \sqrt{D_n \tau_n}. \tag{2.7}$$

This is an important parameter because the longer the diffusion length, the greater the chance of electron extraction before recombination. Ultimately, L_n should be greater than the width of the TiO_2 layer, d, so that all photgenerated carriers can contribute to the photocurrent. It is therefore the goal of this work to simulate the quantities τ_{trans} and τ_{rise} numerically.

2.3 Modelling electrons in dye-sensitised solar cells

The numerical scheme to simulate τ_{trans} and τ_{rise} at open circuit in a DSSC is now described.

2.3.1 Bulk transport and trapping in the DSSC

As noted earlier, the electric field in DSSCs is largely screened so that the transport of conduction band electrons can be described by a trap-limited diffusion equation [58, 61]. The multiple trapping model is applied which solves for the densities of conduction band, n_c, and trapped electrons, n_t in the TiO_2,

$$\frac{\partial n_c}{\partial t} = D_0 \frac{\partial^2 n_c}{\partial x^2} + \alpha I_0 \exp\left(-\alpha x\right) - k_{cb0}\left(n_c - n_{c,eq}\right) - \frac{\partial n_t}{\partial t}, \tag{2.8}$$

$$\frac{\partial n_t}{\partial t} = N_{t,0}\left\langle \frac{\partial f}{\partial t} \right\rangle = \left\langle k_t n_c \left(1 - f\right) - k_d N_{t,0} f \right\rangle. \tag{2.9}$$

D_0 is the bare diffusion coefficient (if trapping were absent), α the absorption coefficient, I_0 the illumination intensity, k_{cb0} is the rate constant for recombination of conduction band equilibrium $n_{c,dark}$ is the equilibrium density of electrons in the dark, $N_{t,0}$ is the total density of trap sites, f is the trap occupation probability, k_t is the rate constant for trapping and k_d is the rate for detrapping. In the case where $\frac{\partial n_c}{\partial t} = 0$, $\frac{\partial n_t}{\partial t} = 0$ also and therefore traps make no contribution to the device behaviour.

It is crucial to note that k_d is not a constant, but depends on the trap depth because there is a distribution of electron traps in a DSSC [21]. This distribution decays exponentially into the bandgap as shown in figure 2.3 and can be described by the equation,

$$g(E_T) = \frac{N_{t,0}\beta}{k_B T}\exp\left(-\frac{\beta\left(E_C - E_T\right)}{k_B T}\right), \tag{2.10}$$

where the factor β represents the rate at which the trap distribution falls off into the bandgap [61]. The triangular brackets in equation 2.9 represent the averaging over the trap distribution, equation 2.10. The implementation of these equations for the modelling of the DSSC is non-trivial since the coupled system of equations (equations 2.8 and 2.9) amounts to a system of integro-differential equations which needs manipulating before it can be solved using the **COMSOL** software package used throughout this work. This is because, for a generic variable, ν,

$$\langle\nu\rangle = \int_{E_{Fn,eq}}^{E_C} dE_T g(E_T)\nu(E_T), \tag{2.11}$$

where $E_{Fn,eq}$ is the equilibrium Fermi level of the redox solution and E_C is the conduction band level in the TiO_2. The solution to this problem is considered in Appendix C.

2.3.2 Boundary conditions for electron transport time

Firstly, the boundary conditions for calculating the transport time of conduction band electrons is considered. The boundary conditions for extraction of charge for the DSSC are simpler in form than those used for the metal-organic interfaces as considered previously. This is because of the absence of electric fields in the discussion so that, for example, the Schottky effect does not require consideration. The interface between the TiO_2 and the electrolyte at the counter electrode is insulating for conduction band

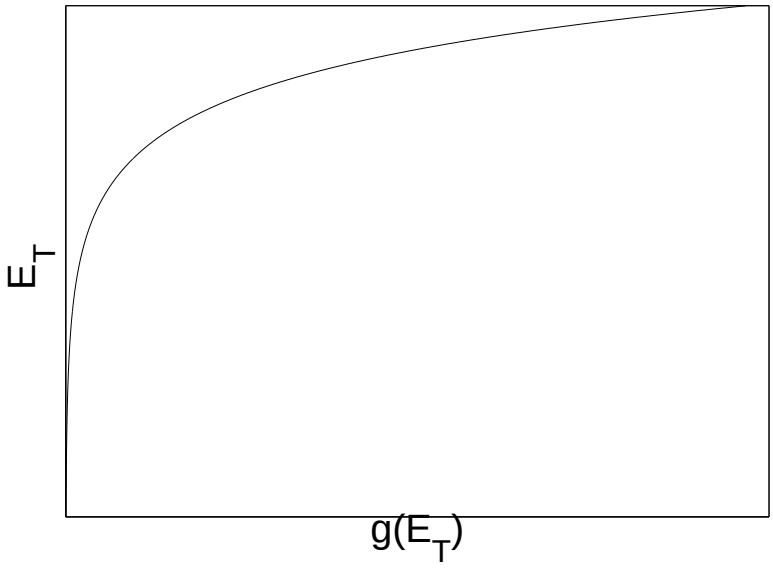

Figure 2.3: Graphical illustration of the trap distribution, $g(E_T)$ showing that there are exponentially more traps near the conduction band, that is, more shallow traps. The top horizontal line represents the conduction band and the bottom horizontal line is the equilibrium Fermi level, $E_{Fn,eq}$.

electrons so that $\frac{\partial n_c}{\partial x} = 0$. At the anode, $x = 0$, the excess conduction band electrons are extracted at a rate, k_{ext}, so that

$$j(t) = eD_0 \frac{\partial n_c(x,t)}{\partial x}\bigg|_{x=0} = ek_{ext}\left(n_c(0,t) - n_{c,eq}\exp\left(\frac{eV_{oc}}{k_BT}\right)\right), \tag{2.12}$$

where the first equality is Fick's law and $n_{c,eq}\exp\left(\frac{eV_{oc}}{k_BT}\right)$ is the conduction band electron density at open circuit, that is, before the laser pulse.

2.3.3 Boundary conditions for photovoltage rise times

For the case of calculating photovoltage rise times, equation 2.12 needs to be modified because only a small fraction of the excess photogenerated charge need to be extracted. This is because the substrate capacitance is significantly lower than the bulk capacitance of the TiO_2 due to the high density of traps [60]. However, when the photovoltage rise time is considered, a way of telling the simulation's clock to stop running when enough charge has been extracted to charge the substrate capacitance is required.

Equation 2.12 can be thought of consisting of an extraction component $ek_{ext}n_c(0,t)$

and an injected component $-ek_{ext}n_{c,eq}\exp\left(\frac{eV_{oc}}{k_BT}\right)$. Since electrons are flowing into the substrate, the voltage across it will rise by an factor equal to Boltzmann factor $\exp\left(\frac{eU_{ph}(t)}{k_BT}\right)$, where $U_{ph}(t)$ is the photovoltage rise in the substrate, given by equation 2.3.

The boundary condition for calculation of the photovoltage rise time is therefore written,

$$j(t) = ek_{ext}\left(n_c(0,t) - n_{c,eq}\exp\left(\frac{eV_{oc}}{k_BT}\right)\exp\left(\frac{eU_{ph}(t)}{k_BT}\right)\right). \tag{2.13}$$

The premise of this modified boundary condition is that the current will go to zero when the substrate photovoltage has increased by the same amount as in the bulk TiO_2. The rise in the TiO_2 photovoltage is assumed to take place instantaneously, which is manifested in the rise in $n_c(0,t)$. Equation 2.13 assumes that the density of conduction band electrons, $n_c(0,t)$, in the TiO_2 does not change when the electrons are extracted into the substrate. Compared to the situation before the pulse, the value of $n_c(0,t)$ is assumed to be raised by a factor

$$\exp\left(\frac{eV_{pulse}}{k_BT}\right). \tag{2.14}$$

In equation 2.14, V_{pulse} is the height of the photovoltage rise in the TiO_2 and therefore,

$$n_c(0,t) = n_{c,eq}\exp\left(\frac{e\left(V_{oc}+V_{pulse}\right)}{k_BT}\right). \tag{2.15}$$

The fact that the density at the anode will decrease as charge is extracted will tend to reduce the rise time below the diffusion limit.

The essential difference between equation 2.13 (for the photovoltage rise time) and equation 2.12 (for the electron transport time) is that the background by which the excess charge is measured is changing in the former case.

2.3.4 The quasi-static approximation

As described in section 2.3.1, the densities of trapped (n_t) and conduction band (n_c) electrons can be described by coupled differential equations. However, if the characteristic timescales of trapping and detrapping are significantly faster than other competing effects (diffusion, recombination etc.) then the effects of the electron traps can be absorbed into a single continuity equation for n_c but with an *effective* diffusion coefficient, D_n, and an *effective* conduction band lifetime, k_{cbn}, which is the inverse of the recombination rate [59, 61]. The fundamental equation of the quasi-static approximation describes the relation between the rates of change of n_c and n_t, and assumes they are proportional to one another,

$$\frac{\partial n_t}{\partial t} = \frac{\partial n_t}{\partial n_c}\frac{\partial n_c}{\partial t}. \tag{2.16}$$

The proportionality function $\frac{\partial n_c}{\partial n_t}$ is independent of time and will be derived later. Equation 2.16 implies that even when the DSSC is not in equilibrium (that is, a current flows), the trapped and conduction band electrons are in equilibrium with each other [59]. This definition is analogous to that of the quasi-Fermi level, where electrons are in thermal equilibrium with the underlying semiconductor structure but are not in thermal equilibrium with the holes [21]. Considering equations 2.8 and 2.9, it can be shown that

$$\frac{\partial n_c}{\partial t} = D_n\frac{\partial^2 n_c}{\partial x^2} - k_{cbn}\left(n_c - n_{c,eq}\right), \tag{2.17}$$

with

$$D_n = \frac{D_0}{1 + \frac{\partial n_t}{\partial n_c}}, \tag{2.18}$$

and

$$k_{cbn} = \frac{k_{cb0}}{1 + \frac{\partial n_t}{\partial n_c}}. \tag{2.19}$$

The problem is therefore reduced to the solution of a single diffusion equation with

an effective diffusion coefficient and conduction band lifetime [59, 61]. An expression for the function $\frac{\partial n_t}{\partial n_c}$ is still required however. In steady state, $\frac{\partial}{\partial t} = 0$, the solution to equation 2.9 gives

$$f(E_T) = \frac{1}{1 + \exp\left\{\frac{(E_T - E_F)}{k_B T}\right\}} \approx \theta\left(E_F - E_T\right), \tag{2.20}$$

where $\theta = 1$ below the Fermi level and zero otherwise and the final relation is true if

$$k_B T \ll \left|E_T - E_F\right|. \tag{2.21}$$

Using equation 2.11 for the variable f and the approximation in equation 2.21,

$$n_t = N_{t,0} f = N_{t,0} \int_{E_{Fn,eq}}^{E_C} dE_T g(E_T) f(E_T) \approx N_{t,0} \int_{E_{Fn,eq}}^{E_{Fn}} dE_T g(E_T). \tag{2.22}$$

Now, using equation 2.10 for the trap distribution $g(E_T)$,

$$\begin{aligned} n_t &\approx N_{t,0} \frac{\beta}{k_B T} \int_{E_{Fn,eq}}^{E_{Fn}} dE_T \exp\left[-\beta \frac{(E_C - E_T)}{k_B T}\right] && (2.23) \\ &= N_{t,0} \left(\exp\left[-\beta \frac{(E_C - E_{Fn})}{k_B T}\right] - \exp\left[-\beta \frac{(E_C - E_{Fn,eq})}{k_B T}\right]\right) && (2.24) \\ &= \frac{N_{t,0}}{N_C^\beta} \left(n_c^\beta - n_{c,eq}^\beta\right). && (2.25) \end{aligned}$$

Therefore,

$$\frac{\partial n_t}{\partial n_c} = \frac{\beta N_{t,0}}{N_C^\beta} n_c^{\beta-1} = \frac{N_{t,0}\beta}{N_C} \left(\frac{n_c}{N_C}\right)^{\beta-1}, \tag{2.26}$$

which is the desired expression.

2.3.5 Analytical model for τ_{rise} and τ_{trans}

A simple analytical model for calculation of τ_{rise} and τ_{trans} has been developed [62]. Experimentally, it has been found that the transport time of photogenerated electrons is equal to

$$\tau_{trans} = \frac{d^2}{2.8D_n}, \tag{2.27}$$

where d is the thickness of the TiO_2 layer (typically 4-10μm) and D_n is the diffusion coefficient of conduction band electrons. The factor of 2.8 is an empirical factor determined experimentally and takes account of the non-uniform illumination profile in the devices [62].

The capacitance per unit area of the TiO_2 is due to the traps with the distribution described by equation 2.10 and is given by,

$$C_{TiO2} = e^2 dg(V_{oc}), \tag{2.28}$$

which assumes that all the traps up to V_{oc} are filled and those above it are empty. The transport time is the product of the transport resistance of the TiO_2, R_{trans}, and its capacitance, C_{TiO_2} [60] so that using equations 2.27 and 2.28,

$$R_{trans} = \frac{d^2}{2.8D_n C_{TiO_2}} = \frac{d}{2.8D_n e^2 g(V_{oc})}. \tag{2.29}$$

Equation 2.29 can now be used to calculate the rise time of the photovoltage from equation 2.4

$$\tau_{rise} = \frac{dC_{sub}}{2.8D_n e^2 g(V_{oc})}. \tag{2.30}$$

Equations 2.27 and 2.30 are the diffusion limited transport time and rise time respectively. These correspond to an infinite extraction rate, k_{ext}, at the TiO_2/substrate interface so that the limiting factor is the diffusion of conduction band electrons to the electrode. For comparison with the numerical modelling of these quantities, it is necessary to introduce the definition of the conduction band diffusion coefficient,

D_n as it appears in equations 2.27, 2.29 and 2.30. For this purpose the quasi-static approximation is used throughout and D_n is given by equation 2.18.

2.3.6 Modelling of the laser illumination

In equation 2.8 only the steady state illumination is considered. In order to take account of the 8ns pulse, it must be modified thus,

$$\begin{aligned}\frac{\partial n_c}{\partial t} &= D_0\frac{\partial^2 n_c}{\partial x^2} + \alpha\left(I_0 + \left[\theta\left(t\right) - \theta\left(t - \tau_{pulse}\right)\right]\delta I_0\right)\exp\left(-\alpha x\right) \\ &\quad -k_{cb0}\left(n_c - n_{c,eq}\right) - \frac{\partial n_t}{\partial t},\end{aligned} \tag{2.31}$$

where δI_0 represents the additional pulse intensity and $\left[\theta\left(t\right) - \theta\left(t - \tau_{pulse}\right)\right]$ is equal to 1 for $0 < t < \tau_{pulse}$ and zero otherwise. The simulation begins at $t = 0$, which is defined as the beginning of the pulse.

The calculation of the parameter δI_0 is now considered. The capacitance of the TiO_2 is significantly higher than that of the substrate, it is therefore a good approximation to assume that the photovoltage rise is due to the increase in the density of trapped electrons alone. If the photovoltage is to be raised by an amount ΔU_{ph}=5mV, say. the number of electrons per unit area, N, which must be supplied to raise the TiO_2 photovoltage by ΔU_{ph} is given by,

$$N = \frac{C_{TiO_2}\Delta U_{ph}}{e} = \frac{e^2 dg\left(V_{oc}\right)\Delta U_{ph}}{e}. \tag{2.32}$$

Now assuming that these electrons are created by the absorption of photons from a pulse of intensity δI_0, then the number of generated electrons per cubic metre, $G(x)$, will be

$$G(x) = \alpha\delta I_0 \exp\left(-\alpha x\right), \tag{2.33}$$

which has the units of $\mathrm{m}^{-3}\mathrm{s}^{-1}$, so this is multiplied by the pulse length, τ_{pulse} to find the number of absorbed photons per unit volume. Integrating between $x = 0$ and $x = d$ yields,

$$N = \tau_{pulse} \int_0^d \alpha \delta I_0 \exp(-\alpha x)\, \mathrm{d}x = \tau_{pulse} \delta I_0 \left(1 - \exp(-\alpha d)\right). \tag{2.34}$$

Comparing equations 2.32 and 2.34,

$$\delta I_0 = \frac{edg(V_{oc})\Delta U_{ph}}{\tau_{pulse}\left(1 - \exp(-\alpha d)\right)}. \tag{2.35}$$

The parameter in the numerical model which controls the photovoltage is the illumination intensity I_0. So if a simulation at a photovoltage of 0.5V is needed, the intensity (in number of photons per unit area per unit time) needs to be calculated. This is achieved by using the equation [63],

$$n_c(x=0,t) = n_{c,eq} \exp\left(\frac{eV_{oc}}{k_B T}\right) = \frac{I_0 \alpha}{D_0\left(\gamma^2 - \alpha^2\right)}(A_+ + A_- + 1). \tag{2.36}$$

In equation 2.36, the variables are given by

$$A_+ = \frac{\{[k_{ext} + \gamma D_0]\,\alpha \exp(-\alpha d) - [k_{ext} + \alpha D_0]\,\gamma \exp(-\gamma d)\}}{\gamma\{k_{ext}[\exp(\gamma d) + \exp(-\gamma d)] + \gamma D_0[\exp(\gamma d) + \exp(-\gamma d)]\}} \tag{2.37}$$

$$A_- = \frac{\{-[k_{ext} - \gamma D_0]\,\alpha \exp(-\alpha d) - [k_{ext} + \alpha D_0]\,\gamma \exp(\gamma d)\}}{\gamma\{k_{ext}[\exp(\gamma d) + \exp(-\gamma d)] + \gamma D_0[\exp(\gamma d) + \exp(-\gamma d)]\}} \tag{2.38}$$

$$\gamma = \sqrt{\frac{k_{cb0}}{D_0}}, \tag{2.39}$$

where k_{ext}=0 at open circuit. Therefore

$$I_0 = \frac{n_{c,eq} \exp\left(\frac{eV_{oc}}{k_B T}\right) D_0\left(\gamma^2 - \alpha^2\right)}{\alpha(A_+ + A_- + 1)}, \tag{2.40}$$

where V_{oc} is set equal to the photovoltage, which is 0.5V in this case.

$V_{oc}(V)$	0.4
$N_{t,0}$ (m^{-3})	2×10^{25} [62]
β	0.2 [62]
D_0 (m^2s^{-1})	2×10^{-5} [61]
k_{cb0} (s^{-1})	10^4 [61]
k_{trap} (s^{-1})	10^9 [63]
$d(\mu m)$	4 [62]
$\alpha(m^{-1})$	3.2×10^4 [64]

Table 2.1: Simulation parameters for reproduction of the diffusion limited transport times in a DSSC.

2.4 Results

2.4.1 Reproduction of diffusion limited transport times

In order to calculate the electron transport times, numerical simulations were performed using the continuity equations for n_c and n_t in section 2.3.1, the extraction boundary condition in section 2.3.2 and the description of the laser pulse give in section 2.3.6. To ascertain whether this numerical model is giving physically realistic results it is necessary to be able to reproduce data obtained using the simpler, diffusion limited model given in section 2.3.5 above conditions of fast charge extraction. The transport time is the time taken for 63%, $(1 - \frac{1}{e} = 0.63)$, of the photogenerated electrons to be extracted. Therefore, the cumulative extracted charge from the numerical model is plotted as a function of time and the calculated transport time is the time taken to reach 63% of the maximum value. This can the be compared to the value obtained from the diffusion limited model in section 2.3.5.

The values of the electron transport time obtained with the the numerical simulations should approach those obtained by the diffusion limited model as k_{ext} approaches $10^4 ms^{-1}$. This value was used in reference [58] and was chosen since it was found to give diffusion limited results [62].

The parameters used for the simulations in this section are listed in in table 2.1 and the values of the transport time for increasing k_{ext} are seen in figure 2.4, where the dashed line is calculated using the diffusion limited model described in section 2.3.5.

Figure 2.4 shows that the numerical solution approximates the quasi-static model well at values of k_{ext} above $10^4 ms^{-1}$ as expected. The numerically calculated transport times at high k_{ext} are within a factor of 2 of the diffusion limit, compared to a variation in the transport time of a factor of roughly 1000 over the variation in k_{ext} in figure 2.4.

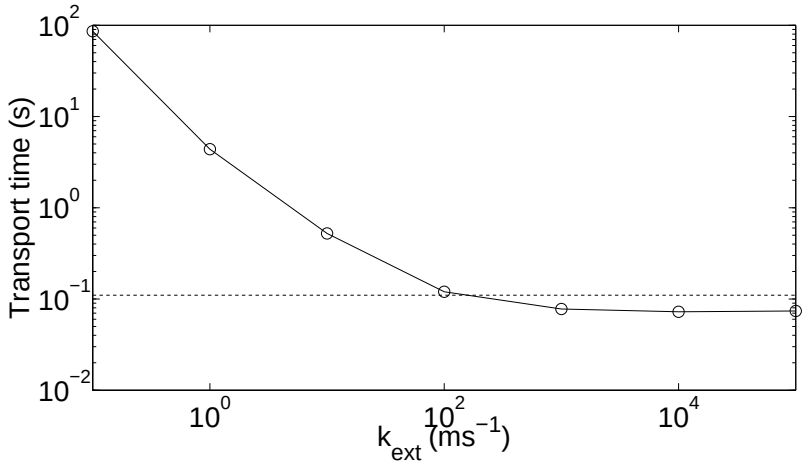

Figure 2.4: Transport times as a function of the extraction rate, k_{ext}, calculated using the parameters given in table 2.1. The dashed line is the value from the diffusion limited model.

This gives confidence that the numerical model is giving physically reasonable results because the two models being compared are very different in nature. The simple, quasi-static model assumed RC time constants for the calculation and the trapping is taken into account by an effective diffusion coefficient. The numerical model however explicitly considers trapping as well as the pulse itself, which is entirely absent from the quasi-static model.

The dependence of τ_{trans} on V_{oc} has also been considered and it is expected that as V_{oc} increases, the rise time will decrease as has been reported experimentally [60]. This is because at higher photovoltages, the deeper traps become filled and so are not involved in trapping. Since the detrapping rate is exponentially dependent on the trap depth, the average time spent in traps will decrease and the effective diffusion coefficient will increase, which is encapsulated in the quasi-static model detailed above. Additionally, at high values of the open circuit voltage, the diffusion limited transport time is expected to saturate because the effective diffusion coefficient approaches its value in the absence of trapping, D_0. This is anticipated to occur at open circuit voltages approaching 1V where the Fermi level in TiO_2 becomes close to the conduction band. Values of the diffusion limited transport time are given in figure 2.5 and show firstly that the model reproduces the expected transport times well at each value of V_{oc} and secondly that the transport time saturates when the diffusion coefficient approaches its bare value, D_0, as expected for values of V_{oc} near 1V.

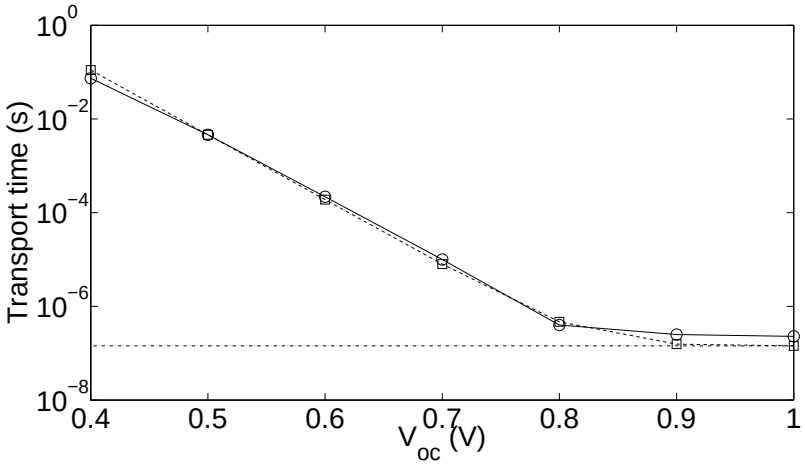

Figure 2.5: Diffusion limited transport times as a function of open circuit voltage, calculated using the parameters given in table 2.1 ($-\bigcirc$) and those calculated from the diffusion limited model ($--\square$). The dotted-dashed line is the value calculated when the diffusion coefficient is equal to the bare value D_0 in the diffusion limited model.

2.4.2 Reproduction of diffusion limited photovoltage rise times

As in the previous section, the behaviour of the photovoltage rise time is now considered as a function of the rate of extraction of conduction band electrons, k_{ext}. The situation is complicated in this case by the fact that only a fraction $\frac{C_{sub}}{C_{TiO_2}}$ of the charge is to be extracted. This is because the substrate capacitance is considerably smaller than the TiO_2 capacitance and therefore not all of the photogenerated charge in the TiO_2 is needed to equalise the Fermi levels and hence reestablish equilibrium.

Again, numerical simulations were performed using the continuity equations for n_c and n_t in section 2.3.1 and the description of the laser pulse give in section 2.3.6. However, now the boundary condition used is different and the form given in section 2.3.3 is used. In the previous section, the transport time was calculated as the time taken to extract 63% of the charge in the device. Now however, the current in the numerical model will go to zero before all the charge has been extracted. In both cases, the extracted current goes to zero at long times, and therefore the rise time can be found using the same formalism as for the electron transport time. This is valid in the case of the rise time because the photovoltage in the substrate is proportional to the amount of charge extracted, from equation 2.3. Figure 2.6 shows the rise times obtained, again using the parameters in table 2.1.

As opposed to the data in figure 2.4, the diffusion limit is underestimated by more than a factor of 10^3 in this case. One possible reason for this considerable underestimation of τ_{rise} is that some of the photogenerated charges are extracted before they can be

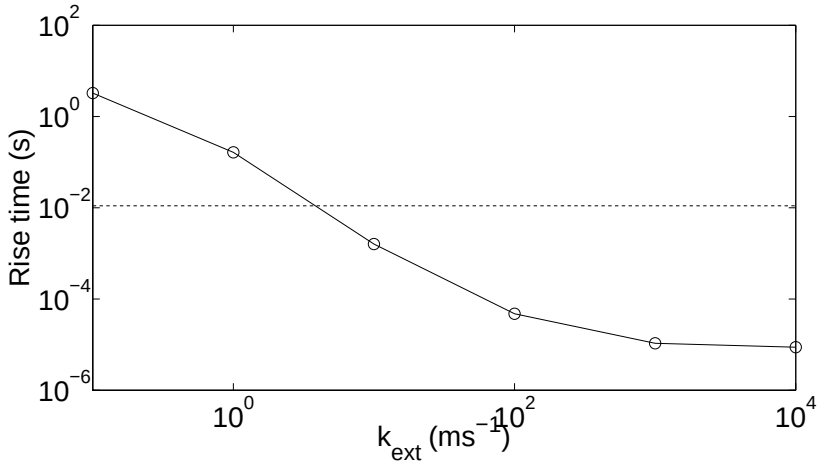

Figure 2.6: Rise times calculated using the parameters given in table 2.1. The dashed line is the value from the diffusion limited model.

trapped so that they cannot be described by the quasi-static approximation, which the diffusion limited model uses as its basis. It is worth noting here that the data in figure 2.6 do show saturation of the rise time at high values of k_{ext}, which can be interpreted as the transport becoming diffusion limited. However, this is not the same as the quasi-static diffusion limit, indicated by the horizontal line in figure 2.6. Simulations were therefore performed for increasing values of the trapping rate k_{trap} to see how high the trapping rate needs to be for the quasi-static diffusion limit to be reproduced, or even if this is possible with this method. For these simulations, a value of $k_{ext} = 10^4 \mathrm{ms}^{-1}$ was used because this was found to be high enough for the rise time to saturate for $k_{trap} = 10^9 \mathrm{s}^{-1}$ as seen in figure 2.6.

Figure 2.7 shows the diffusion limited rise time as a function of the trapping rate, k_{trap} and shows that, as expected, the rise time increases as k_{trap} is increased. Unexpectedly however, the rise time obtained as k_{trap} tends to infinity is still significantly underestimating the value expected for the quasi-static diffusion limit. This is a clear indication that the simulation method is an incomplete description of the physics because it is known experimentally that the photovoltage transients in cells of this kind are diffusion limited [60]. It has already been shown that the assumptions underlying the quasi-static approximation hold for calculation of the transport time in DSSCs. It is therefore of interest to examine the further assumption implicit in the modified Schottky boundary condition used for calculation of the rise time.

The conduction band electron profile in the device for high values of k_{trap} and k_{ext} is therefore considered; specifically the density near the extracting electrode. The boundary condition used for the calculation of rise times is given in equation 2.13. As mentioned above, this equation assumes that the photovoltage will go to zero when

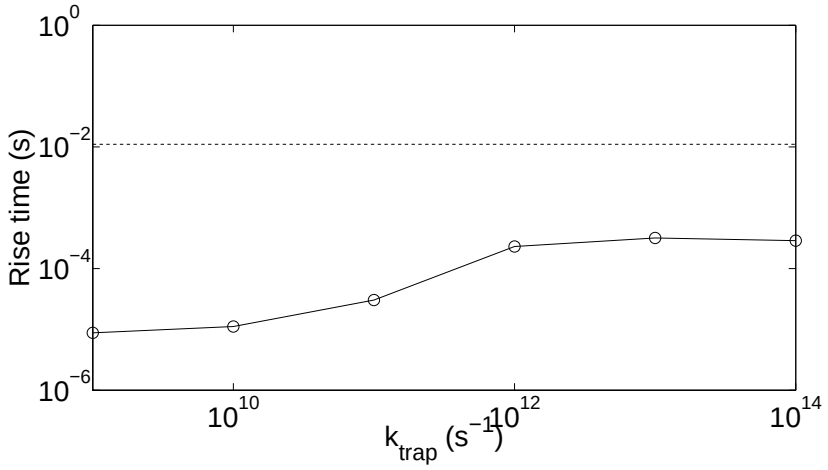

Figure 2.7: Rise times calculated using the parameters given in table 2.1, but with increasing k_{trap} and $k_{ext} = 10^4 \mathrm{ms}^{-1}$. The dashed line is the value from the diffusion limited model.

enough charge has been extracted for the substrate voltage to be raised by, say, 5mV. The crucial assumption implicit in equation 2.13 however is that the density of conduction band charges is equal to $n_{c,eq} \exp\left(\frac{e\left(V_{oc}+V_{pulse}\right)}{k_B T}\right)$ immediately after the pulse and *does not decrease*. The rise time in this case is then the time it takes for the quasi-Fermi level in the substrate to rise up to the level in the TiO_2. Figure 2.8 shows the densities of interest at the extracting electrode for k_{trap}=$10^{13}\mathrm{s}^{-1}$ and $k_{ext} = 10^4 \mathrm{ms}^{-1}$. These parameters were chosen so that the rise time was maximal, as can be seen from inspection of figure 2.7.

There are two noteworthy aspects of this figure. Firstly, the density of conduction band electrons rises above that expected from the simple, quasi-static analysis (by roughly an order of magnitude), which predicts that the density increases by a factor $\exp\left(\frac{eV_{pulse}}{k_B T}\right)$ compared to that before the pulse, $n_{c,eq} \exp\left(\frac{eV_{oc}}{k_B T}\right)$. This is particularly interesting since a very high value of k_{trap} has been used for illustrative purposes. This value is considerably higher than used previously in continuum modelling of DSSCs ($\sim 10^7 \mathrm{s}^{-1}$) [58] and even greater still than a very high value recently reported of $\sim 10^{12}\mathrm{s}^{-1}$ [65]. The fact that the density increases to a value higher than expected from the simple analysis means that the electrons will be diffusing faster than if they were held at the level indicated by the dotted-dashed line in figure 2.8. However, this has already been shown to be a minor effect because the transport time would be equally affected. Secondly, the conduction band electron density decreases significantly below that expected from the diffusion limited model. This is because the high value of the charge extraction rate k_{ext} pulls the density down at the anode meaning that less charge has to be collected for the current to go to zero. This is clear evidence that the assumption in the boundary condition for the extraction of electrons is breaking down and causing the rise time to

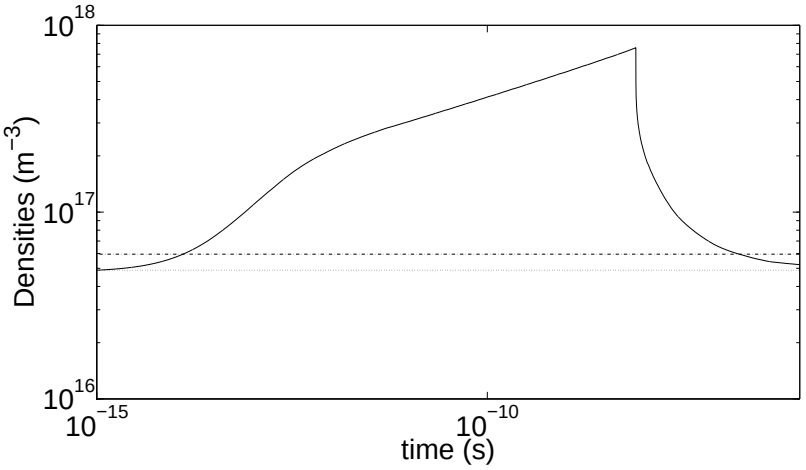

Figure 2.8: Relevant densities for the parameters in table 2.1 with k_{trap}=10^{13}s^{-1} and $k_{ext} = 10^4$ms^{-1}. The quantities are the conduction band density ($-$), the density at the anode at $t = 0$, $n_{c,eq} \exp\left(\frac{eV_{oc}}{k_B T}\right)$ $(\cdot\,\cdot\,\cdot)$ and the density expected from $n_{c,eq} \exp\left(\frac{e(V_{oc}+V_{pulse})}{k_B T}\right)$ $(-\cdot)$.

be too fast.

Figure 2.9 shows a schematic of n_c near the extracting electrode. Because the the value of $n_c(0,t)$ is being pulled down at the interface (as is clear from from 2.8) the current goes to zero before the density in the substrate can be raised by the factor $\exp\left(\frac{eV_{oc}}{k_B T}\right)$ and the rise time is reduced below that expected from the quasi-static model.

For further proof that the fast rise time is not a numerical effect, the magnitude of the photovoltage rise was studied. The diffusion limited model expects that the photovoltage rise height of the substrate will be the same as that in the TiO_2, i.e., 5mV. The results of these simulations are shown in the figure 2.10, which are for the same simulations as shown in figure 2.7.

Figure 2.10 shows that the height of the photovoltage rise saturates at ∼2.5mV. In the simulations, the parameter δI_0 is engineered deliberately to raise the internal voltage of the TiO_2 by 5mV. Therefore, the extracted current is going to zero before the 'correct' amount of charge has been extracted. This is therefore further proof that the faster rise time than expected is a real effect and that the model as it stands does not contain all the physics required to reproduce the experimentally observed diffusion limited rise times.

Another indication that the model as described above is somewhat incomplete is that, experimentally, the photovoltage transients are 'well behaved' when they approach their

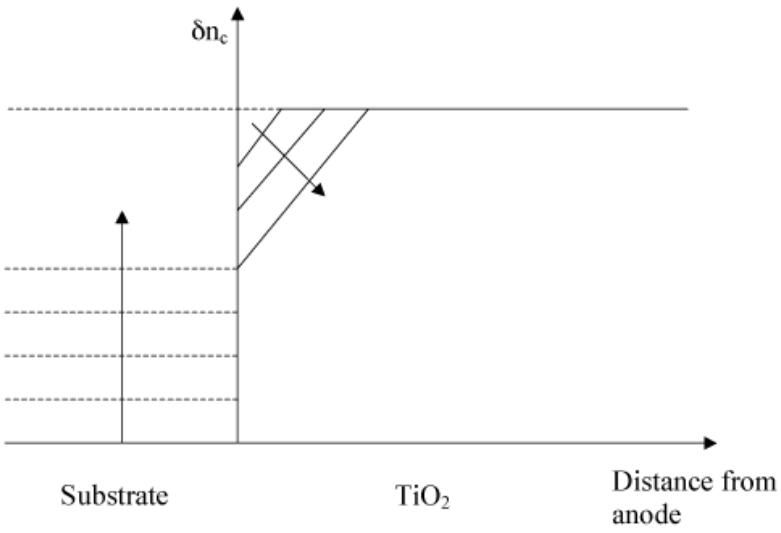

Figure 2.9: Illustration of the excess conduction band electron density, δn_c, at the extracting electrode of a DSSC. The solid horizontal line represents the factor $\exp\left(\frac{eV_{oc}}{k_BT}\right)$ and the boundary condition, equation 2.13 assumes that the current will stop flowing when enough electrons have flowed into the substrate to raise the density there by the same factor. The arrows indicate advancing time and show the increasing density in the substrate and the decreasing value of $n_c(0,t)$.

maximum and then decrease due to recombination. An example experimental trace can be seen in figure 2.11 and shows a maximum at approximately 5μs after a fast rise, followed by a slower fall, determined by the decay of the extra photogenerated charges above the background illumination level.

Figure 2.11 shows that the current into the substrate of the solar cell goes smoothly to zero when the substrate capacitance has been charged to a level where its Fermi level reaches that of the illuminated TiO_2. However, in the simulation results that have been presented so far this is not the case. For example, figure 2.12 shows a photocurrent transient for the parameters in table 2.1 and $k_{ext} = 10^4 s^{-1}$, which makes it clear that the boundary condition as implemented thus far does not allow for smooth transition when the substrate capacitance becomes charged up to that in the TiO_2.

The factors considered above indicate that the successful simulation of the photovoltage decay cannot be simulated using the precise methodology presented above.

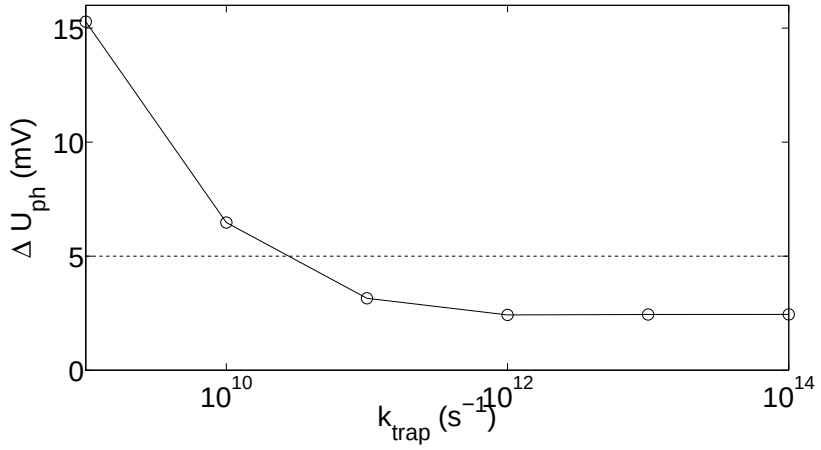

Figure 2.10: The photovoltage heights for the same data considered in figure 2.7.

2.4.3 Space charge effects in nanocrystalline TiO_2 electrodes

It has recently been reported that there may be a barrier for the extraction of electrons [66] at the substrate in DSSCs. Additionally, references [67] and [68] have explored the effects of non-negligible electric fields, which have been neglected so far in this work. These references show that for a complete description of the performance of the DSSC, the effect of the electrostatic potential in terms of band bending and band offsets cannot be completely ignored. However, it should be noted that for almost all situations of interest, the field-free model has been shown to correctly reproduce experimental data [58, 61].

Throughout the preceeding discussions of the DSSC, it has been assumed that electric fields are negligible and that electron transport in the device is purely diffusive. The possible influence of an electric field internal to the TiO_2 grains in the solar cell is now considered. The grains can be well approximated by spheres of radius ∼20nm and dielectric constant, $\epsilon_r = 30$ and it will be assumed in this discussion that they contain 10^{24} donor centres per cubic metre, corresponding to ionised oxygen atoms. In an isolated, doped TiO_2 grain, the Fermi level is just below the conduction band [21] and that of the electrolyte redox couple is approximately 1eV below the same conduction band level [21, 58, 61]. In order to maintain electrochemical equilibrium (i.e., Fermi level continuity) electrons will be transferred to the electrolyte when the TiO_2 grain is placed into the electrolyte. Due to the presence of the oxygen, this flux will give rise to an uncompensated positive space charge on the grain. Assuming that all of the excess electrons have left the grain, the net charge density in the TiO_2 will simply be equal to the number of donor atoms, N_d.

Solving the Poisson equation analytically will give a feel for the possible band-bending

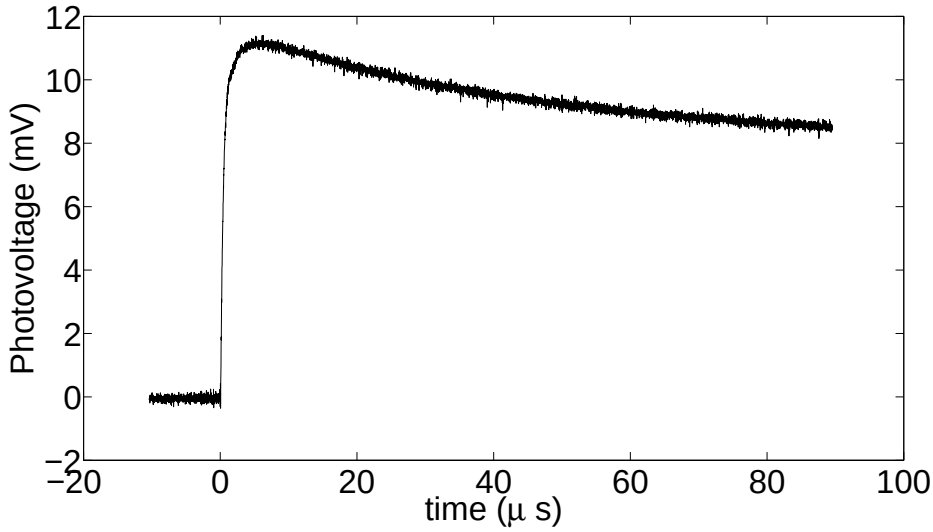

Figure 2.11: Experimental photovoltage transient for a DSSC illuminated with an 8ns pulse at V_{oc}=566mV.

in the TiO_2, which will be further examined later [69, 21]. Inside the sphere (of radius R) the Poisson equation can be written using spherical polar coordinates. Assuming spherical symmetry, only the radial component of the Poisson equation needs to be considered,

$$\nabla^2\psi = \frac{\partial^2\psi}{\partial r^2} + \frac{2}{r}\frac{\partial\psi}{\partial r} = \frac{-\rho}{\epsilon_0\epsilon_r} = \frac{-eN_d}{\epsilon_0\epsilon_r}, \tag{2.41}$$

where ρ is the charge density and the first equality follows from the expression of ∇^2 in spherical polar coordinates. Outside the sphere where $\rho = 0$,

$$\frac{\partial^2\psi}{\partial r^2} + \frac{2}{r}\frac{\partial\psi}{\partial r} = 0. \tag{2.42}$$

This has the general solution

$$\psi = \frac{a}{r} + b, \tag{2.43}$$

where a and b are constants. The constant b can be set to zero because the position of the ground (where the potential is zero) does not affect the outcome of the electric field calculation and so the zero of potential is set at infinity. Far from the sphere of charge, the sphere will appear as a point charge and therefore

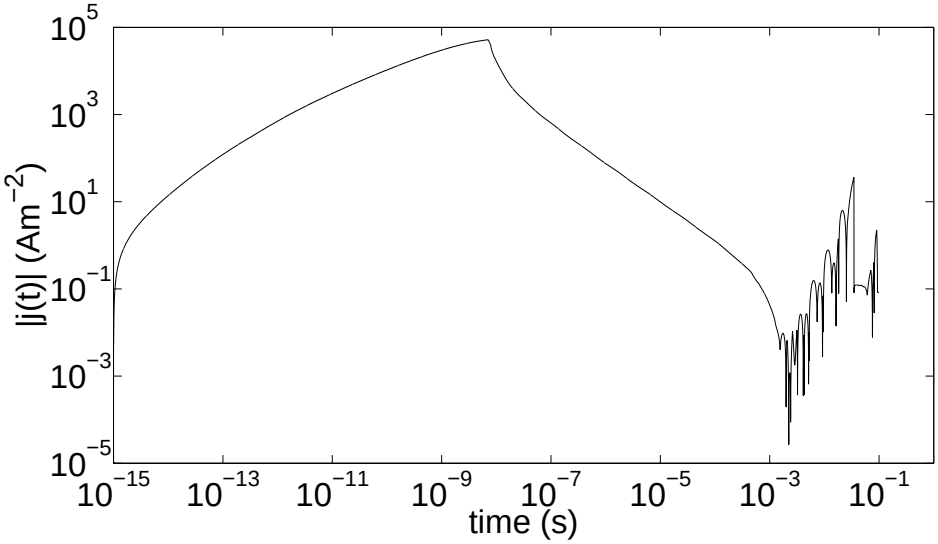

Figure 2.12: Simulated photocurrent transient for a DSSC illumination with an 8ns pulse, the parameters in table 2.1 and $k_{ext} = 10^4 \mathrm{s}^{-1}$.

$$a = \frac{Q}{4\pi\epsilon_0\epsilon_r}, \tag{2.44}$$

which yields

$$\psi = \frac{Q}{4\pi\epsilon_0\epsilon_r r}, \tag{2.45}$$

which is the standard result for the Coulomb potential of a point charge, Q, where

$$Q = \frac{4}{3}\pi R^3 \rho. \tag{2.46}$$

Inside the grain, there is a constant term on the left hand side of the Poisson equation, equation 2.41. Solving this equation and equating ψ at the surface of the grain ($r = R$) gives

$$\psi = \frac{\rho}{6\epsilon_0\epsilon_r}\left(R^2 - r^2\right) + \frac{\rho R^2}{3\epsilon_0\epsilon_r} = \frac{eN_d}{6\epsilon_0\epsilon_r}\left(R^2 - r^2\right) + \frac{eN_d R^2}{3\epsilon_0\epsilon_r}. \tag{2.47}$$

Substitution of the parameters given above gives a difference in the potential of 40mV between the centre and the outer edge of the sphere. Since the potential varies as

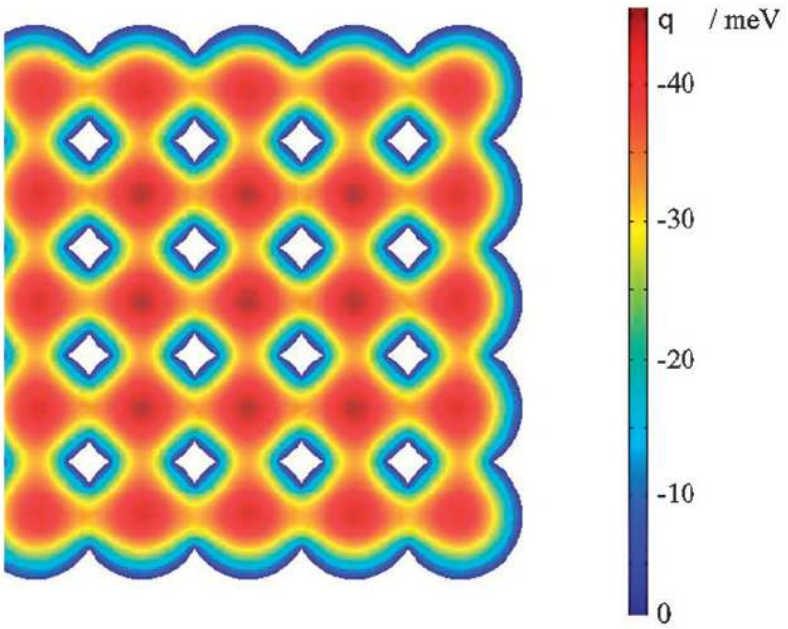

Figure 2.13: Illustration of the electron potential energy (in meV) in an ensemble of 20nm TiO_2 particles for the parameters discussed above.

$\psi \sim -r^2$, the electron potential energy will vary as $+r^2$ and conduction electrons will tend to be drawn away from the surface of the grains where recombination with tri-iodide molecules occurs. This could have important implications for DSSCs where the grains are large and/or where the doping density is high. This is because the potential difference between the centre and edge of the particles increases proportionately with these quantities. Figure 2.13 shows an example for an ensemble of TiO_2 grains for the same parameters given above. A lattice of low potential energy pathways can be seen in this figure, which may help funnel the conduction electrons to the anode where they can be extracted with a lower recombination probability. This effect may help to explain recent findings in the literature that electron diffusion lengths in DSSCs may be significantly longer than previously thought [70].

Due to the complicated structure of the TiO_2 matrix, some simplification is often required in the process of simulation. For example, reference [68] considers a columnar, cylindrical geometry to represent the TiO_2 particles in contact with the substrate. This is done to enable calculation of the dark electric potential profile and hence the resultant electric field. These calculations are included here since the value of the dielectric constant used in reference [68] is $\epsilon_{r,rutile} \approx 130$; that of rutile TiO_2. However, the polymorph of TiO_2 used in the DSSC of interest here is the anatase form, which has $\epsilon_{r,anatase} \approx 30$.

For illustrative purposes, the effect of changing the values of the doping density and the dielectric constant is examined with respect to the results in reference [68]. Dirichlet boundary conditions are used at all boundaries in reference [68] and identical conditions are used here. Specifically, at the substrate (junction) side,

$$\psi_j = -\frac{5k_BT}{e} \tag{2.48}$$

and at the other surfaces,

$$\psi_s = -\frac{15k_BT}{e}. \tag{2.49}$$

Firstly, the effect of the dielectric constant on a column of radius 20nm and length 200nm is considered. An exact comparison with reference [68] is precluded here because the radius of column therein is set equal to the Debye length, L_D,

$$L_D = \sqrt{\frac{\epsilon_0\epsilon_r k_BT}{N_d e^2}}. \tag{2.50}$$

Here, N_d is the doping density inside the column and the number of free electrons is assumed to be negligible. Therefore, if the doping density or dielectric constant is changed, the resulting radius of the column is changed also, and there is no net effect on ψ. Figure 2.14 shows the distribution of electric potential along the axis of cylinder for different values of the doping density and dielectric constant.

All values of N_d and ϵ_r give similar shapes in the electric potential profile. The parameters originally considered in reference [68] are represented in figure 2.14 by the dotted line. Using this result as the basis for comparison, it can be seen that changing the dielectric constant to that of anatase TiO_2 has very little effect on the potential profile in the device apart from giving a slightly higher bulk value.

A marginally greater effect on the potential can be seen than that considered above when the doping density is increased by a factor of 10 to $10^{24}\mathrm{m}^{-3}$ and $\epsilon_{r,rutile}$ is used. This is because the order of magnitude increase in N_d gives a relatively larger change in the source term of the Poisson equation than the relative change in ϵ_r (130/30≈4) considered above.

The most striking effect occurs when the dielectric constant is decreased *and* the doping

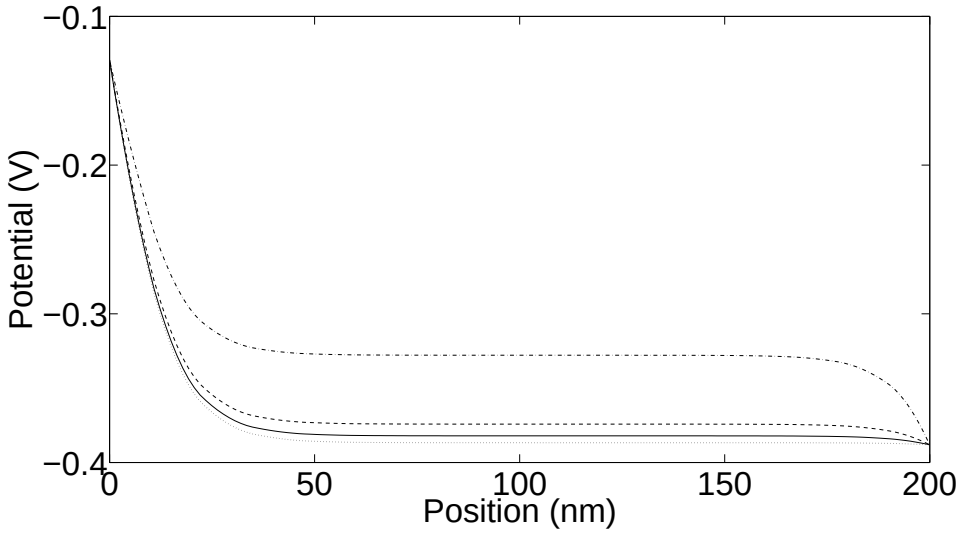

Figure 2.14: Electric potential along the cylindrical axis for N_d=10^{23}m^{-3}, $\epsilon_{r,anatase}$ $(-)$, N_d=10^{23}m^{-3}, $\epsilon_{r,rutile}$ $(\cdot\cdot)$, N_d=10^{24}m^{-3}, $\epsilon_{r,anatase}$ $(\cdot - \cdot)$, N_d=10^{24}m^{-3}, $\epsilon_{r,rutile}$ $(--)$. The radius of the cylinder is 20nm.

density is increased. These both act to exacerbate the rate of change of band curvature, as given by the Poisson equation. Most interesting of all however is the appearance of a significant band bending at the counter electrode (right hand side) of the device. This may act to aid collection of electrons generated far from the extracting electrode at the left hand side of the device. This is because the resultant electric field at the counter electrode is such that it will sweep electrons towards the extracting electrode. This effect is well-known in the field of inorganic solar cells and is called a 'back surface field' [2]. This assertion that a high doping density may act to improve device performance is in agreement with the result obtained above, which saw that low potential energy pathways through the centre of the quasi-spherical TiO_2 could be created by increasing the value of N_d. In addition, this section shows that for a correct consideration of the photovoltage rise time in a DSSC the band structure at the extracting electrode must be considered.

2.5 Conclusions and further work

The transport time in a DSSC at open circuit has been successfully shown to obey the diffusion limit given by the quasi-static approximation under the conditions of fast extraction. However, the reproduction of the photovoltage rise time was not so favourable. This has been attributed to the neglection of band bending effects and to the breakdown of an implicit assumption in the boundary condition for charge extraction. Electrostatic effects are frequently ignored in the literature, however, it has

been shown here that electric fields may be beneficial to device performance in two ways. Firstly, the quasi-spherical nature of the TiO_2 matrix could mean that electrons are kept away from the grain surface, thus reducing recombination and increasing L_n. Secondly, high doping densities may set up a 'back surface field' in the device, causing electrons generated near the counter electrode to be more efficiently collected at the extracting electrode. These effects may support recent results showing that electron diffusion lengths in DSSCs may be significantly longer than previously reported.

Part II: Organic solar cells and OLEDs

Chapter 3

Simulation of ideal morphology polymer solar cells

Much research has taken place in recent decades on organic solar cells with bulk heterojunction morphologies. However, recent work has shown that the most effective geometry at harvesting sunlight is formed from interpenetrating fingers of donor and acceptor materials [33], which will be termed an ideal morphology throughout this work. This type of geometry has also been documented for hybrid inorganic-organic devices made from conjugated polymers and inorganic materials such as TiO_2 [32]. This chapter presents time-independent simulations of these devices where the two active phases are both polymeric in nature. Particular attention is paid to the influence of the intermediate polaron pair charge-transfer state on device performance as well as the effect of space charge on the open circuit voltage.

3.1 π-conjugated organic polymers

Figure 3.1 shows some commonly used organic polymers. Technically, a conjugated organic polymer is a carbon-containing long chain molecule where there is alternation between single and multiple (often double) carbon-carbon bonds [3]. It consists of many repeat units where the unit cell is known as a monomer. It is of interest to consider the electronic structure of an isolated carbon atom before considering the solid state. The atomic state of carbon, isolated from any other outside influence is $1s^2 2s^2 2p^2$. However, the energy of an ensemble of carbon atoms can be lowered if the electronic configuration is altered from this state. This fundamental principle is the basis of the chemical bond [71].

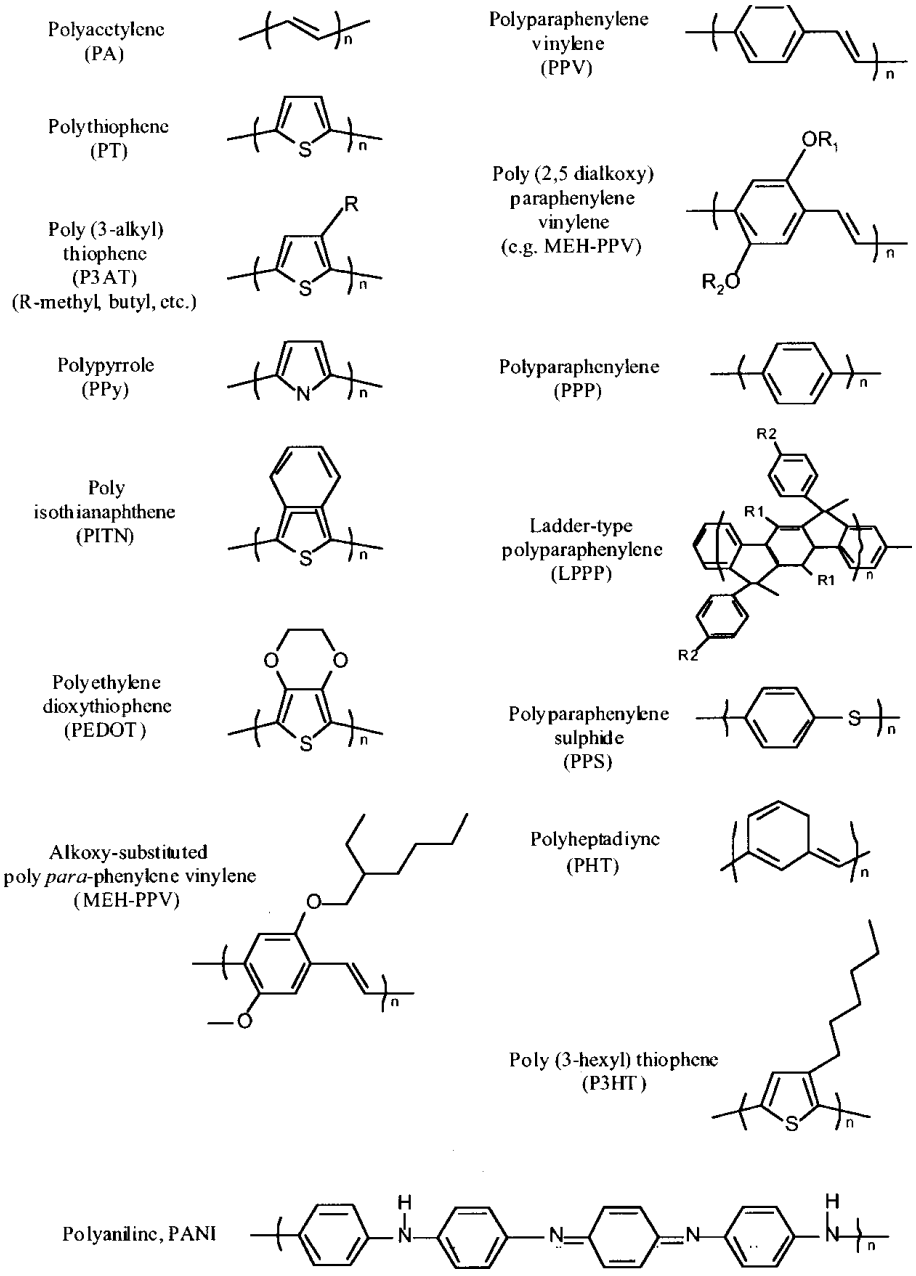

Figure 3.1: Some examples of chemical structures of conjugated polymer materials, from [3].

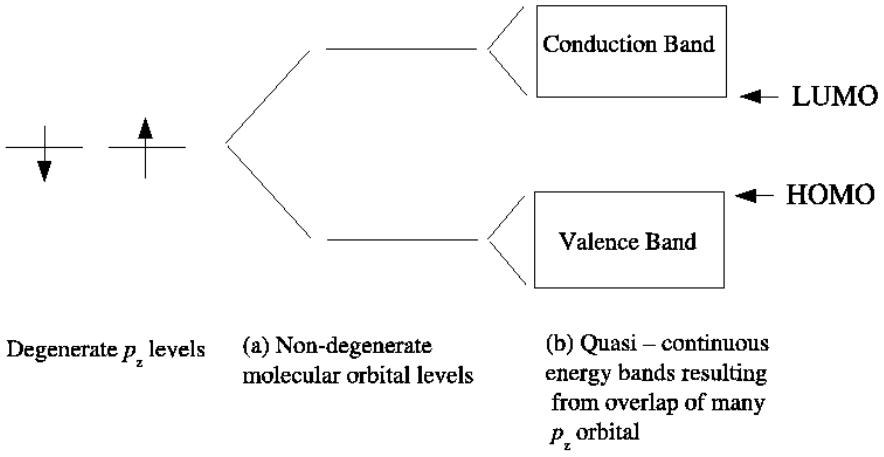

Figure 3.2: The evolution of the bandstructure of organic materials, from the isolated atomic picture on the left to the solid state on the right, adapted from [12].

Now consider the promotion of an electron from the filled $2s$ shell, giving $1s^2 2s 2p^3$. This change of electronic structure requires about 6eV of energy. The formation of covalent bonds between neighbouring carbon atoms, however, reduces the energy by more than 6eV, thus making this latter structure energetically favourable. In his lectures on this subject [24], Alan Heeger notes that a key realisation in the development of conjugated polymers was that the resulting electronic structure of polyacetylene - the simplest conjugated polymer - is similar to that of a semiconductor. This fundamental structure consists of extended conduction and valence bands separated by a bandgap. There is now one unfilled s orbital and three filled p orbitals. These states can now form hybridised structures [12]. Three covalent bonds are formed from the three hybridised sp^2 orbitals with the two carbon atoms on either side of the atom in question, and one with another atom or chemical moiety. These bonds (the σ bonds) give the materials their structural stability. There is now one valence electron left per atom, and these electrons form a delocalised p_z orbital band, known as a π-band, when many atoms are in close proximity and this is illustrated in figure 3.2. Optoelectronic transitions can now be made between the highest occupied molecular orbital (HOMO), or π orbital to the lowest unoccupied molecular orbital (LUMO), or π^* band [3]. The analogy with standard semiconductor conduction and valence bands is clear from figure 3.2.

Optical excitations between π electron states are structurally stable since the σ bonds are unaffected. Indeed, if an electron were excited between the σ bands then the material would degrade and become a photoresist since the structural backbone of the polymer would come apart [24]. For polyacetylene, virtually all photoexcitations are within the π bandstructure because the σ-σ^* splitting is $\sim$10eV.

The device characteristics upon which this work is based involve the solution of partial differential equations. These involve the transport of electrons, holes and excitons, the injection of electrons and holes at the interface between the transport materials and the metallic electrodes, generation and recombination of electrons and holes and the interaction between charges resulting in a distribution of electric potential. All these coupled equations are solved self-consistently.

3.2 Electrons and holes in organic semiconductors

Firstly, the transport of charge carriers in organic semiconductors is considered. The standard form of the drift-diffusion equations, as used throughout the simulations of organic devices herein are given by

$$J_{n(p)} = e\mu_{n(p)}n(p)E + (-)eD_{n(p)}\nabla n(p) \tag{3.1}$$

for electrons (holes). $J_{n(p)}$ is the electron (hole) current density, e is the magnitude of the electron charge, $\mu_{n(p)}$ is the electron (hole) mobility, $n(p)$ is the electron (hole) density, E is the electric field in the device and $D_{n(p)}$ is the electron (hole) diffusion coefficient. The mobility and diffusion coefficient are connected via the Einstein relation

$$\frac{D}{\mu} = \frac{k_B T}{e}, \tag{3.2}$$

which is used throughout this work, although it has been shown that the diffusion coefficient can be enhanced at high charge densities [72]. The electric field, E, is related to the electric potential, ψ through

$$E = -\nabla\psi \tag{3.3}$$

and the potential is found from the solution of the Poisson equation,

$$-\nabla^2\psi = \frac{e\,(p-n)}{\epsilon_0\epsilon_r}, \tag{3.4}$$

where $\epsilon_0\epsilon_r$ is the product of the permittivity of free space and the dielectric constant.

This combination of equations is very widely used in the literature [55, 73, 74, 75, 76, 77].

The short circuit boundary conditions on the Poisson equation used here are given by

$$\psi = -\phi_{Bn}, \tag{3.5}$$

and in a multi-layer structure, the difference in the electron affinities must be taken into account at opposite sides of the device. In equation 3.5, ϕ_{Bn} is the barrier for electron injection into the semiconductor and the boundary conditions on equation 3.1 are considered in detail in section 3.3. When a bias is applied to the device, the potential boundary condition at one side needs to be altered to give,

$$\psi = -\phi_{Bn} \pm V_a, \tag{3.6}$$

where V_a is the value of the bias. The reason for the $\pm$ in equation 3.6 is that the definition of 'forward bias' is poorly defined in the literature and it is often implied that 'forward bias' and 'positive bias' are synonymous. This can be shown to be false by noting that a positive bias on one side is equivalent to a negative bias at the opposite side. The correct definition of forward bias is one that acts to oppose the built-in field in the device. The quantity, V_{bi} is defined as the potential difference between the electrodes at zero applied bias.

The electron and hole transport equations can also be used for the simulation of inorganic devices [1] where disorder is small. However, in organic materials where disorder is present [19], the mobility is parameterised by a form which depends on the electric field,

$$\mu_{n(p)} = \mu_{n(p)0} \exp\left(\gamma\sqrt{E}\right), \tag{3.7}$$

where γ is a material dependent constant. This functional form has been derived by considering the interactions of electrons and holes with permanent dipoles of random position within the organic material [78].

The fundamental processes in the bulk of a semiconductor system are transport, recombination and generation and can be represented by the continuity equations,

$$\frac{\partial n(p)}{\partial t} = G_{n(p)} - R_{n(p)} + (-)\frac{1}{e}\nabla \cdot J_{n(p)}, \tag{3.8}$$

where the electron (hole) current, $J_{n(p)}$ is given by equation 3.1 and $G_{n(p)}$ and $R_{n(p)}$ are the electron (hole) generation and recombination rates [1].

3.3 Organic-metal interfaces

Firstly, the potential energy of an electron near a metal interface in the presence of an image potential and an applied electric field, E, is considered. Throughout this discussion, electrons will be considered. However, entirely analogous expressions exist for holes. The potential near the interface is described by

$$\psi(x) = \phi_{Bn} - Ex - \frac{e}{16\pi\epsilon_0\epsilon_r x}, \tag{3.9}$$

where x is the distance between the metal and the charge, ϕ_{Bn} is the Schottky barrier height [1] and the zero of potential is taken as the metal work function.

Figure 3.3(a) illustrates that the application of an externally applied field (of the correct sign) will give a reduction in barrier height for charge injection. This barrier reduction is given by differentiating the expression for the potential in equation 3.9. This gives the distance, x_M at which the potential is a maximum,

$$x_M = \left(\frac{e}{16\pi\epsilon_0\epsilon_r E}\right)^{1/2}. \tag{3.10}$$

Substituting this into equation 3.9, gives the barrier height reduction for charge injection from the metal work function, Φ_M, as a function of applied electric field, $\Delta\phi_{Bn}^{-}$,

$$\Delta\phi_{Bn}^{-} = \left(\frac{eE}{4\pi\epsilon_0\epsilon_r}\right)^{1/2}. \tag{3.11}$$

Some care needs to be exercised when applying the Schottky lowering formula, since equation 3.11 only applies for a certain sign of the electric field [77]. Considering an electron at the interface given in equation 3.3, the Schottky effect only applies if the

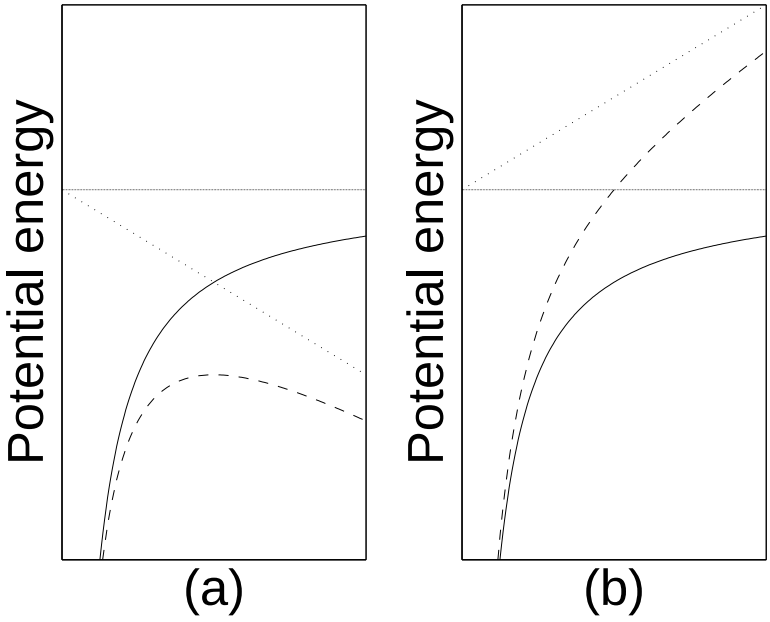

Figure 3.3: Schematic diagram of the potential energy of an electron near a metal electrode for (a), when the Schottky effect is valid (and the barrier for injection is lowered) and (b), for the opposite sign of the field (where the barrier height is increased). The dotted lines show the potential energy due to a constant applied field, the solid line shows the Coulomb potential (the last term in equation 3.9) and the dashed line gives total potential. In (b) the $-E_x$ term in equation 3.9 is replaced by $+E_x$. In both cases the solid central horizontal line is the barrier height without the Schottky effect or applied field.

energy of the particle decreases as it moves away from the interface [79]. This becomes clearer if figure 3.4 is considered, which shows a single layer device band diagram at different bias conditions. This lowering of energy as charges move away from the electrodes corresponds to electrons drifting 'downhill' and holes drifting 'uphill' in standard band diagrams, such as figure 3.4. This is because of the difference in sign of the charge on an electron and a hole.

In band diagrams, the top line represents the conduction band, E_C, or the lowest unoccupied molecular orbital, LUMO, in organic materials. The bottom line is the valence band, E_V, or highest occupied molecular orbital, HOMO. These bands represent the potential energy of carriers, that is

$$E_C \sim -\psi + \text{constant} \tag{3.12}$$

and

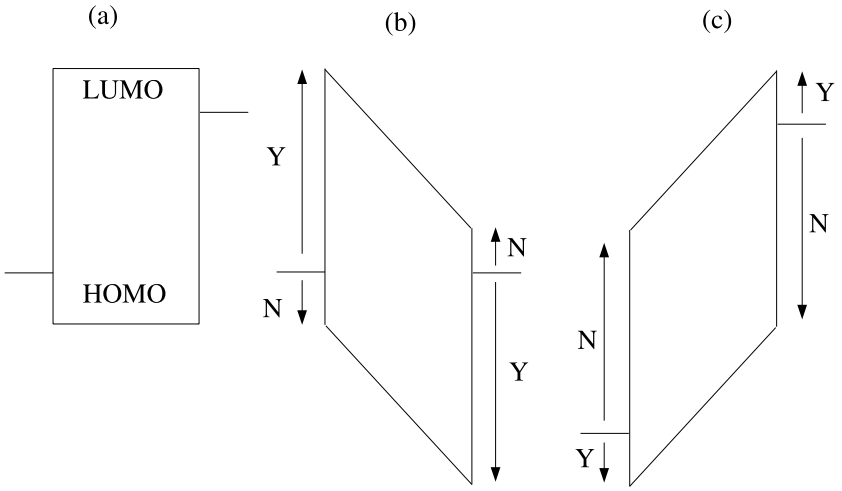

Figure 3.4: Band diagrams for a single layer organic device at (a) flat band, (b) short circuit and (c) $V_a > V_{bi}$, where the bands are tilted in the opposite direction to that at short circuit. At each possible injection site, the letters **Y** and **N** indicate whether or not Schottky lowering is appropriate. The case illustrated in (c) will be where the Schottky lowering has the most pronounced effect on device performance since in this case the barrier lowering is applicable to the smaller barrier at each electrode interface.

$$E_V \sim -\psi - E_g + \text{constant}. \tag{3.13}$$

E_g is the bandgap of the material, and since no equations used in this work depend on the value of the potential, ψ, only its gradient, the constant is set equal to zero without any loss of generality.

3.3.1 The Scott-Malliaras formalism

To simulate the injection and extraction of electrons and holes at the electrodes the model of Scott and Malliaras is used [80, 81]. This is a physically realistic model based on the recombination of charges with their electrostatic images in the metallic electrode. The flux of charges from organic to metal is calculated by considering that the average charge which approaches the metal will recombine with its electrostatic image in the metal if the binding energy exceeds the thermal energy, k_BT. This occurs at a distance,

$$x_C = \frac{e^2}{16\pi\epsilon_0\epsilon_r}. \tag{3.14}$$

In this work it is the behaviour away from equilibrium that is of interest and hence the form of the injected and extracted currents at non-zero applied electric field is required. In the regime where Schottky lowering is appropriate, it can be shown [80, 82] that the current density across the metal-organic interface is given by the difference of the current densities injected into, and extracted from the organic material, J_{inj} and J_{rec},

$$\begin{aligned} J_n &= A^* T^2 \exp\left(\frac{-e\phi_{Bn}}{k_B T}\right) \exp\left(\sqrt{f}\right) - neS(E) \\ &= J_{inj} - J_{rec} \end{aligned} \tag{3.15}$$

where

$$S(E) = S(0)\left(1/\psi(f)^2 - f\right)/4 \tag{3.16}$$

is the field-dependent recombination velocity and

$$S(0) = \frac{16\pi\epsilon_0\epsilon_r k_B^2 T^2 \mu_n}{e^3}, \tag{3.17}$$

is the value at zero field. In equations 3.15 and 3.16, f is the so-called reduced field [80, 81]

$$f = \frac{e^3 E}{4\pi\epsilon_0\epsilon_r k_B^2 T^2} \tag{3.18}$$

and

$$\psi(f) = f^{-1} + f^{-1/2} - f^{-1}\left(1 + 2f^{1/2}\right)^{1/2}. \tag{3.19}$$

Equations 3.16 and 3.19 are derived in Appendix A. The standard theory for Schottky barrier lowering is used in equation 3.15 and the injected current density is given by,

$$
\begin{aligned}
J_{inj} &= A^* T^2 \exp\left(\frac{-e\left(\phi_{Bn} - \Delta\phi_{Bn}^{-}\right)}{k_B T}\right) \\
&= A^* T^2 \exp\left(\frac{-e\left(\phi_{Bn} - \sqrt{\frac{eE}{4\pi\epsilon_0\epsilon_r}}\right)}{k_B T}\right) \\
&= A^* T^2 \exp\left(\frac{-e\phi_{Bn}}{k_B T}\right) \exp\left(\sqrt{\frac{e^3 E}{4\pi\epsilon_0\epsilon_r k_B^2 T^2}}\right) \\
&= A^* T^2 \exp\left(\frac{-e\phi_{Bn}}{k_B T}\right) \exp\left(\sqrt{f}\right), \qquad (3.20)
\end{aligned}
$$

where equation 3.11 has been used to define the Schottky barrier lowering.

Image force lowering of the thermionic emission barrier is only applicable at one particular sign of the field. The effect when the field changes sign has been considered in reference [55] and this formalism is used here. The premise of the argument is that for signs of the field where the Schottky effect is not valid, the binding energy between the injected carrier and its image charge must be less than or equal to $k_B T$ for the injected charge to escape recombination. This is shown in figure 3.3(b) where it can be seen that there is no peak in the total potential profile. It is because of this lack of maximum in the potential that the notion of escaping recombination is invoked since injection into the potential profile in figure 3.3(b) will be more difficult for a finite applied bias [55]. The magnitude of the increase in barrier height, $\Delta\phi_{Bn}^{+}$, is given by equation 3.21.

$$
\Delta\phi_{Bn}^{+} = \frac{e^2 E}{16\pi\epsilon_0\epsilon_r k_B T}, \qquad (3.21)
$$

and so, since the recombination velocity takes its zero field value [55] in this regime,

$$
\begin{aligned}
J_n &= A^* T^2 \exp\left(\frac{-e\phi_{Bn}}{k_B T}\right) \exp\left(-\frac{f}{4}\right) - neS(0) \\
&= J_{inj} - J_{rec}. \qquad (3.22)
\end{aligned}
$$

In equation 3.22, the injected component can be written in terms of f because,

$$
\begin{aligned}
J_{inj} &= A^* T^2 \exp\left(\frac{-e\left(\phi_{Bn} + \Delta\phi_{Bn}^{+}\right)}{k_B T}\right) \\
&= A^* T^2 \exp\left(\frac{-e\left(\phi_{Bn} + \frac{e^2 E}{16\pi\epsilon_0\epsilon_r k_B T}\right)}{k_B T}\right) \\
&= A^* T^2 \exp\left(\frac{-e\phi_{Bn}}{k_B T}\right) \exp\left(-\frac{e^3 E}{16\pi\epsilon_0\epsilon_r k_B^2 T^2}\right) \\
&= A^* T^2 \exp\left(\frac{-e\phi_{Bn}}{k_B T}\right) \exp\left(-\frac{f}{4}\right). \qquad (3.23)
\end{aligned}
$$

Equation 3.21 has been used here to define the increase in injection barrier height in this regime.

3.4 Excitons in organic semiconductors

Next, the exciton population in organic devices is considered. Since excitons are charge neutral, they move only by diffusion. The continuity equation [83] describing the density of excitons is

$$
\frac{\partial S}{\partial t} = \nabla \cdot (D_{exc} \nabla S) - \frac{S}{\tau_{exc}} + \frac{Q}{\hbar\omega}, \qquad (3.24)
$$

where $S_{n(p)}$ is the density of excitons in the acceptor (donor), D_{exc} is the exciton diffusion coefficient, τ_{exc} is the exciton lifetime, Q is the energy dissipated by the optical excitation per unit volume per unit time, $\hbar$ is Planck's constant divided by 2π and ω is the angular frequency of the light [84]. The exciton diffusion length, L_{exc} is given by

$$
L_{exc} = \sqrt{D_{exc}\tau_{exc}}, \qquad (3.25)
$$

and is the average distance an exciton diffuses before decaying. The excitons are assumed to be perfectly quenched (separated) at the polymer-polymer interface and the electrodes. At the electrodes, however, excitons will recombine non-radiatively and will not give a contribution to the photocurrent [85]. Therefore, at the heterojunction and at the electrode,

$$S = 0. \tag{3.26}$$

The dissociation of excitons at the interface between two polymers has been considered in detail for a bilayer structure [55] and the same formalism is used here. It is assumed that within 1nm of the interface, the excitons dissociate into a so-called polaron pair, which straddles the junction but remains bound and immobile [86]. This polaron pair can then either recombine back into an exciton with rate constant k_{rec}, or dissociate with the electric field-dependent rate $k_{diss}(E)$. Polaron pairs can also be formed from recombination of free charges, so that the areal density (number per unit area) of polaron pairs, X, at the interface can be described by

$$\frac{\partial X}{\partial t} = G_X - k_{rec}X - k_{diss}(E)X + F_X. \tag{3.27}$$

Here, G_X is the polaron pair generation rate from exciton dissociation and F_X is the rate of formation from the capture of free charge [55]. F_X is described by a Langevin-like rate [87] using the smaller of the two majority carrier mobilities, μ_{small}, as has been recently used to describe the behaviour of polymer-fullerene blends [88]. The width of the charge generation region at the interface, h, is 1nm, and

$$F_X = \frac{n_{int}p_{int}h\mu_{small}e}{3\epsilon_0\epsilon_r}, \tag{3.28}$$

where $n(p)_{int}$ is the value of the electron (hole) density at the polymer-polymer interface.

The reason for this dependence on the smaller of the two mobilities instead of the original Langevin dependence on the sum is due to the majority carriers being confined to the separate materials. Therefore, for recombination to occur, a charge sitting at the interface has to wait for a charge of opposite sign to approach it before recombination can occur. Hence the recombination is controlled by the smaller of the two mobilities. Langevin recombination of electrons and holes is considered in each bulk material, but it is found to be negligible compared with other processes as found previously [55]. In the steady state, $\frac{\partial X}{\partial t} = 0$ and therefore

$$X = \frac{G_X + F_X}{k_{rec} + k_{diss}(E)}, \tag{3.29}$$

where the form of G_X is given by the flux of excitons at the interface [83, 89],

$$G_X = D_{exc} \left| \nabla \left(S_n + S_p \right) \right| . \tag{3.30}$$

The coupling of electrons and holes with the excitons is now considered. Using equation 3.27, equation 3.8 is written as

$$\frac{\partial n(p)}{\partial t} = \frac{k_{diss}(E)X - F_X}{h} + (-)\frac{1}{e}\nabla \cdot J_{n(p)}, \tag{3.31}$$

where the term in $k_{diss}(E)X$ and F_X account for polaron pair dissociation and formation from free charges respectively. Care needs to be exercised when considering the coupling between the populations of excitons and free charges via polaron pair recombination. This is because for each polaron pair which recombines only one exciton is created, or, half an exciton in each polymer on average. Therefore equation 3.24 is modified as

$$\frac{\partial S}{\partial t} = \nabla \cdot (D_{exc} \nabla S) - \frac{S}{\tau_{exc}} + \frac{Q}{h\nu} + \frac{\eta_{st} k_{rec} X}{2h}. \tag{3.32}$$

It is important here to consider the spin statistics inherent in the theory of molecular photochemistry. When two spin $\frac{1}{2}$ particles come together they can generate a singlet or a triplet state and they are created in a ratio 1:3 [90]. The factor η_{st} in equation 3.32 accounts for this. Only singlet excitons can recombine radiatively [90] to give luminescence and therefore, absorbed photons can only generate singlets. What this means is that the model contains the population of singlet excitons only. Emission from triplet states is possible and this is known as phosphorescence [91] but this occurs on timescales of several orders of magnitude slower than luminescence in general. The efficiency of luminescence limited LEDs is therefore limited to 25%, and hence η_{st}=0.25. There has been recent interest, however, in enhancing this limit by using phosphorescent emitters where the quantum yield can be enhanced above 25% [92].

Figure 3.5 illustrates the different mechanisms of capture and dissociation in this system. The precise nomenclature in reference [73] has been altered in this figure to emphasise the analogy with reference [55] since it is the latter formalism which is used here. In fact the only significant difference between the two methods is in the calculation of the dissociation rate, k_{diss}. Reference [55] uses a formalism due to Jonscher [93], which considers the dissociation over one hemisphere, or 2πSr, due to the distinct

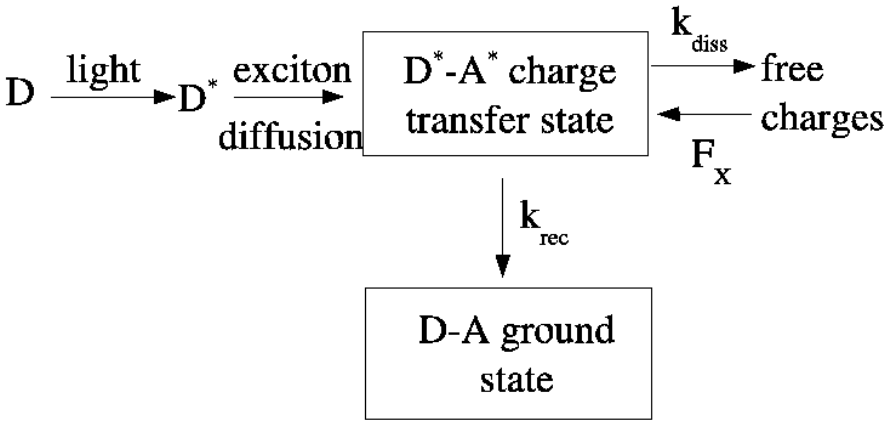

Figure 3.5: Schematic illustration of the different possible states after photon absorption in the donor (D) component of a bulk heterojunction solar cell. Adapted from [73, 94].

material phases present in a bilayer device. However, in the bulk heterojunction case, dissociation can occur over the full 4πSr sphere.

The dissociation rate considered in reference [73] is a modified version of that due to Onsager to describe the recombination and dissociation of ions in solution [95, 96]. The original calculation [96] gave the fraction of pairs of oppositely charged ions which recombine in the presence of an electric field assuming that the transport occurs by Brownian motion [97, 96]. Braun [94] modified this theory to include a non-zero lifetime of the charge transfer state [73]. This means that the intermediate state will not necessarily recombine, should the distance between the pair vanish [94], but can generate free carriers by dissociating with a field-dependent rate $k_{diss}(E)$. The recombination rate is field-independent in all models considered above [55, 73, 94, 95].

The rate of polaron pair dissociation at the heterojunction used here, $k_{diss}(E)$ is given by

$$k_{diss}(E) = \frac{2k_{diss}(0)}{M}\left[\exp\left[M\right]\left(1-\frac{1}{M}\right)+\frac{1}{M}\right], \tag{3.33}$$

for $E < 0$ (the factor of 2 is absent in reference [55]), and by

$$k_{diss}(E) = k_{diss}(0)\frac{4\pi\epsilon_0\epsilon_r k_B^2 T^2}{e^3 E}\left(1-\exp\left(\frac{-e^3 E}{4\pi\epsilon_0\epsilon_r k_B^2 T^2}\right)\right) \tag{3.34}$$

for $E > 0$, where

$$M = \frac{e}{k_B T}\sqrt{\frac{-eE}{\pi\epsilon_0\epsilon_r}}. \tag{3.35}$$

In equations 3.34 and 3.35, E is the average value of the x component of the electric field at the interface. This will be discussed in more detail in section 3.7.

Figure 3.6 illustrates $k_{diss}(E)$ and shows that polaron pair dissociation is reduced, compared to zero field, for positive fields and increased for negative fields. Also in figure 3.6 the dissociation rate for the Onsager formalism is shown [94, 95], $k_{Onsager}$. It can be seen that $k_{Onsager} < k_{diss}(E)$ for negative fields and that $k_{Onsager}$ is an even function of the field. In the simulations presented here, excitons can only be dissociated in one direction, i.e., electrons to the cathode (right) and holes to the anode (left). Electrons (holes) drift to the right (left) in a negative field and therefore, dissociation is enhanced when $E < 0$ [55]. In the case considered by Onsager however, the electrons and holes can move in either direction after dissociation and therefore

$$k_{Onsager}(E) = k_{Onsager}(-E). \tag{3.36}$$

The authors of reference [97] have considered a modified Onsager theory and have shown that interfacial dissociation is increased relative to that in the bulk because the charges are confined to their own material phases. Different functional forms for the dissociation with positive and negative fields are not considered however.

3.5 Photons in organic semiconductors

The main difference between the physics of solar cells to that of OLEDs is that a net generation of charge is necessary to obtain a photovoltaic effect and a net recombination is needed for light emission. The initial photoexcited state in a conjugated polymer is an exciton, so therefore it is necessary to simulate the incoming light in the solar cell and the excitons themselves. Several authors have considered optical effects in organic devices [84, 85, 98, 99] and used matrix methods based upon the fact that the incident light can be considered to only consist of an optical electric field, the tangential component of which is continuous at material interfaces. The essential input parameters are the real (η) and imaginary (κ) parts of the complex, refractive index, $\tilde{n}$,

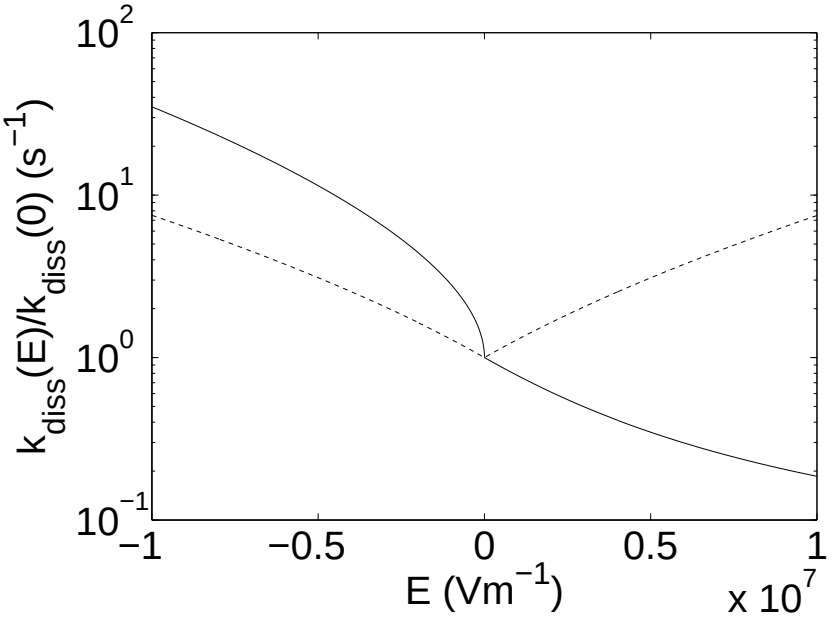

Figure 3.6: The electric field dependence of the polaron pair dissociation rate as used here (solid line) [55] and that due to Onsager (dashed line) [95]. Both forms have been normalised to their values at zero field.

$$\tilde{n} = \eta + i\kappa, \tag{3.37}$$

where $i = \sqrt{-1}$, and the wave equation of interest is that describing the optical electric field in the direction of illumination, $E_{\hbar\omega}$ is

$$\nabla \times (\nabla \times E_{\hbar\omega}) - \tilde{n}^2 k_0^2 E_{\hbar\omega} = 0, \tag{3.38}$$

where k_0 is the free space wavenumber of the light [100].

The boundary conditions on this equation are that $E_{\hbar\omega}$ at the left hand side of the device, $E_{\hbar\omega,g}$ (where the glass substrate meets the rest of the device), is calculated from the reflectance at the interface of the outer glass layer, R^*, and that of the interface of the glass with the rest of the device structure, R [98],

$$E_{\hbar\omega,g} = E_{\hbar\omega,0} \frac{1 - R^*}{\eta_{glass}\,(1 - RR^*)}, \tag{3.39}$$

where $E_{\hbar\omega,0}$ is the optical electric field outside the device. This is necessary because

the millimetre thickness of the glass layer is much thicker than the distance over which the light remains coherent. Because of this fact, at the interface between the glass and the remainder of the device, the amplitudes of the waves must be summed instead of the phases [84]. At the other side of the device, the electric field very quickly falls to zero at the metallic back contact [84]. There is a boundary condition built-in to the **COMSOL** software which enables calculation of this effect and requires the values of the real and imaginary parts of the refractive index of the metal in question. The implementation of the physics contained in this optical modelling is given in appendix C.

3.5.1 Absorption in organic solar cells

In the exciton continuity equation (equation 3.24), the term defining the absorption of photons to generate excitons is given by [98]

$$Q = \frac{1}{2} c \epsilon_0 \alpha \eta E_{\hbar\omega}^2, \tag{3.40}$$

where c is the speed of light and α is the absorption coefficient for a wavelength λ,

$$\alpha = \frac{4\pi\kappa}{\lambda}. \tag{3.41}$$

3.5.2 Emission in OLEDs

Contrary to the case for photovoltaic devices, OLEDs work on the premise that opposite charges injected at the electrodes recombine to gives excitons which then decay to give electroluminescence. As mentioned previously, only a fraction η_{st} of these excitons are able to recombine radiatively. Ultimately, the quantity of interest in the study of OLEDs is the number of charge carrier pairs recombined per charge carrier injected at the contacts. This is given by the internal quantum efficiency, $\eta_{IQE,OLED}$,

$$\eta_{IQE,OLED} = \eta_{st} \frac{J_r}{J_{tot}}, \tag{3.42}$$

where the recombination current, J_r, is the difference between the electron (or hole) current at the anode and at the cathode and J_{tot} is the total device current. The

external quantum efficiency is the number of photons emitted from the device per injected charge and is obtained by multiplying the internal quantum efficiency by the probability of a photon escaping from the device.

3.6 Modelling the open circuit voltage, V_{oc}

The origin and quantification of V_{oc} is an outstanding problem in the field of organic solar cells [101, 102]. Open circuit conditions apply when the current in the external circuit is zero for a non-zero applied bias and illumination intensity. This is when injected and extracted current densities are equal and therefore cancel.

In this section, models describing the open circuit voltages of different types of organic solar cell are described. Bulk heterojunction and bilayer models in the literature are given first before an expression for the idealised morphology considered here is derived.

3.6.1 Bulk heterojunction organic solar cells

A model which successfully describes the current-voltage characteristics of a double Ohmically contacted polymer-fullerene blend device has been published recently [73, 103]. It utilises a drift-diffusion transport scheme, as is standard in continuum models of device behaviour, in an effective medium model. The bandgap is then equal to the difference between the donor HOMO and the acceptor LUMO, termed the internal bandgap, E_{gi}, and the effective medium has a single value for all other relevant material properties such as electron mobility and dielectric constant. This is illustrated in figure 3.7.

An extension of this model to describe the illumination intensity dependence of the open-circuit voltage in polymer-fullerene blend solar cells has been published recently [104]. The key assumption is that the electron and hole quasi-Fermi levels are constant throughout the single layer device at open circuit. The further consideration that generation and recombination must cancel throughout the device gives the following relation for V_{oc},

$$V_{oc} = \frac{E_g}{e} - \frac{k_B T}{e} \ln\left(\frac{(1-P)\,\gamma N_C^2}{PG}\right). \tag{3.43}$$

In equation 3.43, P is the probability of polaron pair (not exciton) dissociation to form

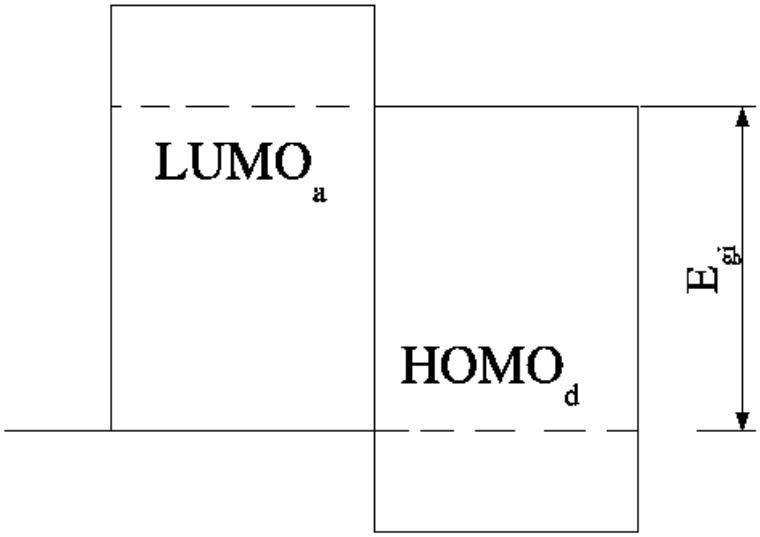

Figure 3.7: Band diagram for the effective medium considered in reference [73]. Ohmic contacts are shown as being barrierless at the electrodes and the internal bandgap, E_{gi}, is shown as being the difference between the donor HOMO and the acceptor LUMO.

free charge carriers, G is the generation rate of polaron pairs and γ is the rate of free charge recombination [87]. Equation 3.43 has been used to accurately simulate the open circuit voltages over two orders of magnitude of intensity.

3.6.2 Bilayer polyfluorene organic solar cells

An analytical expression for the open-circuit voltage in bilayer polyfluorenes has been given in reference [56]. This model first assumes that the electric field in each layer is given by the potential difference across the layer divided by the width, L. Assuming that the electrons are confined to the right of the interface (in one dimension) and the interface defines $x = 0$, from equation 3.1,

$$J_n = e\mu_n n\left(\frac{V_n}{L}\right) + eD_n\frac{\mathrm{d}n}{\mathrm{d}x} = 0. \tag{3.44}$$

which has the solution

$$n(x) = n_{int}\exp\left(-\frac{eV_n}{k_BT}\frac{x}{L}\right), \tag{3.45}$$

where V_n is the potential difference across the electron transporting layer and n_{int} is the electron density at the heterojunction. Assuming that n_{int} is proportional to the illumination intensity, I_0, raised to power α, with proportionality constant k_1,

$$n_{int} = k_1 I_0^{\alpha}, \tag{3.46}$$

the following relationship results,

$$\frac{eV_n}{k_B T} = \alpha \ln(I_0) + \ln(k_1) - \ln(n_c), \tag{3.47}$$

where n_c is the electron density at the cathode ($x = L$). Combining the analogous expression for holes (p_a is the hole density at the anode),

$$\frac{e(V_n + V_p)}{k_B T} \equiv \frac{eV_{oc}}{k_B T} = 2\alpha \ln(I_0) + \ln(k_1 k_2) - \ln(n_c p_a). \tag{3.48}$$

Equation 3.48 reproduces the experimentally seen logarithmic rise in V_{oc} with intensity. However, it underestimates the 80mV rise per order of magnitude in intensity seen in experiment by 20mV, assuming α=0.5 [56]. A numerical simulation study of the same system gives a rise of 55mV [55].

One interesting feature of the open circuit voltage in polyfluorene bilayer cells is that it tends to saturate at high intensity [56], which is not reproduced in the numerical model [55]. The authors speculate that this could be due to accumulation of charges or polaron pairs at the heterojunction causing non-radiative recombination of excitons or influencing the local electric potential such that exciton dissociation requires an energy input.

3.6.3 The intermediate case; ideal morphology organic solar cells

Reference [33] has shown that an interdigitated donor-acceptor morphology can be more efficient that a bilayer or a bulk heterojunction device. This will be referred to as the 'ideal morphology' case in this work and is illustrated in figure 3.8.

The current flowing in a semiconductor can be given by the gradient of the quasi-Fermi level [1], therefore the electron (hole) quasi-Fermi level at the interface and at

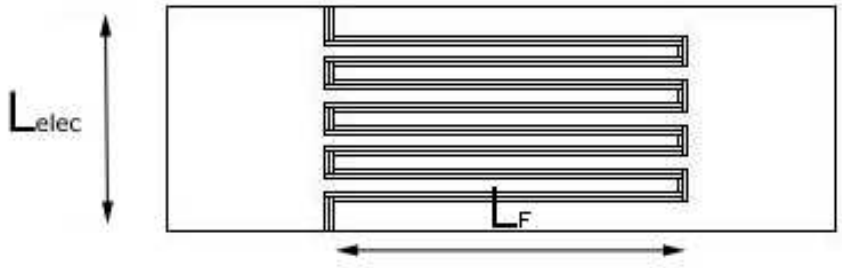

Figure 3.8: Illustration of the morphology used to simulate polymer solar cells. The length of the fingers, L_F, and the electrode length, L_{elec}, are systematically varied. The full device structure is glass substrate/ITO/PEDOT/donor polymer/acceptor polymer/Al. ITO is indium tin oxide and is an electrode material and PEDOT is a polymer improving charge transport across the polymer-electrode interface. This device structure is based on that given in reference [84] for a bilayer organic solar cell.

the cathode (anode) are identical at open circuit. Figure 3.9 shows an energy band diagram of the system considered in this work.

From the definition of the quasi-Fermi level [1], the electron (hole) density at the interface and that at the cathode (anode) can be combined to give

$$\ln\left(\frac{n_{int}p_{int}}{n_c p_a}\right) = \frac{e}{k_B T}\left(\psi_a - \psi_c\right) \tag{3.49}$$

The subscripts *int,* a and c indicate a quantity at the polymer-polymer interface, the anode and the cathode respectively. Following reference [104], the product of the densities at the interface can be written in terms of the areal polaron pair generation rate, G_X and the probability of polaron pair dissociation, P,

$$n_{int}p_{int} = \frac{3\epsilon_0\epsilon_r P G_X}{h\mu_{small}e(1-P)}. \tag{3.50}$$

were h and μ_{small} are defined in equation 3.28.

At open circuit, the potential at the electrodes is given by the boundary conditions for the Poisson equation, equation 3.5,

$$\psi_a = -\phi_{Bna} + V_{oc}, \tag{3.51}$$

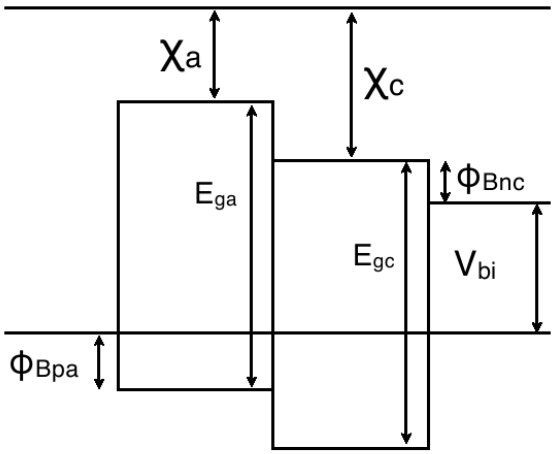

Figure 3.9: Energy band diagram of relevant quantities considered in the derivation of the expression for the open circuit voltage, equation 3.54, where χ is the electron affinity, ϕ_{Bn} is the injection barrier height and E_g is the bandgap. The subscript n refers to electron, p to holes, a to anode (left hand side here) and c to cathode. The top horizontal line refers to the common vacuum level.

$$\psi_c = -\phi_{Bnc} - \chi_c + \chi_a. \tag{3.52}$$

Noting that

$$|V_{bi}| = \phi_{Bna} - \phi_{Bnc} - (\chi_c - \chi_a), \tag{3.53}$$

the open circuit voltage can be written as

$$V_{oc} = |V_{bi}| - V_{th} \ln (n_c p_a) + V_{th} \ln \left(\frac{P}{1-P} \right) + V_{th} \ln \left(\frac{3\epsilon_0 \epsilon_r G_X}{h \mu_{small} e} \right), \tag{3.54}$$

where V_{th} is the thermal voltage,

$$V_{th} = \frac{k_B T}{e}. \tag{3.55}$$

Equation 3.54 can also be recast as a sum of different voltage contributions as

$$V_{oc} = |V_{bi}| + V_{elec} + V_P + V_{G_X}, \tag{3.56}$$

which makes the open circuit voltage data more amenable to examination. All the terms in equation 3.54 can now be ascribed a physical meaning and the open-circuit voltage has been described in terms of deviations from the built-in voltage. The second term on the right hand side of 3.54 shows that the densities of majority carriers at the electrodes should be as small as possible to maximise the quasi-Fermi level splitting between the electrodes and the heterojunction. This in turn will maximise the V_{oc}. The third term shows how the probability of polaron pair dissociation affects the V_{oc} and the fourth term gives the variation of V_{oc} with the dissociation rate of excitons. In this final term, G_X is found to be proportional to intensity and therefore recovers the well known relationship expected from a diode-like current-voltage characteristic, equation 1.5.

Equation 3.54 can be compared to that describing the V_{oc} of a bilayer device in the previous section, equation 3.48. In both cases, photogenerated charges diffuse away from the interface, an electric field counteracting this diffusion is therefore needed to obtain zero current at open circuit.

Equation 3.54 contains a term which varies as $\ln(G_X)$, and it is found below that G_X is very accurately proportional to the illumination intensity. Additionally both expressions for V_{oc} have terms in $-\ln(n_c p_a)$. Reference [56] assumes a voltage, V_n dropped linearly between the polymer-polymer interface and the electrode to obtain $\ln(n_{int}) - \ln(n_c) = \frac{eV_n}{k_B T}$. However, this is the same result used above for the ideal morphology case, under the assumption that the quasi-Fermi level is continuous across the layer, equation 3.49. These two definitions are therefore analogous and the difference in derivation between the two expressions is thus entirely due to the different ways in which the charge densities at the interface are defined. The bilayer case uses $n_{int} p_{int} = k_1 k_2 I_0^{2\alpha}$, whereas the more physically realistic expression, equation 3.50, is used for the ideal morphology case.

This work can therefore be considered as a bridge between the two previous model of references [55] and [73]; a bilayer in the former and a bulk heterojunction in the latter. Both of these models are one-dimensional in nature and therefore cannot describe any morphological dependence of important photovoltaic parameters. Although reference [73] considers a bulk heterojunction device, the effective medium approximation is used. This precludes consideration of, for example, transport of the electrons and holes in their respective phases and the screening of the electric field, which is considered below.

3.7 Simulation methods

In this work polymer-polymer blend solar cells with an idealised, interdigitated morphology are considered. A similar morphology has been recently considered in reference [33] and has been shown to be more efficient than a planar bilayer [55] and even a bulk heterojunction structure. This type of morphology has also been termed an 'ideal ordered bulk heterojunction' to describe hybrid organic-inorganic devices such as those considered in reference [32]. The geometry used for the simulations presented here is illustrated in figure 3.8.

In order to calculate the optical electric field profile in the devices considered here, the following values for the refractive indices are used, which are all for λ =459nm

1. glass: $\tilde{n} = 1.5 + 0$ [105].
2. ITO: $\tilde{n} = 1.9 + 3.8 \times 10^{-3} i$ [105].
3. PEDOT: $\tilde{n} = 1.5 + 2.5 \times 10^{-2} i$ [105].
4. donor: $\tilde{n} = 1.8 + 1.2 \times 10^{-2} i$ [106].
5. acceptor: $\tilde{n} = 1.7 + 6 \times 10^{-1} i$ [106].
6. aluminium: $\tilde{n} = 6 \times 10^{-1} + 5.2 i$ [106].

The ordinary wave values for η and κ from Figure 2 in reference [106] are used for the donor and acceptor values and the values for aluminium are from figure 5 in the same reference. The aluminium refractive index is needed for the boundary condition at the Al electrode where it is known that the optical electric field penetrates only a small distance into the back electrode [100]. Interference effects are included by consideration of both incident and reflected optical waves and an example plot of the optical electric field inside the device is given in figure 3.10. This shows the cancellation of the optical electric field in the close vicinity of the Al back contact.

If the light intensity were assumed to decay exponentially with distance inside the device and interference effects were neglected, then for a given position, x, the light intensity would be the same in each phase respectively. This means that each finger of donor material would have the same intensity at a given value of x. This would apply equally to the acceptor, although the intensities would be different in the two materials because they have different refractive indices. Figure 3.10 shows that this is not the case when the wave equation for $E_{\hbar\omega}$ is solved (equation 3.38) since there is a clear

Parameter	Donor	Acceptor
ϵ_r	4	4
N_C (m^{-3})	10^{27}	10^{27}
N_v (m^{-3})	10^{27}	10^{27}
μ_{n0} ($m^2V^{-1}s^{-1}$)	10^{-12}	3×10^{-10}
μ_{p0} ($m^2V^{-1}s^{-1}$)	10^{-10}	3×10^{-12}
γ ($V^{-1/2}m^{1/2}$)	3×10^{-4}	1.55×10^{-4}
ϕ_{Bn} (eV)	2.3	0.5
ϕ_{Bp} (eV)	0.5	1.9
τ_{exc} (ns)	1	1
D_{exc} (m^2s^{-2})	10^{-7}	10^{-7}
L_{exc} (nm)	10	10

Table 3.1: Simulation parameters for the simulation of idealised morphology polymer blend solar cells. These are as given in reference [55] except for the γ value for the acceptor material.

oscillation in the value of $E_{\hbar\omega}$ in the direction parallel to the electrodes. A comparison of current-voltage characteristics obtained with these two different illumination schemes is performed in section 3.8.2.

Because the excitons have a finite diffusion length, it is desirable to generate excitons as close to the heterojunction as possible. The peaks of the optical electric field in figure 3.10 profile should therefore be close to the junction to maximise the photovoltaic response. Reference [107] has shown that for a bulk heterojunction organic solar cell, the short circuit current can be optimised with respect to the thickness of the active layer and reference [84] has given analogous results for the optimum layer thickness in a bilayer organic solar cell. It would be an interesting extension to this work to examine the relationship between quantum efficiency and device thickness in the intermediate case considered here for an ideal morphology organic solar cell.

Table 3.1 gives the invariant electrical simulation parameters for all morphology schemes used in this chapter.

To calculate the generation and recombination rates for the electrons and holes the model uses the value of the x component of the electric field and the value of the majority carrier concentrations at the polymer-polymer heterojunction [55]. For a distributed junction the value of these quantities at a point cannot be used. This is circumvented by splitting the interface into sections as seen in figure 3.8 and using an average generation rate in each interface subdomain. The electric field (the majority carrier densities are obtained analogously) is calculated from

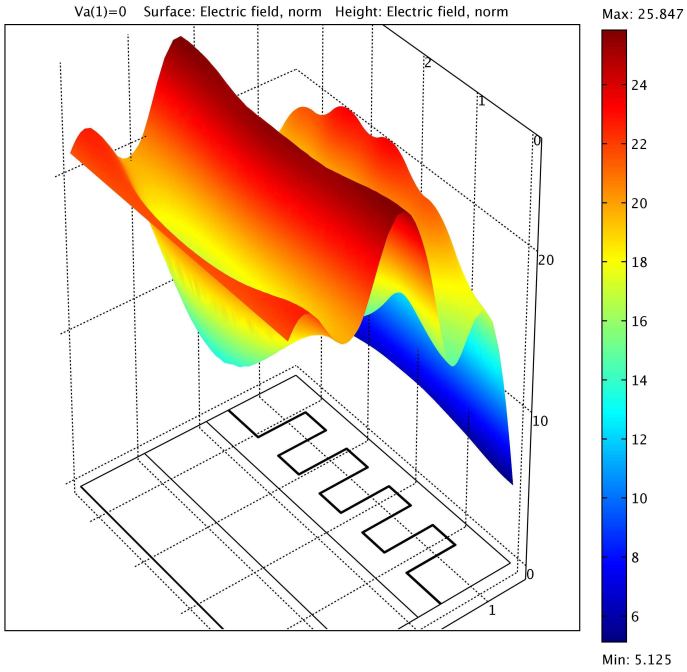

Figure 3.10: Example plot of the magnitude of the optical electric field (in Vm^{-1}) inside a device at 0.1 Sun for the refractive indices given on page 74, L_{elec}=440nm and L_{int}=1072nm. The figure also illustrates the underlying device morphology.

$$\bar{E}_{x(y)} = \frac{\int_0^l E_{x(y)} dx(y)}{\int_0^l dx(y)}, \tag{3.57}$$

where l is the length of the interface region in question. It is ensured that the numbers of generated electrons and holes are equal, which ensures continuity of charge throughout the device.

It is necessary to consider several different factors which affect the power conversion efficiency of any organic photovoltaic device and these are defined as

1. The photon absorption efficiency, $\eta_A = \dfrac{\text{number of absorbed photons}}{\text{number of photons incident on cell}}$
2. The exciton dissociation efficiency, $\eta_e = \dfrac{\text{number of dissociated excitons}}{\text{number of absorbed photons}}$
3. The charge transport efficiency, $\eta_c = \dfrac{\text{number of electrons in the external circuit}}{\text{number of dissociated excitons}}$
4. The internal quantum efficiency, $\eta_{IQE} = \eta_e \eta_c$
5. The external quantum efficiency, $\eta_{EQE} = \eta_A \eta_{IQE}$

The formalism of reference [55] is used here for quantifying the illumination intensity. Monochromatic illumination at 459nm is incident on the cells with a power density of $1\mathrm{Wm}^{-2}$. Therefore, 1 Sun illumination is defined as a power density of $1\mathrm{Wm}^{-2}$. The illumination intensity (in photons per unit are per unit time) is given by the power density divided by the energy of a photon at 459nm, which is equal to $2.3\times10^{18}\mathrm{m}^{-2}\mathrm{s}^{-1}$.

3.7.1 Organisation of results

In the results section below, two different sets of morphologies are of interest,

1. where the electrode length, L_{elec} is fixed and the length of the interface, L_{int} is varied by changing L_F.
2. where L_{int} is varied to the same extent as considered in (1) but L_{elec} is also varied so that the ratio $\frac{L_{int}}{L_{elec}}$ is kept constant.

The total length of the interface, L_{int}, is given by

$$L_{int} = 2N_F L_F + L_{elec}, \tag{3.58}$$

where N_F is the number of fingers (4 throughout this work). Table 3.2 gives the morphological parameters considered in this chapter for cases 1 and 2 in the above list. Firstly, for each of these two cases in turn, the relationship between morphology and η_{IQE} is studied by studying η_c and η_e.

Next, the inclusion of a full optical model to describe the incident sunlight on the solar cells is justified by comparing current-voltage characteristics obtained using the full model and an exponentially decaying illumination profile.

The variation of the key photovoltaic parameters J_{sc}, V_{oc}, η_{mpp} and FF with variations in morphology and illumination intensity are then considered for the two morphology schemes. In addition to this, scheme 1 is also considered in the absence of polaron pairs so that excitons dissociate directly into free charges. When polaron pairs are absent, the charge continuity equation (equation 3.31) is modified as,

$$\frac{\partial n(p)}{\partial t} = \frac{G_X - F_X}{h} + (-)\frac{1}{e}\nabla \cdot J_{n(p)}, \tag{3.59}$$

where all symbols are as defined previously.

Finally, the effect of the electric field on device performance is discussed with relation to field screening in the region surrounding the fingers in the device geometry. Results are presented showing that field screening can improve or degrade the V_{oc}.

3.8 Results

3.8.1 Quantum efficiency as a function of morphology

A considerable advantage of multi-dimensional modelling in the study of excitonic solar cells is that it enables the investigation of the morphological dependence of the efficiency. This is, after all, the parameter all solar cell research is ultimately intent on improving. It has been shown before by both experimental [108] and theoretical [109] research that the internal quantum efficiency does not always increase monotonically with increasing interfacial area as might be expected. Reference [109] showed that as the interfacial area is increased, the exciton dissociation efficiency increases. This is because the excitons are more likely to find an interface within an exciton diffusion length of their creation site. However, the charge transport efficiency is decreased because charges are more likely to recombine across the heterojunction. Since η_{IQE} is the product of these two quantities, it may exhibit a peak at intermediate morphologies. The device model in reference [109] is a bulk heterojunction device consisting of a 3D blend of donor and acceptor materials and considered ratios of interfacial to electrode areas roughly two orders of magnitude higher than those considered here. To elucidate the effect of morphology on the results, simulations including polaron pairs are considered for the two cases where the ratio of electrode length, L_{elec} to interface length, L_{int}, is either constant or varying.

Variable electrode to interfacial area ratio

Firstly, the fraction $\frac{L_{elec}}{L_{int}}$ is varied. Figures 3.11 and 3.12 show the charge transport and exciton dissociation efficiency for this case.

Up to biases approaching V_{oc}, the charge transport efficiency in figure 3.21 is unity because there is insufficient recombination to cancel out the photocurrent. By definition, η_c will go to zero at V_{oc} because there are no carriers delivered to the external circuit. One may expect the charge transport efficiency to decrease as the interfacial

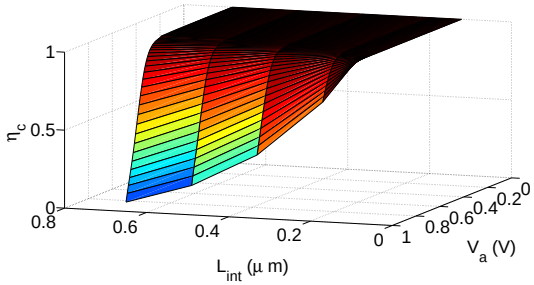

Figure 3.11: The charge transport efficiency as a function of applied bias and morphology for varying $\frac{L_{elec}}{L_{int}}$ and for 0.1 Sun. The values are normalised to the highest value found for each applied bias.

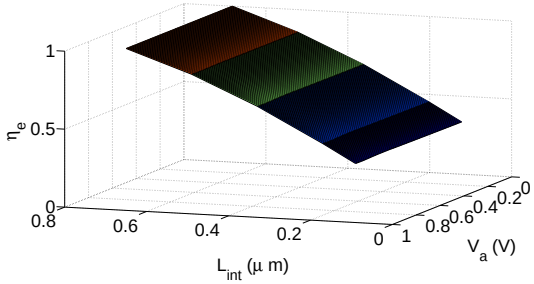

Figure 3.12: The exciton dissociation efficiency as a function of applied bias and morphology for varying $\frac{L_{elec}}{L_{int}}$ and for for 0.1 Sun. The values are normalised to the highest value found for each applied bias.

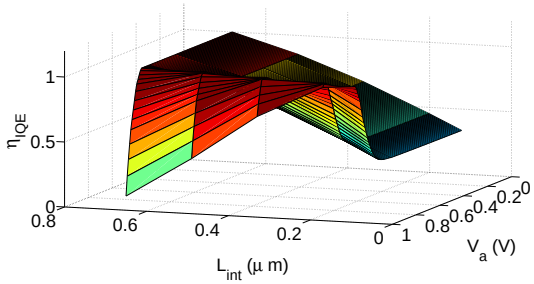

Figure 3.13: The internal quantum efficiency efficiency as a function of applied bias and morphology for varying $\frac{L_{elec}}{L_{int}}$ and for 0.1 Sun. The values are normalised to the highest value found for each applied bias.

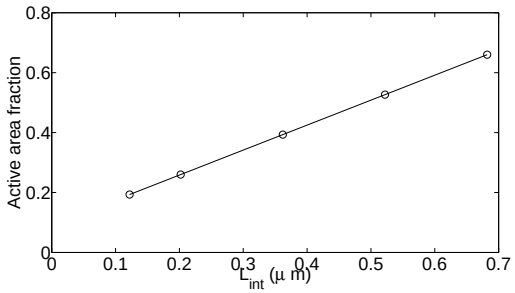

Figure 3.14: The active area fraction for varying $\frac{L_{elec}}{L_{int}}$.

area increases due to increased recombination as found in reference [109] but this is not seen except at biases close to V_{oc}.

The exciton dissociation efficiency shows a monotonic increase with increasing interfacial area in agreement with reference [109]. In order to quantify this, the active area fraction of the solar cells is defined as the ratio of the area within an exciton diffusion length (10nm) of the interface to that of the whole device. If this fraction grows as the length of the interface increases then the exciton diffusion efficiency is expected to increase also. Figure 3.14 shows that this is case.

The product of η_c and η_e gives the IQE, which is shown in figure 3.13. At low bias the shape of the internal quantum efficiency is dominated by the rise in the diffusion efficiency since η_c is unity and at high bias the rise in the diffusion efficiency is overwhelmed by the decrease in η_c. At biases between 0.77-0.88V a peak in η_{IQE} is observed, which is in agreement with the modelling studies in reference [109].

Reference [110] reports data at short circuit conditions for a similar, interdigitated

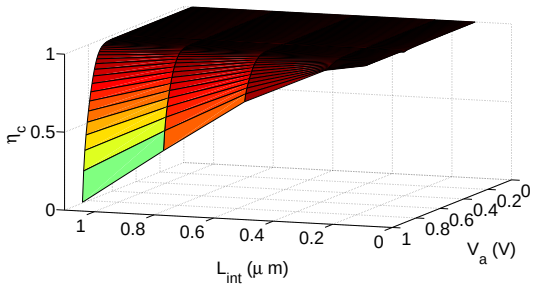

Figure 3.15: The charge transport efficiency as a function of applied bias and morphology for constant $\frac{L_{elec}}{L_{int}}$ and for 0.1 Sun. The values are normalised to the highest value found for each applied bias.

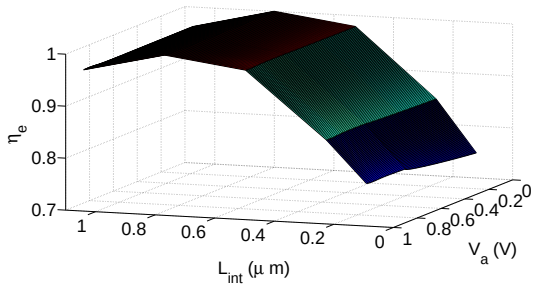

Figure 3.16: The exciton diffusion efficiency as a function of applied bias and morphology for constant $\frac{L_{elec}}{L_{int}}$ and for 0.1 Sun. The values are normalised to the highest value found for each applied bias.

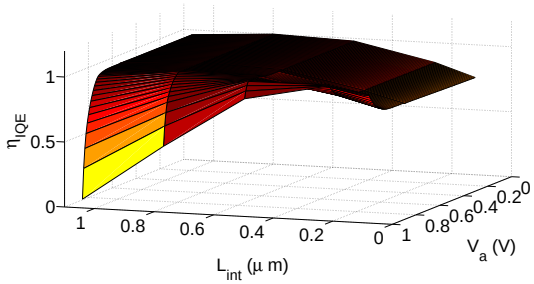

Figure 3.17: The internal quantum efficiency efficiency as a function of applied bias and morphology for constant $\frac{L_{elec}}{L_{int}}$ and for 0.1 Sun. The values are normalised to the highest value found for each applied bias.

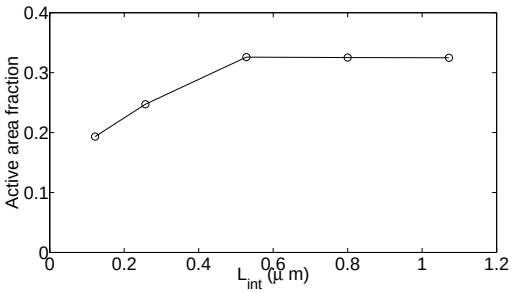

Figure 3.18: The active area fraction for constant $\frac{L_{elec}}{L_{int}}$.

morphology to that considered here and shows that as the interfacial area between the donor and acceptor becomes longer, a peak in J_{sc} is observed for most conditions considered. This is shown to be due to competition between increasing generation and increasing recombination, which grow in strength at different rates. This is entirely analogous to the results reported here where a peak in η_{IQE} is observed between 0.77-0.88V.

Constant electrode to interfacial area ratio

In the previous section, the ratio $\frac{L_{elec}}{L_{int}}$ was allowed to vary. In this section this fraction is kept constant and figures 3.15-3.17 show η_c, η_e and η_{IQE} as a function of morphology and applied bias.

From examination of figure 3.15 it is clear that all free charges escape the device without recombination except for biases very close to V_{oc} in agreement with figure

3.11. However, figure 3.16 shows that η_e exhibits a peak at intermediate interfacial area and is broadly independent of the applied bias. The value of η_e is defined as the number of dissociated excitons per absorbed photon and figure 3.18 shows that the active area fraction saturates at high values of the interface length. Therefore, the fact that η_e exhibits a peak at intermediate morphologies indicates that the number of excitons generated is not saturating also. Since η_c is unity at short circuit and the active area fraction saturates, the value of J_{sc} is also expected to saturate and this is seen in figure 3.20 on page 93.

Figure 3.17 shows the IQE and is highly dependent on the morphology and applied bias, exhibiting a maximum in the IQE at every bias considered. At high bias, the charge transport efficiency is considerably decreased and therefore the maximum in η_{IQE} is shifted towards increasingly low interfacial areas as the bias approaches V_{oc}.

3.8.2 Validity of the Lambertian illumination profile

Several organic solar cell device models use a Lambertian absorption profile where the light intensity decreases exponentially with distance inside the device [110, 33]. Figure 3.19 shows a comparison of the current-voltage characteristics of two devices, one with a Lambertian profile and one using the optical electric field obtained by solving equation 3.38. For the Lambertian case, the transmitted intensity is calculated using the reflectance at the air-glass interface, R^*, so that

$$Q = \frac{1}{2} c\epsilon_0 \alpha \eta E^2_{\hbar\omega,0} \left(1 - R^*\right) \exp\left(-\alpha x\right), \tag{3.60}$$

where Q is the parameter denoting exciton generation in equation 3.24.

Figure 3.19 shows that by using the Lambertian illumination profile (including the ITO and PEDOT layers) reduces the predicted J_{sc} by an order of magnitude and the V_{oc} by approximately 50mV. The currents decrease with increasing applied bias because the internal electric field is decreasing, which decreases polaron pair dissociation. It will be seen below that when solving for the full optical electric field profile, these reductions are commensurate with a reduction in the illumination intensity by roughly an order of magnitude. This is because the J_{sc} is proportional to the intensity (except at very high illumination levels) for each decade increase in intensity the V_{oc} increases by between 50 and 60mV. This emphasises the necessity of using a realistic illumination profile for predicting the response of organic solar cells.

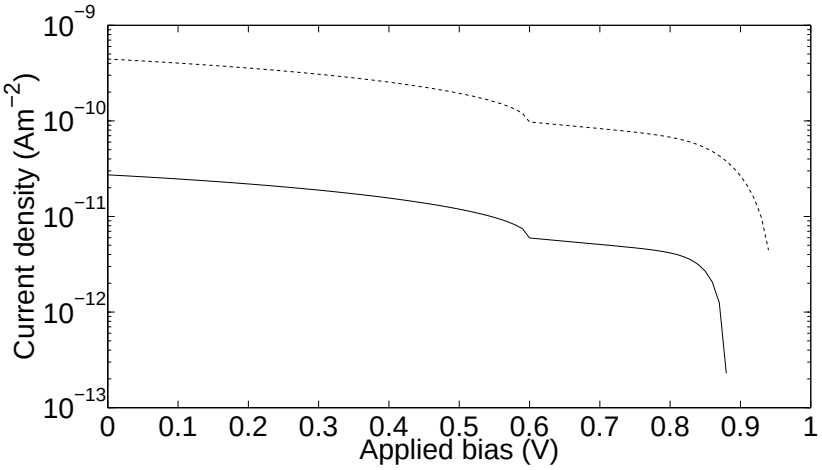

Figure 3.19: Comparison of different illumination profiles on the current-voltage characteristic for L_{elec}=105nm, L_F=19nm including polaron pairs at 0.1 Sun. The Solid line uses the Lambertian profile in equation 3.60 and the dashed line uses the optical electric field obtained by solving equation 3.38.

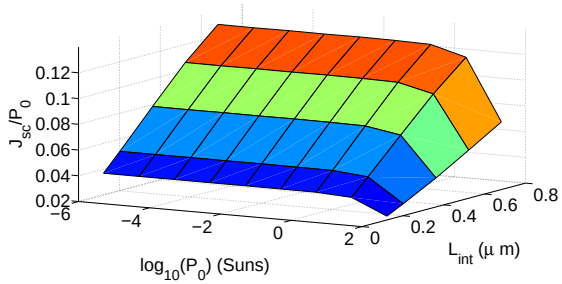

Figure 3.20: Short circuit current density normalised to the illumination intensity for constant L_{elec} and with polaron pairs.

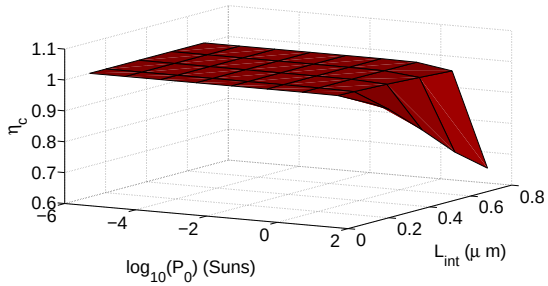

Figure 3.21: Charge transport efficiency at short circuit for constant L_{elec} and with polaron pairs.

3.8.3 Key photovoltaic parameters: Varying L_{int}, constant L_{elec}, polaron pairs included

Short circuit current

Figure 3.20 shows the short circuit current density as a function of intensity and morphology for the constant L_{elec} and varying L_{int}. The J_{sc} has been normalised to the illumination power density (that is $\frac{J_{sc}}{P_0}$) because it is expected to increase linearly with P_0 [2]. In this work, the illumination intensity is varied over 8 orders of magnitude and so providing the quantity $\frac{J_{sc}}{P_0}$ enables the results to be analysed more easily.

Figure 3.20 shows that the J_{sc} increases as the contact area between the two phases increases. This is because the active area ratio of the device is increasing, as seen previ-

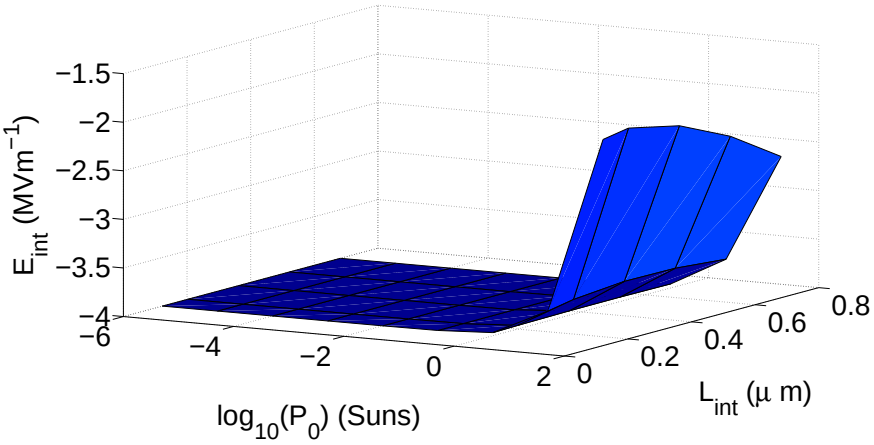

Figure 3.22: The average short circuit electric field at the interface for constant L_{elec} and with polaron pairs.

ously in figure 3.14. Therefore, more excitons are able to diffuse to the heterojunction and dissociate into free charges. These free charges then move to the electrodes where they are extracted and establish a photocurrent.

Two effects will principally affect the short circuit current,

1. Free charge recombination, reflected in the charge transport efficiency η_c, figure 3.21.
2. The effect of the electric field on the polaron pair dissociation, which will ultimately determine how many photogenerated excitons can contribute to the photocurrent, figure 3.22.

Figure 3.21 shows that η_c decreases at high intensity. This will act to decrease the short circuit current as observed in figure 3.20. The average electric field at the interface between the polymer phases is shown in figure 3.22. The electric field increases (becomes less negative) at high intensity. This will act to decrease the polaron pair dissociation rate further and will decrease the short circuit current as has been previously reported in reference [55].

Maximum power point efficiency

The power conversion efficiency at the maximum power point is given by the equation,

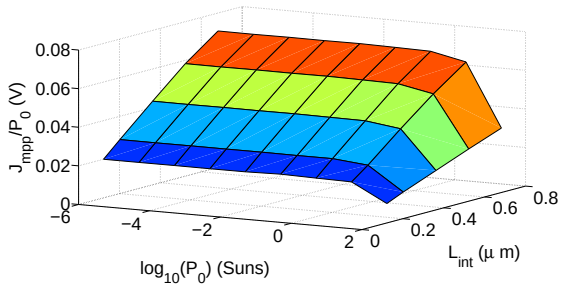

Figure 3.23: Maximum power point current density normalised to the illumination intensity for constant L_{elec} and with polaron pairs.

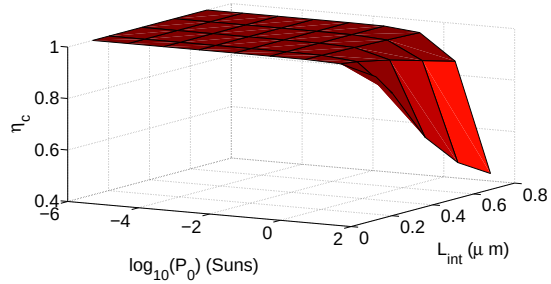

Figure 3.24: Charge transport efficiency at the maximum power point for constant L_{elec} and with polaron pairs.

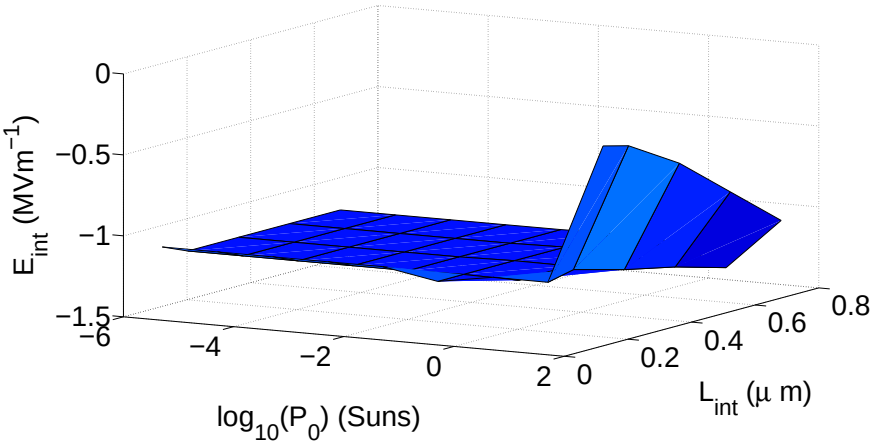

Figure 3.25: The electric field at the interface between the polymer phases at maximum power point for constant L_{elec} and with polaron pairs.

$$\eta_{mpp} = \frac{J_{mpp}}{P_0} \times V_{ampp}. \tag{3.61}$$

It is therefore of interest to study the two quantities $\frac{J_{mpp}}{P_0}$ and V_{ampp}. Figures 3.23-3.26 show the current, the charge transport efficiency η_c, the average interfacial electric field and the applied bias at the maximum power point voltage respectively.

Figure 3.23 shows that the current density increases as the length of the fingers increases and also decreases for increasing illumination intensity. This is precisely the same behaviour as noted above for J_{sc} and the increase in J_{mpp} is due to the increasing active area fraction seen in figure 3.14. As for the short circuit current considered in figure 3.20, the decrease in J_{mpp} for intense illumination can be seen to be due to the combined factors of the decreased charge transport efficiency, figure 3.24, and the electric field, figure 3.25, which acts to decrease polaron pair dissociation.

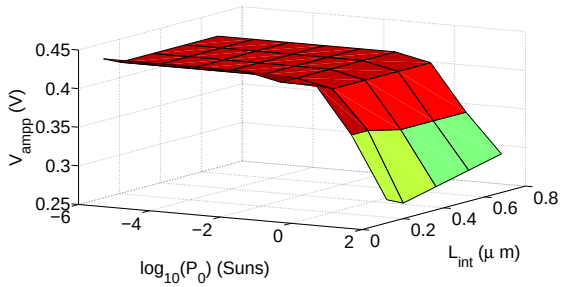

Figure 3.26: The maximum power point voltage for constant L_{elec} and with polaron pairs.

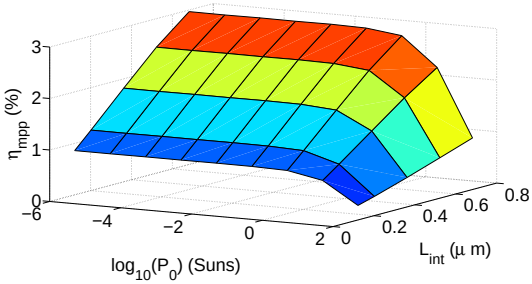

Figure 3.27: The maximum power point efficiency for constant L_{elec} and with polaron pairs.

The applied bias at the maximum power point, V_{ampp}, is constant up to ∼1 Sun and decreases for higher intensities. From figure 3.19, it is clear that the current decreases with increasing applied bias in this case. The power is given by the product of the current and the applied voltage, therefore, if the maximum power point voltage is constant at low to intermediate intensity, this means that the associated currents are all decreasing at the same rate with respect to the applied bias. The currents decrease with increasing applied bias because the internal electric field is decreasing and hence polaron pair dissociation is inhibited. The decrease in V_{ampp} at high intensity will be due partly to the decrease in the charge transport efficiency at high intensity, figure 3.24, meaning that the injected current will be able to cancel out the photogenerated current at lower applied biases. The decrease in the polaron pair dissociation efficiency, figure 3.25, will have the same effect.

If the electric field in the devices was constant across the devices, it would take the value

$$E = \frac{V_a - V_{bi}}{d}. \tag{3.62}$$

Therefore, if V_{ampp} is decreasing (as is observed at high intensity in figure 3.25), the interfacial electric field would be expected to become more negative. This is in opposition to what is seen in figure 3.25 and the observed decrease in magnitude of the electric field must therefore be solely due to the build up of space charge.

The maximum power point efficiency is shown in figure 3.27. From the previous consideration of the current and the maximum power point voltage, it can be immediately seen that the increase in efficiency with increasing L_{int} is due to the increase of the current, figure 3.23. Also, it can also be seen that the decrease at high intensity is due to the combined effects of the decreased maximum power point voltage, figure 3.26 and the decrease in current, figure 3.23.

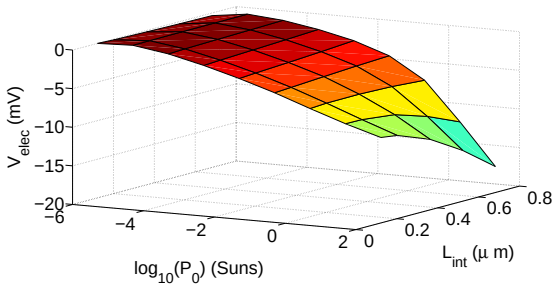

Figure 3.28: V_{elec} relative to that calculated for the lowest intensity and interfacial area considered for constant L_{elec} and with polaron pairs.

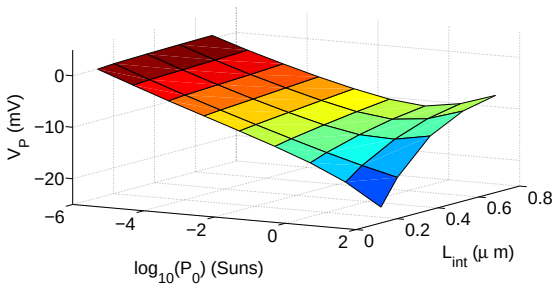

Figure 3.29: V_P relative to that calculated for the lowest intensity and interfacial area considered for constant L_{elec} and with polaron pairs.

Open circuit voltage

The open circuit voltage is examined in terms of its constituent components as set out in equations 3.54 and 3.56. It has been found that that the different terms in equation 3.56 can differ significantly from one another in magnitude. Therefore they are plotted with respect to the value for the smallest value of L_{int} and illumination intensity considered. This gives a feel for the trends involved as the morphology and optical bias are varied, which is the behaviour of interest.

Figure 3.28 shows the evolution of V_{elec} and it is clear that this term acts to decrease the open circuit voltage and is therefore detrimental to device performance. The fact that this term is increasing in magnitude means that the densities of majority carriers at their respective electrodes are increasing, acting to reduce the quasi-Fermi level splitting between the polymer-polymer interface and the electrodes. This behaviour has been noted previously for a bilayer device [55] and effect becomes more pronounced for higher illumination intensities and for increased interfacial area.

Figure 3.29 shows V_P for the same system and again it is seen that V_P tends to reduce the V_{oc} and shows a general increase in magnitude with increasing intensity. In contrast to V_{elec}, V_P tends to decrease faster for lower interfacial areas. These effects will tend to cancel each other out in the final value of V_{oc}. In these simulations P is between 4% and 8% and V_P will only give a positive contribution if $P > \frac{1}{2}$.

The behaviour of V_{G_X} is considered in figure 3.30. This figure has been displayed in two parts since the size of the term obscures the change with morphology. The change in V_{G_X} as the intensity is increased is significantly more pronounced than V_{elec} and V_P and is also significantly more uniform as the morphology is varied. For every morphology and intensity considered, the rise in V_{oc} with each decade of intensity is 59.5mV. The uniformity with increasing illumination intensity implies that it is solely

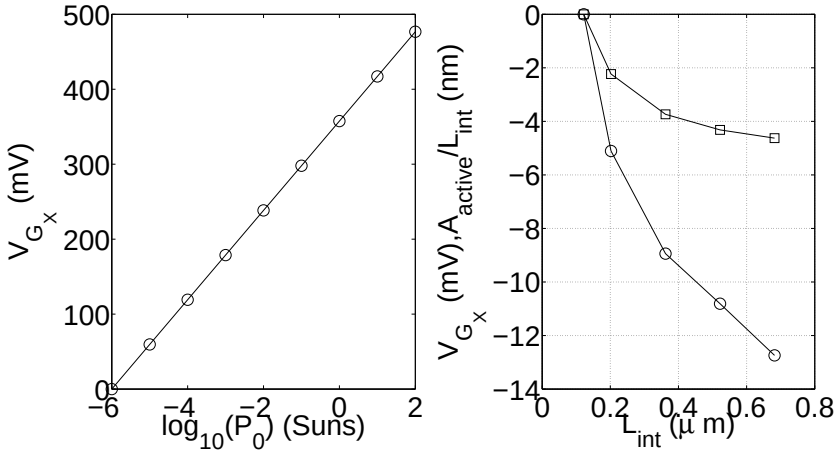

Figure 3.30: V_{G_X} relative to that calculated for the lowest intensity and interfacial area considered for constant L_{elec} and with polaron pairs. The right hand side of the figure shows the behaviour as the morphology changes for 10^{-6} Sun illumination (◯) and the ratio of the active area to L_{int} relative to the shortest value of L_{int} in table 3.2 (□). This observed decrease in V_{G_X} in the right hand pane is seen uniformly for all intensities considered and is obscured by the large increase as the intensity is increased (left hand pane).

the morphology of the system which affects this term and this is borne out by the fact that the change in V_{G_X} with morphology is unchanged when vastly different light powers are incident. As the interfacial area between the polymer phases increases, V_{G_X} decreases by up to approximately 13mV. This means that fewer excitons are being dissociated per unit interfacial area.

The quantity, V_{G_X} is a measure of the total number of dissociated excitons per unit interfacial area. Therefore, the behaviour of V_{G_X} in the right panel of figure 3.30 should reflect the ratio of the active area to total length of the interface, L_{int}. This behaviour is evident in the right hand pane of figure 3.30 and shows that L_{int} is increasing at a faster rate that the active area.

The three terms V_P, V_{elec} and V_{G_X} are all plotted for L_{elec}=50nm and L_{int}=362nm in figure 3.31. The very large increase in V_{G_X} compared to the other terms means that plotting all three on the same axes would obscure the relative magnitudes of the changes in V_P and V_{elec}. From figure 3.31 it is clear that the behaviour of V_{oc} as the intensity is increased is dominated by V_{G_X}.

Equation 3.54 begins to break down at high interfacial areas and illumination intensities. The discrepancy between the equation and the simulation results originates from the fact that in each interface subdomain, the average of the electron and hole densities and the electric field are used, equation 3.57. At high interfacial areas and illumination

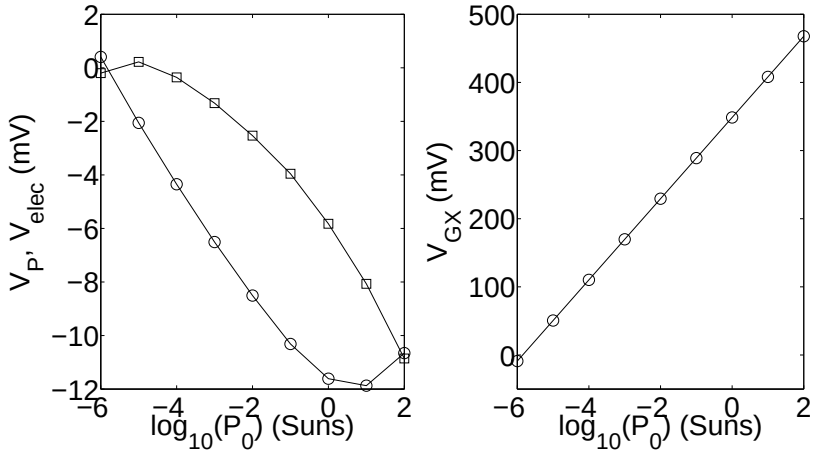

Figure 3.31: The left hand panel shows V_P (◯) and V_{elec} (□) and the right hand panel shows V_{G_X}. All quantities are for L_{elec}=50nm and L_{int}=362nm and are with respect to their values at the shortest finger length and lowest intensity considered.

intensities, these quantities vary rapidly at the interface and therefore the product of the averages are not rigorously equal to the local values. However, for the shorter values of L_{int} considered here, the agreement between the simulations and the equation is excellent as shown in figure 3.32.

Fill factor

The fill factor, FF, is defined in equation 1.3 and the form of the second equality will be used here because the behaviour of each of the quantities in this definition have already been considered. Figure 3.33 shows the FF as a function of L_{int} and P_0.

Figure 3.33 shows that the FF decreases at a constant rate for all intensities up to 1 Sun and then decreases more rapidly. Figures 3.27 and 3.20 show that η_{mpp} and $\frac{J_{sc}}{P_0}$ are roughly constant up to this intensity and so this initial decrease in FF can be attributed to the logarithmically increasing V_{oc}. Above 1 Sun, the decrease in the FF is accelerated. The open circuit voltage continues to rise logarithmically, so the further decrease in FF is due to the decrease in η_{mpp}. This is because the decrease in $\frac{J_{sc}}{P_0}$ will act to increase the FF, contrary to what is observed in figure 3.33.

3.8.4 Key photovoltaic parameters: Varying L_{int}, constant L_{elec}, polaron pairs not included

Simulations are now considered without the presence of polaron pairs.

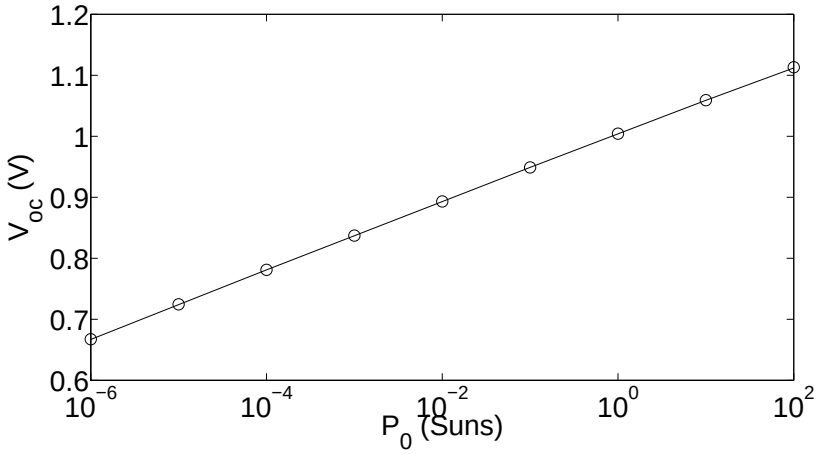

Figure 3.32: Comparison of simulated V_{oc} as a function of illumination intensity (◯) and calculated from equation 3.54 (solid line) for constant L_{elec} and with polaron pairs for L_{elec}=50nm and L_{int}=122nm.

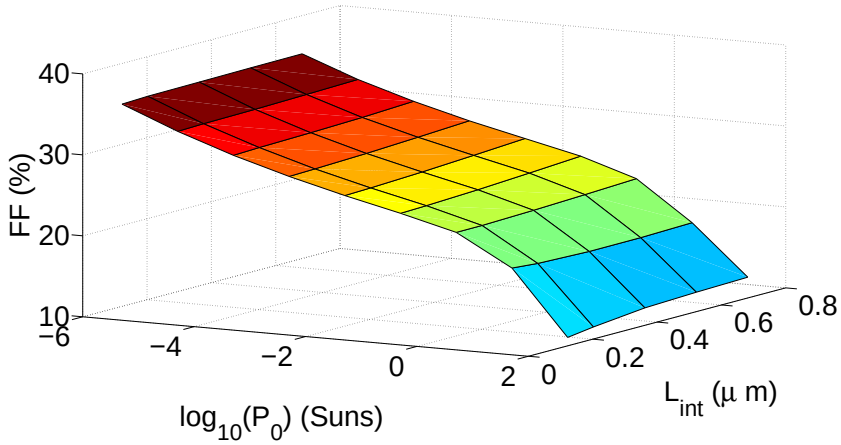

Figure 3.33: The fill factor for constant L_{elec} and with polaron pairs.

Short circuit current

Figure 3.34 shows that the decay of polaron pairs at the interface provides a significant loss mechanism at short circuit because the currents are roughly a factor of two larger in figure 3.34 compared to those in figure 3.20 when polaron pairs are present. Additionally, J_{sc} is seen to grow with increasing L_{int} due to the increasing active area fraction in figure 3.14. The charge transport efficiency at short circuit is shown in figure 3.35 and the decrease at high intensity is in agreement with figure 3.21. In this case the decrease in J_{sc} at high intensity can be solely attributed to this decrease in charge transport efficiency because the polaron pairs are absent and hence the interfacial electric field does not affect free charge generation.

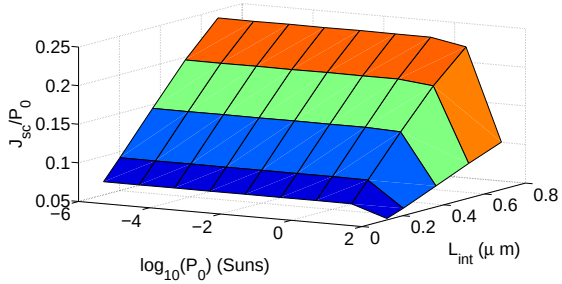

Figure 3.34: Short circuit current density normalised to the illumination intensity for constant L_{elec} and without polaron pairs.

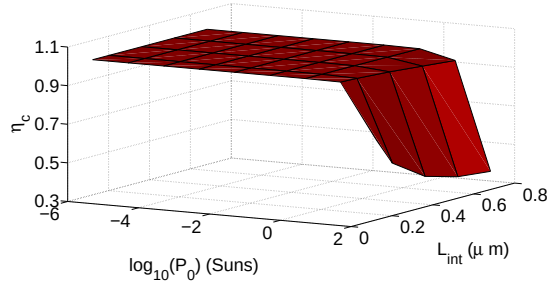

Figure 3.35: Charge transport efficiency at short circuit for constant L_{elec} and without polaron pairs.

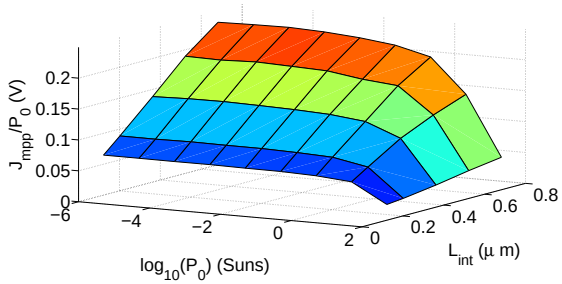

Figure 3.36: Maximum power point current density normalised to the illumination intensity for constant L_{elec} and without polaron pairs.

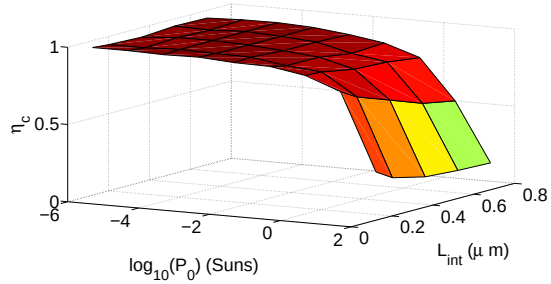

Figure 3.37: Charge transport efficiency at the maximum power point for constant L_{elec} and without polaron pairs.

Figure 3.35 shows that the decrease in η_c is greater at high values of L_{int} and illumination intensities compared to the case when polaron pairs are present, figure 3.21. This is attributed to the fact that in the absence of polaron pairs, all of the free charges which recombine will be lost. However, in figure 3.21, the polaron pairs can re-dissociate back into free charges, increasing η_c.

Maximum power point efficiency

Figures 3.36-3.38 show the current, charge transport efficiency and the applied bias at the maximum power point. Figure 3.36 shows that the current increases with increasing L_{int} due to the increasing active area fraction. The decrease at high intensity is again attributed solely to the reduced charge transport efficiency, figure 3.37, due to the absence of polaron pairs in the simulations.

The shape of the maximum power point voltage results in figure 3.38 is rather different from that seen above in the presence of polaron pairs, figure 3.26. The latter shows a constant value up to high illumination intensity as opposed to the peak at $\sim 10^{-3}$ Suns in figure 3.38. This differing behaviour can be attributed to the effect of the electric

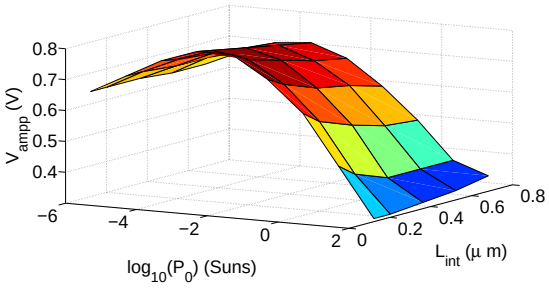

Figure 3.38: The maximum power point voltage for constant L_{elec} and without polaron pairs.

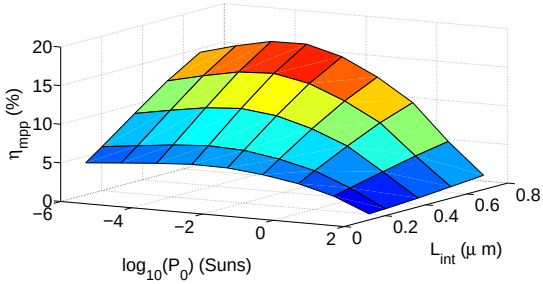

Figure 3.39: The maximum power point efficiency for constant L_{elec} and without polaron pairs.

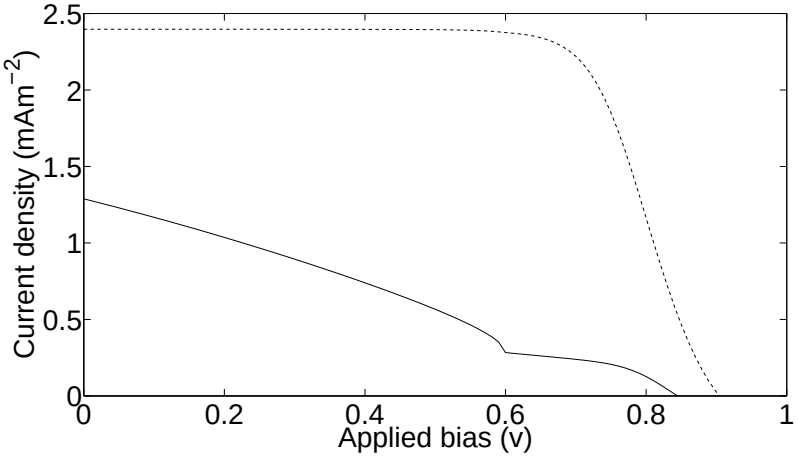

Figure 3.40: Current-voltage characteristics for constant L_{elec} with polaron pairs (solid line) and without polaron pairs (dashed line) for L_{int}=682nm, L_{elec}=50nm and 0.01 Sun.

field on the polaron pair dissociation. Figure 3.40 compares the shapes of the current-voltage characteristics in the presence and absence of polaron pairs. Since the polaron pair dissociation rate, and hence the current, is dependent on the electric field, the resultant current will decrease with increasing applied bias because the internal field is decreasing. In addition, for biases above V_{bi}, there will be a significant amount of charge injected into the device, which will act to increase recombination and decrease the current further [55]. In the absence of polaron pairs, the current only starts to decrease for $V_a \approx V_{bi}$ because the photocurrent is electric field independent as is clear from figure 3.40. The initial rise in the maximum power point voltage in the absence of polaron pairs, figure 3.38, is therefore due to the increasingly large bias needed for the injected current to overwhelm the increasing photocurrent. The subsequent decrease in V_{ampp} will be due to the decrease in charge transport efficiency, meaning that less photogenerated charges reach the electrode, and so a smaller applied bias is required to cancel out the photocurrent.

Figure 3.39 shows η_{mpp} in the absence of polaron pairs. It is immediately apparent that the peak in η_{mpp} is due to the peak in V_{ampp} and that the decrease at high intensities is due to the combined effects of the decreased maximum power point voltage, figure 3.38, and the decreased current, figure 3.36.

Open circuit voltage

It is unnecessary here to include the V_P term since excitons are dissociated directly into free charges. The term V_{G_X} is again found to be remarkably consistent in its behaviour when the intensity and morphology are changed with the increase of V_{G_X} lying between 59 and 60mV per decade of intensity and again decreasing with increasing L_{int}. It is interesting to examine the difference in the value of the open circuit voltage depending on whether or not polaron pairs are included. It would certainly be expected that in this latter case, higher open circuit voltages would result since in the case where polaron pairs are present, some dissociated excitons will never give rise to free charges. This is precisely what is observed and the difference between the open circuit voltages can be entirely attributed to the voltage loss due to the decay of polaron pairs, V_P. With V_P varying between 60 and 85mV, this is a significant loss channel in organic solar cells.

Fill factor

The situation is more complicated in the absence of polaron pairs because the shape of the η_{mpp} curve exhibits a peak at intermediate intensity, figure 3.41. However, the peak in the FF is less pronounced and is shifted to lower values of the illumination intensity due to the increasing open circuit voltage. Since $\frac{J_{sc}}{P_0}$ is constant up to 1 Sun, figure 3.34, the decrease in FF at low intensity is therefore due to the increasing V_{oc}. Also, as noted above, the decreasing value of $\frac{J_{sc}}{P_0}$ at high intensity will only act to increase the FF. Above 10^{-3} Suns, the decrease in η_{mpp} will also aid the decrease in the FF. In figures 3.38, 3.39 and 3.41, V_{ampp}, η_{mpp} and FF are significantly higher than found in figures 3.26 3.27 and 3.33. This can be attributed to the more rectangular current-voltage curve in figure 3.40, where the current decreases with increasing forward bias even near short circuit where polaron pairs are present. These higher values of the FF and η_{mpp} give further indication of the significant loss mechanism brought about by the presence of polaron pairs in organic solar cells.

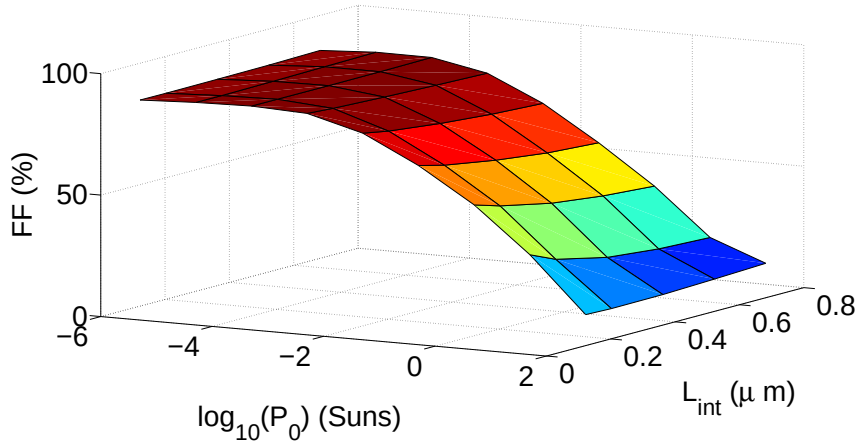

Figure 3.41: The fill factor for constant L_{elec} and without polaron pairs.

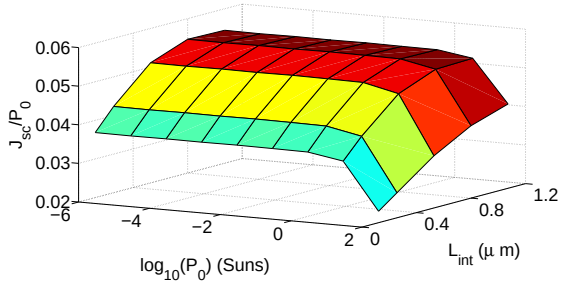

Figure 3.42: Short circuit current density normalised to the illumination intensity for varying L_{elec} and with polaron pairs.

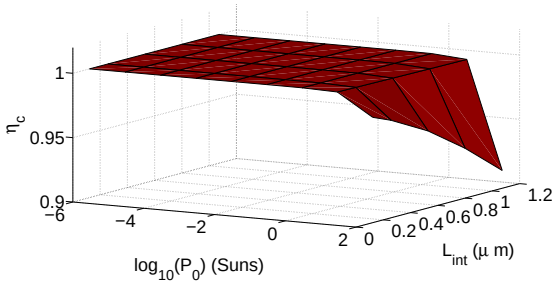

Figure 3.43: The charge transport efficiency at short circuit for varying L_{elec} and with polaron pairs.

3.8.5 Key photovoltaic parameters: Varying L_{int} and L_{elec}, polaron pairs included

Short circuit current

Now the effect of the ratio between L_{int} and L_{elec} on the J_{sc} is considered in figures 3.42-3.44. As well as the decrease in the current at high illumination intensity in agreement with figure 3.20 and 3.34, it is clear that the current saturates at high values of the interfacial area.

Figure 3.18 shows that the active area fraction in this geometry saturates as L_{int} increases. The length of the electrode, L_{elec} is increasing at the same rate as the total volume of the device and therefore the current density is expected to saturate also, which is observed in figure 3.42.

When L_{elec} is held constant and polaron pairs are included, the charge transport ef-

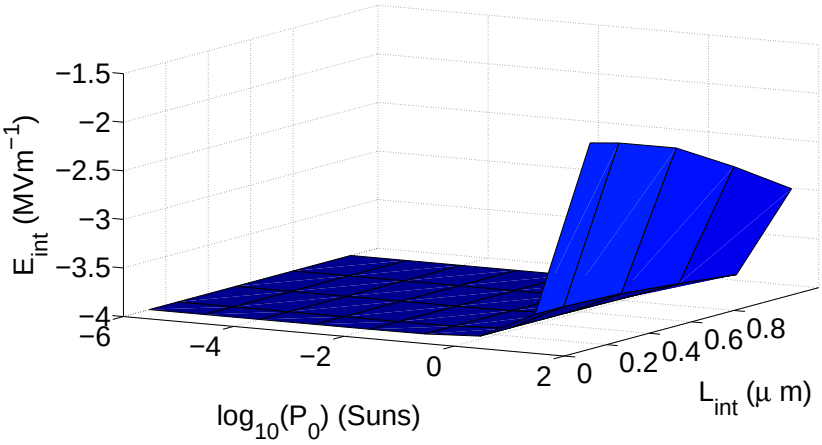

Figure 3.44: The electric field at the interface at short circuit for varying L_{elec} and with polaron pairs.

ficiency figure 3.21 at high intensity is significantly lower than in the equivalent case where L_{elec} varies, figure 3.43. This is attributed to the fact that in the former case there is more interfacial area per cross sectional area of the device and therefore more chance for recombination of free carriers at the junction. The decrease in charge transport efficiency at high intensity, figure 3.43, is in agreement with the constant L_{elec} case given above in figure 3.21, acting to decrease the J_{sc} at high intensity. Figure 3.44 shows the electric field at the interface at short circuit and shows that it becomes less negative at high intensity. This is in agreement with figure 3.22 for constant L_{elec} and will act to reduce the J_{sc} further.

Modelling studies using similar morphologies, references [111, 112], have shown that the value of J_{sc} is shown to decrease as the width of the fingers is increased for constant finger length. This is in opposition to figure 3.42, which shows a saturation of J_{sc} with increasing finger width. This difference can be rationalised by noting that in references [111] and [112], the active area fraction will be decreasing as the finger width increases and therefore less excitons are able to reach to the heterojunction before decaying. In the results presented here, the active area fraction, figure 3.18 saturates for wider fingers and so J_{sc} saturates also. Reference [112] also shows that as the finger *length* is increased for constant finger width, the current increases and tends to saturate, in agreement with figure 3.42.

The results presented here and in references [109, 112, 111] show how sensitive the value of J_{sc} is to the underlying device morphology. Indeed, increasing the width of characteristic features of the device geometry can actually be detrimental to device performance even though there will be more sites for exciton dissociation. This work has shown that a crucial parameter controlling the efficacy of photon-to-current light

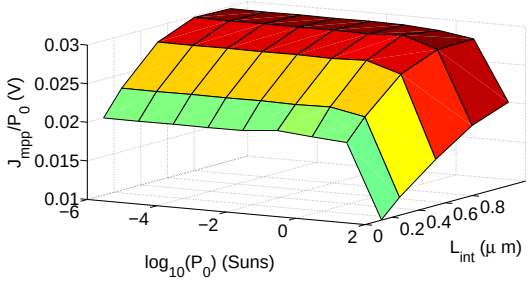

Figure 3.45: Maximum power point current density normalised to the illumination intensity for varying L_{elec} and with polaron pairs.

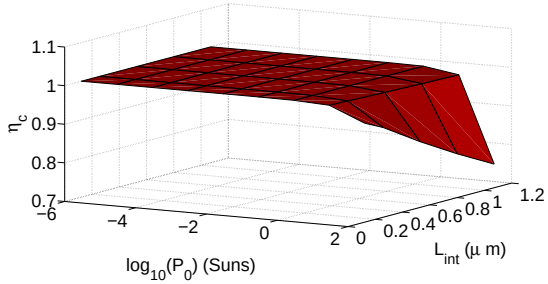

Figure 3.46: Charge transport efficiency at the maximum power point for varying L_{elec} and with polaron pairs.

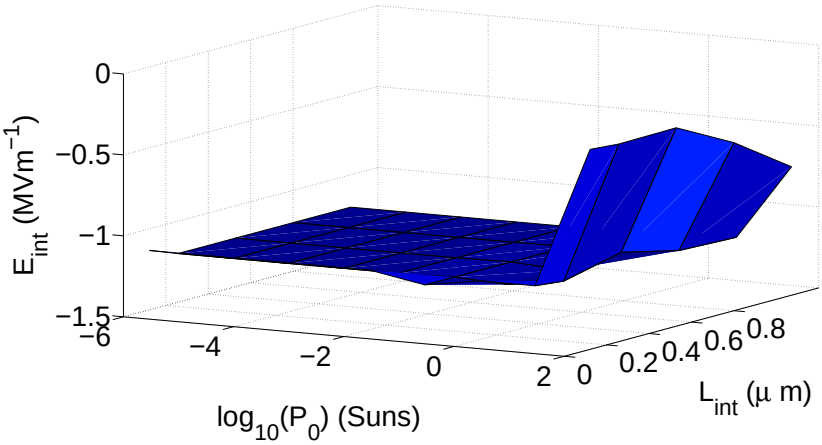

Figure 3.47: The electric field at the interface between the polymer phases at maximum power point for varying L_{elec} and with polaron pairs.

conversion is the active area fraction, as indicated by the different shapes of figures 3.14 and 3.18.

Maximum power point efficiency

Figures 3.45-3.48 show the quantities of interest for the calculation of the maximum power point efficiency.

Firstly examining figure 3.45, it is clear that a saturation occurs for increasing interfacial area and the current decreases at high intensity. The saturation of the current with increasing finger length is expected in the light of the previous discussion concerning the J_{sc} in figure 3.42. Next, the charge transport efficiency at maximum power point is shown in figure 3.46. As shown previously, there is a sharp decrease at high intensity, which will act to decrease the current, as seen in figure 3.45. It should be noted here

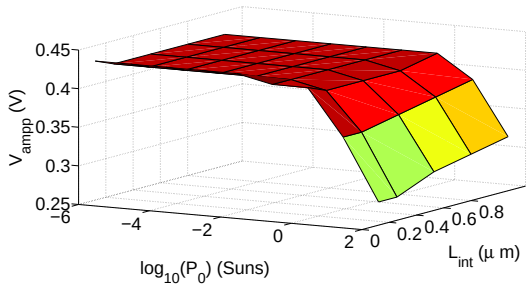

Figure 3.48: The maximum power point voltage for varying L_{elec} and with polaron pairs.

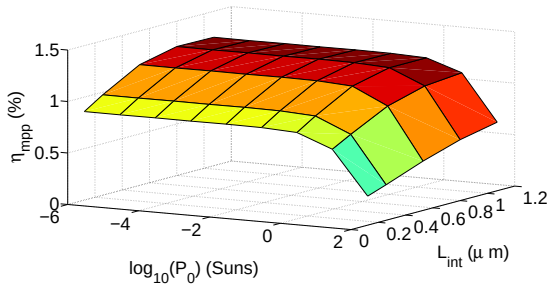

Figure 3.49: The maximum power point efficiency for varying L_{elec} and with polaron pairs.

that the fall in the charge transport efficiency in figure 3.46 is substantially less than for figure 3.24 at high intensity. This effect has been seen above for the charge transport efficiency at short circuit and was attributed to the relatively larger area of the interface compared to the heterojunction, thus providing more pathways for recombination.

Additionally, the electric field at the interface acts to decrease polaron pair dissociation at high intensity, figure 3.47, and this will also act to decrease the current in agreement with the simulations presented above. The value of V_{ampp} is shown in figure 3.48 and is found to be very similar to that found when the L_{elec} is kept constant, figure 3.26. The same conclusions can therefore be reached for the shape of this curve from examination of the decreasing polaron pair dissociation and charge transport efficiency at high intensity on page 85.

Figure 3.49 shows the maximum power point efficiency. The saturation is expected because the value of J_{mpp} saturates similarly and the V_{ampp} is constant at low to intermediate intensities, figure 3.48. The decrease in η_{mpp} at high intensity can then be attributed to the decreased current, figure 3.45, and the reduced maximum power point voltage, figure 3.48, in agreement with the simulations with constant L_{elec}, figures 3.27 and 3.39.

Open circuit voltage

Figure 3.50 shows V_{elec} for the case of varying L_{elec}, including polaron pairs with reference to that for the lowest area and intensity. The same trend is seen as for figure 3.28 and the magnitude is also very similar. The majority carriers build up at the electrodes causing V_{elec} to be detrimental to device performance, which becomes more pronounced for higher values of L_{int}.

Figure 3.51 shows V_P and again the magnitude of the decrease of V_P is very similar

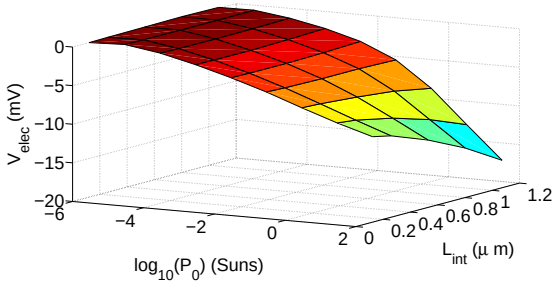

Figure 3.50: V_{elec} relative to that calculated for the lowest intensity and interfacial area considered for varying L_{elec} and with polaron pairs.

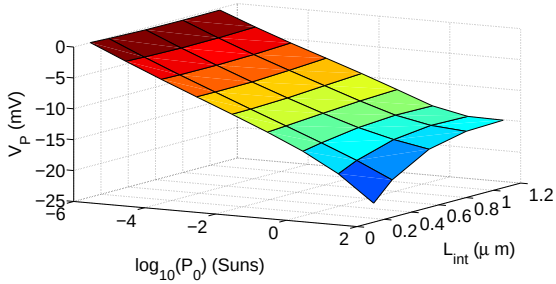

Figure 3.51: V_P relative to that calculated for the lowest intensity and interfacial area considered for varying L_{elec} and with polaron pairs.

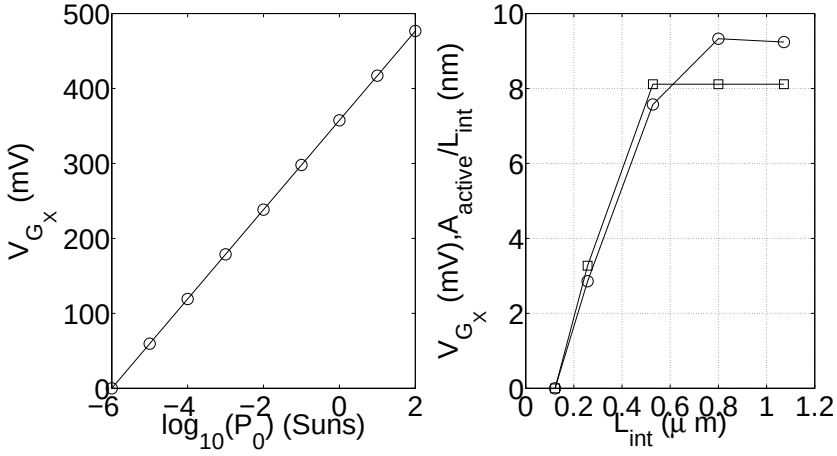

Figure 3.52: V_{G_X} relative to that calculated for the lowest intensity and interfacial area considered for varying L_{elec} and with polaron pairs. The right hand side of the figure shows the behaviour as the morphology changes for 10^{-6} Sun illumination (◯) and the ratio of the active area to L_{int} relative to the shortest value of L_{int} in table 3.2 (□). This observed increase in V_{G_X} in the right hand pane is seen uniformly for all intensities considered and is obscured by the large increase as the intensity is increased (left hand pane).

to that found before for constant L_{elec}, figure 3.29. The trend with morphology is the same also, with the decrease becoming greater for smaller interfacial areas.

Figure 3.52 shows V_{G_X}, plotted in two parts as in figure figure 3.30. Figure 3.52 has a rather different form to that for constant electrode length, figure 3.30, saturating at high values of L_{int}. Again the behaviour of this term with changing morphology is independent of intensity. The right hand panel of Figure 3.52 shows the ratio of the active area to the interface length, relative to that for the smallest value of L_{int} considered. As with figure 3.30 the behaviour of V_{G_X} tracks this quantity, as expected.

As with figure 3.31, V_P, V_{elec} and V_{G_X} are plotted for the intermediate finger length of 38nm in figure 3.53. Again, it is clear that the behaviour of V_{oc} as the intensity is

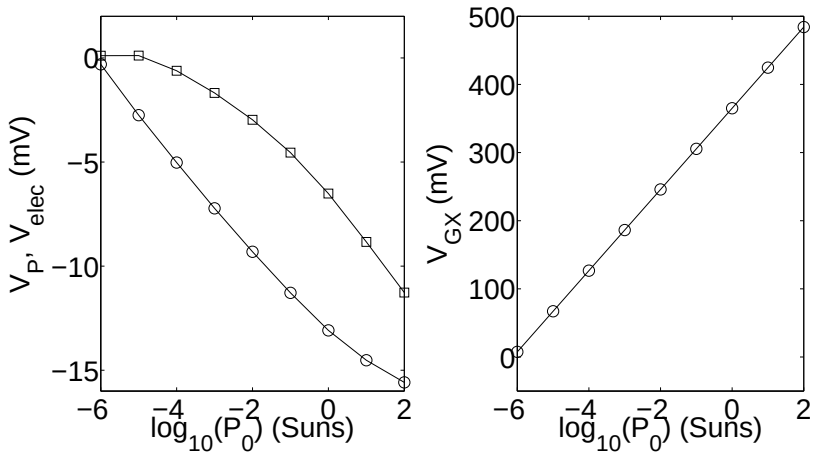

Figure 3.53: The left hand panel shows V_P (◯) and V_{elec} (□) and the right hand panel shows V_{G_X}. All quantities are for L_{elec}=216nm and L_{int}=528nm, and are with respect to their values at the shortest finger length and lowest intensity considered.

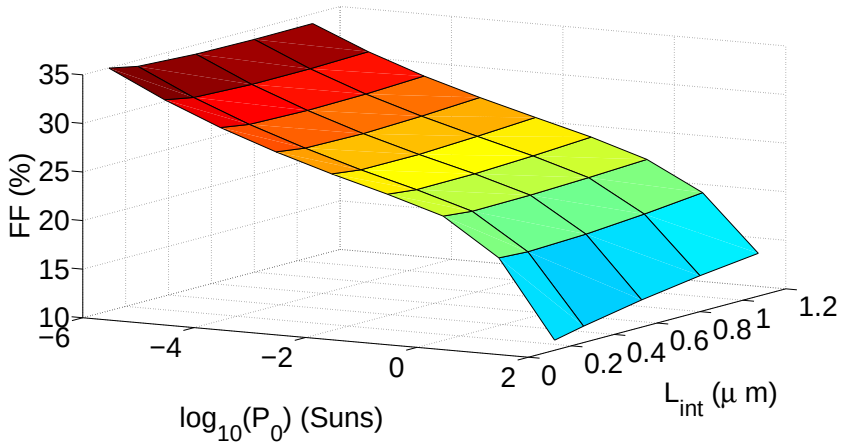

Figure 3.54: FF for varying L_{elec} and with polaron pairs.

increased is dominated by V_{G_X}.

Fill factor

The behaviour with changing morphology and intensity, as well as the magnitude of the FF for this case, figure 3.54, is very similar to that of constant electrode length, figure 3.33. The slower decrease at low to medium intensity is due to the logarithmically increasing V_{oc} when J_{sc} is proportional to the intensity, figure 3.42, and η_{mpp} is constant, figure 3.49 and equation 1.3. Then at high intensity, the faster decrease in FF is due to the additionally decreasing η_{mpp}, which in turn is because of the decreased maximum power point current and the decrease in the maximum power point voltage.

$L_{elec}(1)$(nm)	$L_F(1)$(nm)	$L_{int}(1)$(nm)	$\frac{L_{int}(1)}{L_{elec}(1)}$	$L_{elec}(2)$ (nm)	$L_F(2)$ (nm)	$L_{int}(2)$(nm)	$\frac{L_{int}(2)}{L_{elec}(2)}$
50	9	122	2.44	50	9	122	2.44
50	19	202	4.04	105	19	257	2.44
50	39	362	7.24	216	39	528	2.44
50	59	522	10.44	328	59	800	2.44
50	79	682	13.64	440	79	1072	2.44

Table 3.2: Morphology parameters for the two simulation schemes.

3.8.6 Electric field screening and its effect on the open circuit voltage

The results presented above have shown that the electric field at the polymer-polymer heterojunction has been shown to have a significant effect on the device performance. However, the complex morphology of these devices can also have a significant effect on the distribution of the electric field. In reference [55], a bilayer photovoltaic device is considered and since there is no charge transport across the heterojunction, majority holes are confined to the left of the interface and majority electrons to the right (as is considered here). Since minority carrier densities are negligible in the bilayer case [55], the electric field will have a positive gradient on the left hand side and a negative gradient on the right hand side of the junction. The electric field will therefore *always* exhibit a maximum at the interface. For the interdigitated case, the morphology is more complicated and the previous analysis will not hold since large carrier densities can now overlap by interpenetration via adjacent fingers in the morphology.

Figure 3.55 shows charge density and electric field plots for L_{int}=1072nm and L_{elec}=440nm. The electric field plotted here is the x component, where x is perpendicular to the electrodes. This is so because the polaron pair dissociation rate depends on this quantity [55] and not on E_y. At short circuit, the charge densities are low and the electric field is approximately equal to that given by the built-in voltage divided by the thickness, i.e., approximately 4MVm^{-1}. At $V_a = V_{bi}$, the charge density is similar in magnitude to that at short circuit and the field is approximately zero. However when $V_a - V_{bi} = 0.3\text{V}$, there is a significant increase in the charge density which will be due to charges injected from the electrodes above the built-in bias [55]. In the interface region for figures 3.55(vi), where the charge densities are highest, the electric field is seen to be heavily screened. In addition, neighbouring fingers contain oppositely charged carriers and the electric field may therefore be expected to vary rapidly in the y-direction. This behaviour is absent from figure 3.55 and can be explained by the fact that the form of the Poisson equation in 2 dimensions has the form,

$$-\nabla^2\psi = \frac{\partial E_x}{\partial x} + \frac{\partial E_y}{\partial y} = \frac{e(p-n)}{\epsilon_0\epsilon_r}. \tag{3.63}$$

Therefore, the rapid change in sign of the source term in the y direction can be expressed by a change in $\frac{\partial E_x}{\partial x}$ or $\frac{\partial E_y}{\partial y}$ or a combination of the two. This can be seen from examination of the y component of the electric field for the same data. Figure 3.56 shows the x and y components of the electric field for the conditions in figure 3.55(vi) and shows that the y component of the field is varying rapidly from finger to finger. The change in sign of the source term is mostly taken up in the y component of the field and E_x does not vary significantly in the y direction because of the additional 0.3V applied

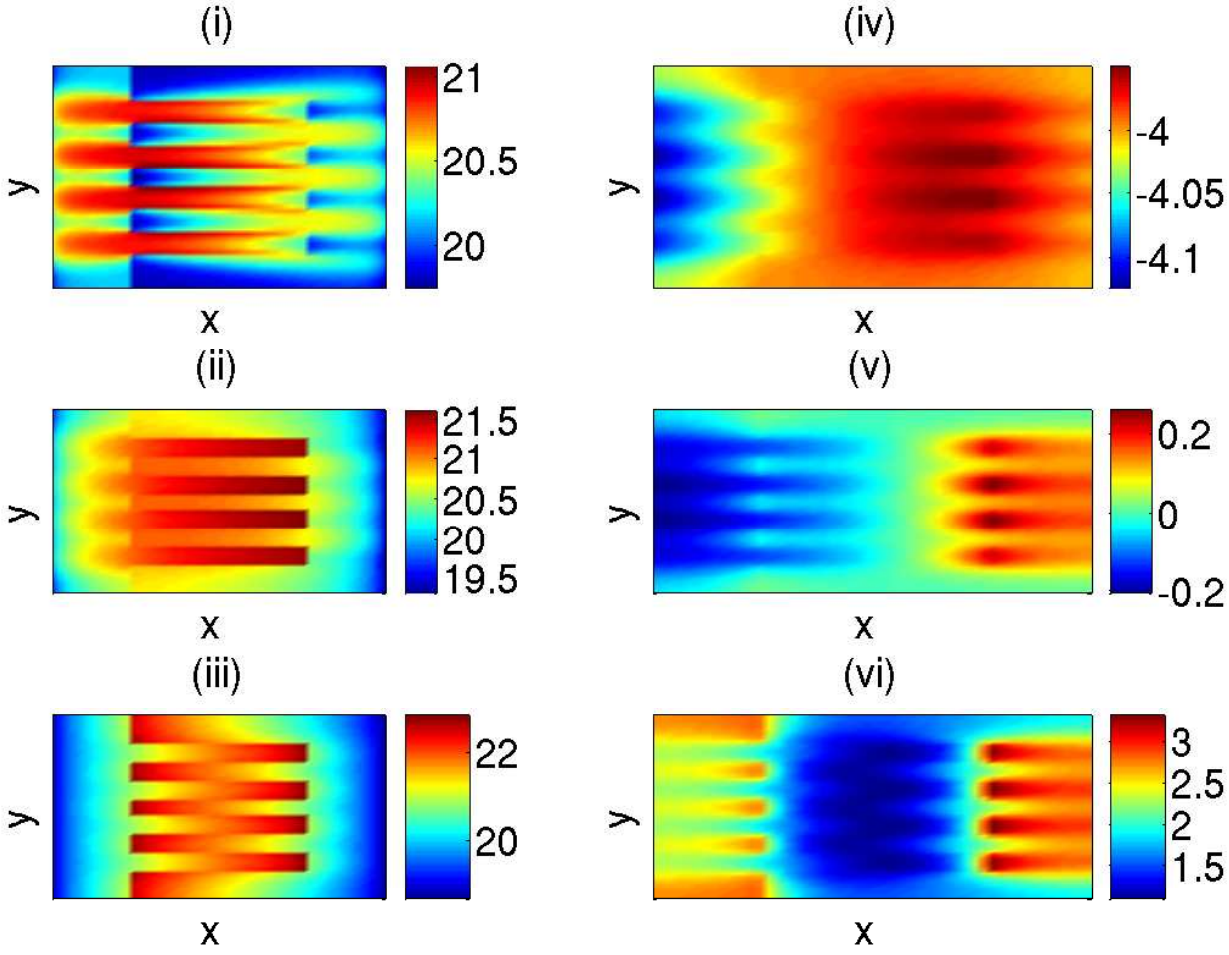

Figure 3.55: Colour plots for carrier density (base 10 logarithm) (i-iii) and resultant electric fields E_x (MVm^{-1}) (iv-vi) for L_{elec}=440nm and L_{int}=1072nm at varying applied bias for 1 Sun illumination. The top two figures are for short circuit, $V_a = 0$, the middle two for $V_a = V_{bi}$, and the bottom two for $V_a - V_{bi} = 0.3$V.

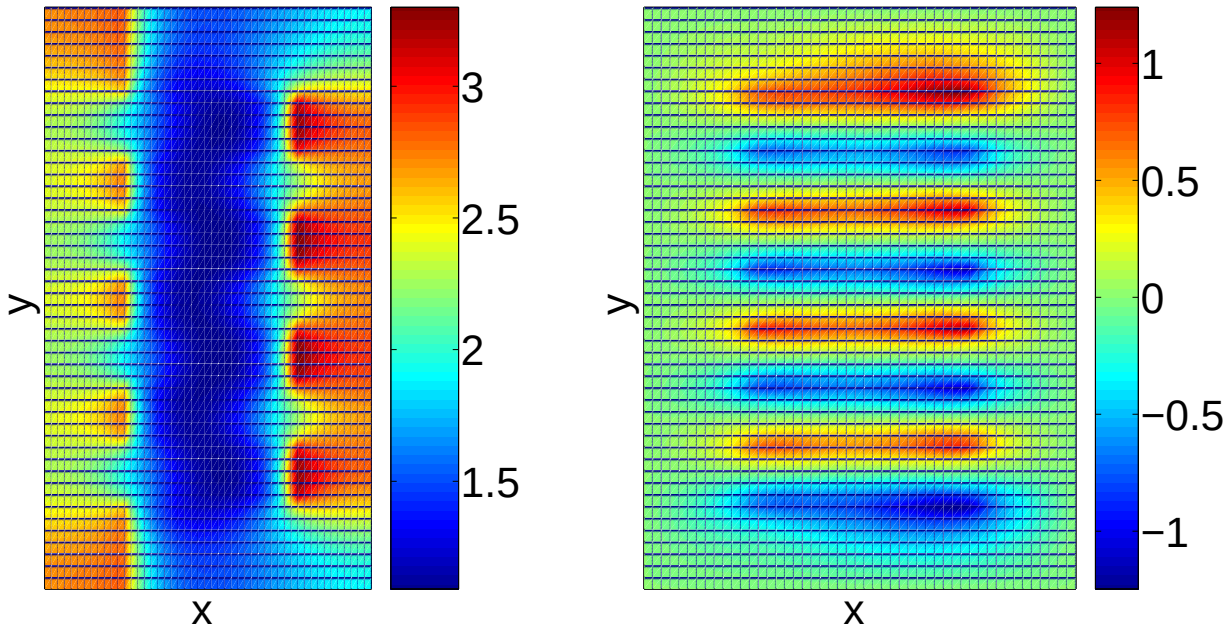

Figure 3.56: The x and y components of the electric field for the result in figure 3.55(vi) (MVm^{-1}).

in the x direction. This oscillatory behaviour in the field direction perpendicular to the electrodes has been observed before in simulation in figure 3(a) of reference [112].

The polaron pair dissociation rate increases as the x component of the electric field becomes either less positive or more negative. It is therefore of considerable interest to investigate if the field screening observed in figure 3.55 is having any noticeable effect on the open circuit voltage, which is a parameter of significant research interest. In order to do this, the value of the expression, V_P, defined above in equations 3.54 and 3.56 is compared to its value assuming that no field screening occurs, $V_{oc,lin}$. In this latter case, the electric field will be given by $\frac{V_{oc}-V_{bi}}{d}$. This comparison is performed in figure 3.57 where the percentage difference between these two quantities is shown.

It is evident that the V_{oc} does not always increase for higher intensities. It can be seen that as the length of the fingers increases, the tendency is to move from a relative decrease to a relative increase in V_{oc} compared to $V_{oc,lin}$. The same trend has been observed for the case of constant electrode length and therefore is not considered further here. It is therefore beneficial to device performance for the fingers to be as long as possible in order for the space charge effects reported here to have a positive effect on the V_{oc}.

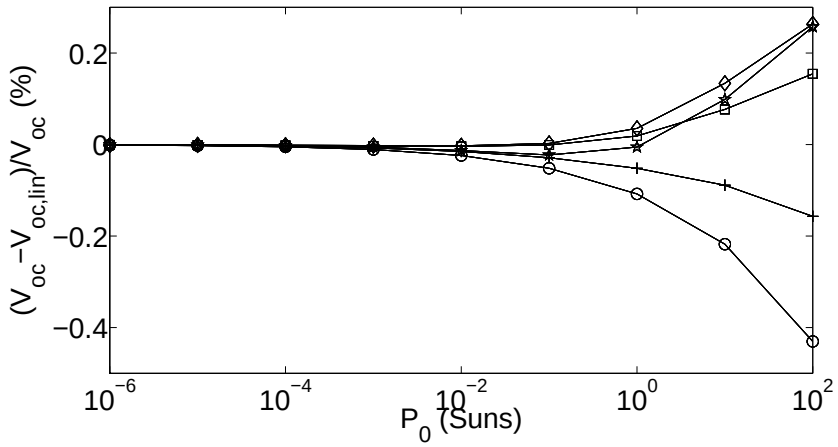

Figure 3.57: The effect of field screening on V_{oc} relative to the case in which the electric field is constant, $V_{oc,lin}$, for varying L_{elec}. In order of increasing length, the finger lengths are illustrated by ◯, +, □, ⋄ and ⋆.

3.9 Conclusions and further work

Idealised morphology polymer blend solar cells have been simulated both with and without intermediate charge transfer states and also with varying ratios between the heterojunction area and the electrode area.

In agreement with previously published experimental and theoretical studies, the internal quantum efficiency has been shown to be a complex function of the morphology. However, this work takes this a step further by consideration of two different morphology schemes, where the ratio of heterojunction length to electrode length is fixed or varying. This difference has been shown to have a significant effect on device performance.

Many experimentally relevant parameters have been investigated with the aim of providing 'rules of thumb' for the device behaviour with illumination intensity and morphology. The morphology has been shown to be crucial in determining the device performance. Reduced charge transport efficiency at high intensities has been shown to be a significant loss factor affecting currents at short circuit and maximum power point which, in turn, degrade the other solar cell parameters of interest. Geometrical factors have been consistently shown to be crucial for understanding the quantum yield in organic solar cells. The active area fraction is a critical parameter for understanding device performance since only excitons generated within an exciton diffusion length of the heterojunction can contribute to the photocurrent. Additionally, the ratio of active area to interface length should be optimised in order to maximise the open circuit voltage.

Electric fields have been shown to have a significant influence upon all aspects of the device physics, particularly at high intensities where space charge effects tend to be detrimental to device performance through reduction of polaron pair dissociation. An equation describing the various losses at open circuit has been derived which provides a bridge between two previously published models: one describing a bilayer device and the other a bulk heterojunction. Both of these models are able to use simplifications which cannot be utilised here. For example, the space charge effects in the interdigitated model are more complex than either of the two predecessors due to the inherently multi-dimensional architecture. Direct application of this model has shown the presence of polaron pairs can account for an open circuit voltage loss of up to 80mV. With further relation to space charge effects, electric field screening has been observed in the interface region. This has been shown to have a relatively small effect on the open circuit voltage, although the length of the fingers should be maximised to increase the potential increase in the open circuit voltage brought about by electric field screening.

Future work should extend the model to give a better quantitative understanding of the origin of V_{oc} by including the energetics of exciton separation at the polymer-polymer heterojunction. This is necessary because the work presented here assumes that *all* excitons which reach the heterojunction are dissociated, either into free charges or polaron pairs. In reality, this dissociation will only occur if the resulting charge-transfer state is lower in energy than the original exciton. The modelling of hybrid organic-inorganic systems such as those reported by Coakley *et al.* is a possible future avenue for research using this simulation scheme and would require minimal modification of the existing framework [31, 32]. The experimental morphologies of these hybrid systems (specifically those containing ZnO nanorods) can be much more akin to the idealised, interdigitated systems considered here when compared to the more frequently used bulk heterojunction devices, for which accurate devices models already exist [73]. Previous studies have shown that device performance can be optimised by varying the layer thickness in organic solar cells due to optical interference effects. This has been performed for bulk heterojunction [107] and bilayer devices [84] and it would be instructive to carry out similar studies on the ideal morphology devices considered in this work.

Chapter 4

Simulation of dendrimer OLEDs

Dendrimers are a novel form of organic molecule wherein the separate properties of solubility and colour of light emission, for example, can be tuned in isolation. This is because different parts of the molecule perform different tasks. This is in contrast to standard conjugated polymers where changing the side groups attached to the backbone of the structure would tend to affect the solubility and the emission range. In this chapter, the numerical model of the previous chapter is used to simulate experimental current-voltage characteristics and extract parameters of interest such as the injection barrier height and the equivalent circuit series resistance. No generation of charges from incident light is considered and hence excitons and polaron pairs are absent.

4.1 Introduction

A dendrimer is a branched molecule consisting of a conjugated core, conjugated dendrons and surface groups [113, 114, 115]. Figure 4.1 illustrates a generic dendrimer molecule.

Dendritic architectures hold out significant promise in the field of optoelectronics due to the spatial separation of their functional properties. In an OLED configuration the dendrimer core controls the colour of light emission and the electron affinity and the surface groups control the solubility [116, 113]. Charge transfer can occur between the core or the dendrons however. The light-emitting core is then able to be processed in solution and enables the electronic and manufacturing properties to be optimised separately [113, 115, 116, 117] as opposed to the behaviour in small molecule devices and co-polymers [116].

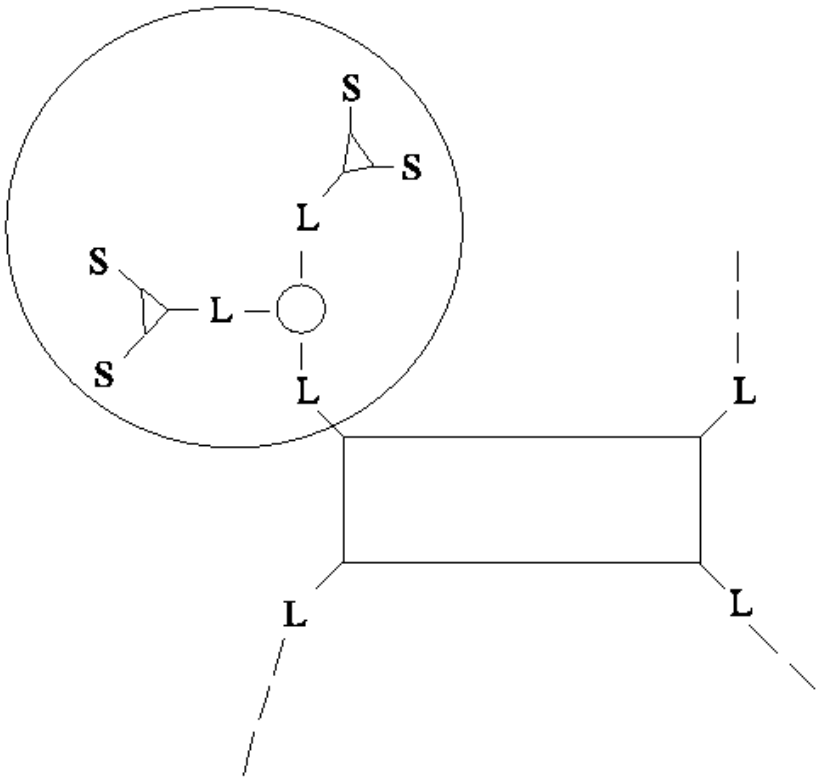

Figure 4.1: Schematic molecular structure of a dendrimer molecule. The central rectangle is the core, **L** is a linker and **s** is a side group. The large circle in the upper left indicates a dendron. The dotted lines in the bottom and top right corners indicate parity with the top left. Adapted from [113].

Another unique property of dendrimers is the ability to build molecules of successive generation. Figure 4.1 illustrates a first generation structure. However, if there were another layer of dendrons attached to those of the first generation, then a second generation molecule would result. In dendrimers of high generation, it will generally only be the surface groups or outermost branches which will interact. This should tend to reduce the aggregation seen in some organic systems, which is deleterious to device operation [115, 116]. The attachment of surface groups can enable the development of new materials made from previously studied chromophores, which otherwise would not be processible due their insolubility [113, 115]. The efficiency of dendrimer OLEDs is found to depend on the generation with almost an order of magnitude increase when a first generation material is exchanged for its second generation equivalent having been reported in the literature [116]. Additionally, the efficiency has been shown to be improved if a bilayer configuration is used [113] and active layer thickness has been shown to affect the colour of light emission, giving another means by which to vary the emission spectrum [113].

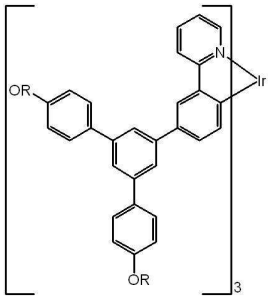

Figure 4.2: Chemical structure of dendrimer **1**.

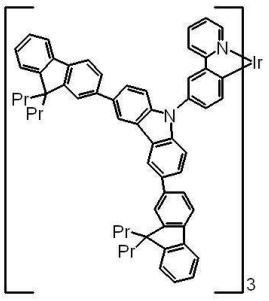

Figure 4.3: Chemical structure of dendrimer **2**.

A further advantage of the separate nature of the core and branches is that if the HOMO-LUMO splitting of the core regions is smaller than the branched regions, then excitations will tend to be directed toward the core [116] where recombination occurs. This is an advantage for an OLED since the goal is to bring electrons and holes together to drive the electroluminescence. It has also been suggested that transfer of charges to the core may also facilitate charge recombination due to the formation of an electric field [115, 113]. The funneling of charges to the core can also be achieved by making the conjugation length of the dendrons shorter than that of the core [117]. These factors mean that a single dendrimer layer can have a function akin to that of a polymer LED with several layers [114].

In this work, single layer dendrimer OLEDs using the two molecules shown in figures 4.2 and 4.3 are studied. These two materials shall be referred to as dendrimers **1** and **2** respectively throughout and are both first generation materials. Dendrimer **1** has cores of *fac*- tris(2-phenylpyridine) iridium, [$(Irppy)_3$], with phenylene dendrons covalently bonded to it [118]. This material has been used previously for LED applications and exhibits core to core transport properties [119]. Material **2** contains carbazole moieties, which have been shown to transfer the transport of the molecule to the dendrons [120].

4.1.1 Experimental method

Both dendrimers studied here are soluble in chloroform and were spin-coated onto various substrates which were cleaned before deposition. All devices studied here had the same sandwich device architecture; an injecting bottom anode contact (ITO, ITO-Au, Au or Pt), the dendrimer layer and a top metal cathode electrode (Al, Au, Pt or Ca). Electrode materials were deposited at pressures of 3×10^{-6}mbar but between the electrode application stages the device was removed from the evaporator in order to spin coat the dendrimer. The device characterisation was taken at room temperature in air and in the dark. The fact that the device was not kept in vacuum during the

Material	Workfunction	LUMO	HOMO
ITO	5.1 [122]	-	-
Au	5.2 [123]	-	-
Pt	5.5 [123]	-	-
Al	4.3 [124]	-	-
Ca	2.9 [125]	-	-
Dendrimer **1**	-	2.5 [120]	5.6 [120]
Dendrimer **2**	-	2.5 [120]	5.7 [120]

Table 4.1: Electrode work functions for dendrimer devices.

	Dendrimer **1**	Dendrimer **2**
T (K)	300	300
μ_{p0} ($m^2V^{-1}s^{-1}$)	9.3×10^{-11} [119]	1.2×10^{-9} [120]
γ ($V^{-1/2}m^{1/2}$)	3.4×10^{-4} [119]	3×10^{-4} [120]
$N_{C(V)}$ (m^{-3})	10^{27} [55]	10^{27} [55]
d (nm)	100	100

Table 4.2: Invariant parameters for device simulation.

entire manufacture and testing process means that impurities are likely to have been taken up by the device, which may adversely affect the performance. This point will be discussed in detail below.

Most of the devices considered here are hole only. That is, the barrier for electron injection is so high as to make the electron component of the current negligible. A table of literature electrode work functions is shown in table 4.1 as well as the frontier orbitals for the dendrimers used [1].

4.2 Methods

Due to the large number of simulation parameters involved (band edge density of states, mobilities, field dependence of mobilities, barrier height for the thermionic emission etc.), the data has been simulated within as consistent a parameter set as possible. That is, keeping many parameters constant with values obtained from experiment where available. Values of the invariant parameters used are given in table 4.2.

[1]The work function of ITO is poorly characterised and values ranging from 4.1-5.53eV can be found in the literature [121]. A more recent value is quoted here, noting that it is only the relative value of the electrode work function to the frontier orbital levels which controls the device behaviour in the simulations.

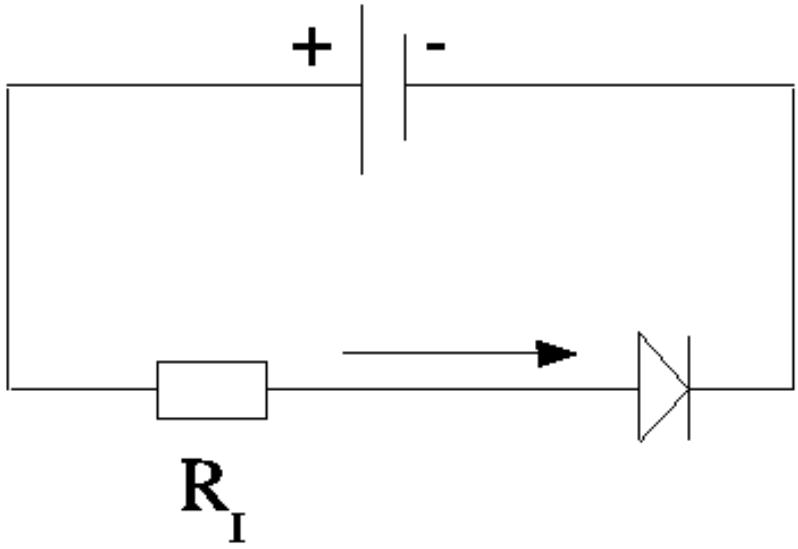

Figure 4.4: Equivalent circuit diagram of the dendrimer transport region (diode symbol) and the series resistance R_I. The horizontal arrow shows the direction of hole flow.

4.2.1 Series resistance

To simulate the current-voltage characteristics of different materials, the barrier for hole injection from the metal work function into the dendrimer HOMO is varied to change the magnitude of the resultant current. It has been shown consistently in this work that varying the value of the injection barrier height and the zero-field mobility, to a very good approximation, only affects the magnitude of the current, not the gradient. As a general rule, it has been found that an increase in the injection barrier height by 0.1eV has a similar effect on the current magnitude as decreasing the hole mobility by a factor of 10. To vary the gradient of the current with respect to the voltage, the parameter controlling the field-dependence of the mobility, γ, could be varied as in reference [126]. However, this parameter is available for both materials under consideration. Therefore, γ is kept constant throughout and an equivalent circuit series resistance, R_I, is introduced as shown in figure 4.4.

The approach of using a series resistance in an equivalent circuit for an organic device model has been used previously to simulate degradation at the interface between layers of polyethylenedioxythiophene/polystyrenesulphonate (PEDOT:PSS) and a fluorene based polymer [127]. The first step to simulating this problem is to find a value of the injection barrier height which gives the correct order of magnitude of the current. Values from table 4.1 can be used as a starting point and a current-voltage characteristic is generated. This then gives the relationship between the applied bias and the current

assuming that all of the bias falls across the dendrimer layer; i.e. $R_I = 0$. This yields the differential resistivity of the active layer and therefore the current given the potential difference across the dendrimer. Now, consider a finite resistance in series with the organic layer. For a given current, the potential difference across the resistance can be obtained from Ohm's law. The bias across the dendrimer layer is then known from the original data and the current can be evaluated. Using this algorithm, the injection barrier height at the anode and R_I can be used as the *only* fitting parameters. This is because it has been found that the results are highly insensitive to the value of the barrier height at the counter electrode. Expressed mathematically,

$$V_{\text{dendrimer}} = V_a - IR_I, \tag{4.1}$$

where $V_{\text{dendrimer}}$ and V_a are the potential differences across the dendrimer and the entire system respectively and I is the current. Therefore, when fitting current-voltage characteristics, $V_a = V_{\text{dendrimer}} + IR_I$ is plotted against I. In the numerical simulation there is no resistance present, and so the results obtained from the numerical model are $V_{\text{dendrimer}}$ and I.

4.2.2 Ensuring zero current at zero applied bias

A simple thought experiment shows that a current flowing at zero applied bias (optical and electrical) in an OLED must be unphysical. One simply has to imagine a battery isolated from any leads, in which case the current has nowhere to flow to. It will now be shown that this result follows straightforwardly from consideration of the boundary conditions on the electron density and electrostatic potential. To begin with, any effects altering the height of the charge carrier injection barrier will be neglected. The analysis is deliberately kept as general as possible, without explicit consideration of the precise form of the governing equations themselves. The following Neumann boundary condition for the flux, Γ, of electrons into the device is used,

$$\begin{aligned} \Gamma_{1(2)} &= v_{rn}\left(n_{eq1(2)} - n_{1(2)}\right) \\ &= J_{inj} - J_{rec}. \end{aligned} \tag{4.2}$$

This gives the flux of electrons - *not* the flux of charge, which would require an extra factor of e - at the left hand side (1) and the right hand side (2), v_{rn} is the recombination

velocity, n_{eq} is the equilibrium density when no current flows and $n_{1(2)}$ is the electron density at the left (right) hand side of the device. The term

$$J_{inj} = v_{rn} n_{eq}, \tag{4.3}$$

represents the thermionic injection of electrons into the conduction band of the semiconductor from the electrode [77] and the term.

$$J_{rec} = v_{rn} n, \tag{4.4}$$

is the backflowing interface recombination current [77]. Complimentary to this is the Dirichlet condition on the electrostatic potential, ψ [128],

$$\psi_{1(2)} = -\phi_{Bn1(2)}. \tag{4.5}$$

The transport of electrons is by a combination of drift and diffusion and the bulk electron current density is given by

$$J_n = e\mu_n n E + eD_n \frac{\mathrm{d}n}{\mathrm{d}x} = -e\mu_n n \frac{\mathrm{d}\phi_n}{\mathrm{d}x}. \tag{4.6}$$

The final equality defines the electron quasi-Fermi level, ϕ_n,

$$\phi_n = \psi - \frac{k_B T}{e} \ln\left(\frac{n}{N_C}\right). \tag{4.7}$$

From equation 4.7, it is clear that the current will only go to zero if the gradient of the quasi-Fermi level vanishes everywhere in the device. This can only be the case if

$$\phi_{n1} = \phi_{n2} \tag{4.8}$$

or

$$\psi_1 - \frac{k_B T}{e} \ln\left(\frac{n_1}{N_C}\right) = \psi_2 - \frac{k_B T}{e} \ln\left(\frac{n_2}{N_C}\right). \tag{4.9}$$

Assuming that the device current is zero yields $n_{1(2)} = n_{eq1(2)}$ from equation 4.2 and the values for $\psi_{1(2)}$ are known from the potential boundary conditions, equation 4.5. Therefore,

$$\psi_1 - \psi_2 = -\phi_{Bn1} - -\phi_{Bn2}. \tag{4.10}$$

Substituting from above gives

$$-\phi_{Bn1} + \phi_{Bn2} = -\frac{k_B T}{e} \ln\left(\frac{N_C \exp\left(\frac{-e\phi_{Bn2}}{k_B T}\right)}{N_C}\right) + \frac{k_B T}{e} \ln\left(\frac{N_C \exp\left(\frac{-e\phi_{Bn1}}{k_B T}\right)}{N_C}\right), \tag{4.11}$$

which yields

$$-\phi_{Bn1} + \phi_{Bn2} = -\phi_{Bn1} + \phi_{Bn2}. \tag{4.12}$$

Therefore, the form of the boundary conditions for the electron flux and the potential automatically ensure zero current at zero applied bias. A complication arises when it is considered that the boundary conditions are more complicated than considered thus far. Firstly, there is the Schottky barrier height lowering. To include this, the electron flux, Γ, is modified thus

$$\Gamma_{1(2)} = v_{rn}\left(n_{eq1(2)}\Theta - n_{1(2)}\right), \tag{4.13}$$

where $\Theta > 1$ represents the barrier lowering due to the Schottky effect. Therefore to keep the electron flux zero at zero applied bias, equation 4.13 must be modified as follows,

$$\Gamma_{1(2)} = v_{rn}\left(n_{eq1(2)}\Theta - n_{1(2)}\Theta_{eq}\right), \tag{4.14}$$

where Θ_{eq} is the value of Θ at zero applied bias. In addition, the injection-recombination formalism used here [55, 80] has two further additions to the expressions for the particle flux densities,

1. The injection term, $v_{rn}n_{eq1(2)}$, is multiplied by a factor $\theta < 1$ when the Schottky effect is not valid (the precise form of the equations is not important, only the physics of enforcing zero current at zero bias).
2. The interface recombination term, $v_{rn}n_{1(2)}$, is multiplied by a factor $\vartheta > 1$ when the Schottky effect is valid.

For this formalism to be successfully applied, the sign of the electric field at zero electrical bias is required because this affects the form of the equations. For example, the Schottky effect will not be present for holes at the left hand side of the device if the field is negative at zero bias; so $\Theta = 1$ and $\theta < 1$. Also $\vartheta = 1$ because this quantity only deviates from unity when the Schottky effect is valid. An example is now considered for the case of the hole current at the left hand side of the OLED where the electric field is negative at zero applied bias. Firstly, the Schottky effect is not valid here so that, as a first order consideration

$$\Gamma = v_{rp}\left(p_{eq}\theta - p\theta_{eq}\right). \tag{4.15}$$

This will ensure zero hole current. However, when a forward bias is applied, the electric field will change sign and become positive. In this case the Schottky effect will be 'turned on', represented by multiplication of the injection term by $\Theta > 1$. Therefore

$$\Gamma = v_{rp}\left(p_{eq}\Theta - p\theta_{eq}\right). \tag{4.16}$$

The factor θ has disappeared from the left hand term of the previous equation because it is now equal to unity but the θ_{eq} term *must* remain to ensure continuity of current as the electric field changes sign. Since the current on the left hand side has been dealt with, the current on the right hand side will not need any modification because charge continuity will ensure that it is zero on the other side also.

The Schottky effect in essence changes the shape of the potential profile near the electrode. However, the potential boundary conditions are invariant. That is, the value of the potential is kept the same at the electrode whether or not the Schottky

Device run	Anode	Dendrimer	Cathode	Bias direction
IV01	ITO	1	Al	+
IV02	Au	1	Au	+
IV03	Au	1	Au	-
IV04	ITO	2	Al	+
IV05	ITO	2	Au	+
IV06	ITO	2	Au	-
IV07	Au	2	Au	-
IV08	Au	2	Au	+
IV01b	ITO-Au	1	Au	+
IV02b	ITO-Au	1	Au	+
IV03b	Au	2	Au	+
IV06b	Au	1	Au	+
IV01c	ITO	1	Au	+
IV02c	ITO	1	Ca-Al	+
IV06c	ITO	2	Ca-Al	+
IV01d	Au	2	Al	+
IV02d	Au	2	Al	+
IV03d	Au	2	Al	-
IV04d	ITO-Au	2	Al	+
IV05d	ITO-Au	2	Al	-
IV06d	Au	1	Al	+
IV07d	Au	1	Al	-
IV08d	ITO-Au	1	Al	+
IV09d	ITO-Au	1	Al	-
IV01e	Pt	1	Au	+
IV02e	Pt	1	Au	-
IV03e	ITO	1	Pt	+
IV04e	Au	1	Pt	+
IV05e	Au	1	Pt	-
IV06e	ITO	2	Al	+

Table 4.3: Device structures used.

effect is valid. The Schottky effect only lowers the barrier for charge injection for one carrier at a time. That is, when the electron injection barrier height is lowered, the hole barrier is not lowered also, but is raised [55, 82] by an amount which is not equal to the Schottky lowering amount for the electrons, as is clear by comparing equations 3.20 and 3.23. What this means, is that if the potential boundary conditions tracked the values of the barrier heights of the respective carriers, then the difference between the potentials at the electrodes would not be equal to the built-in potential, V_{bi}.

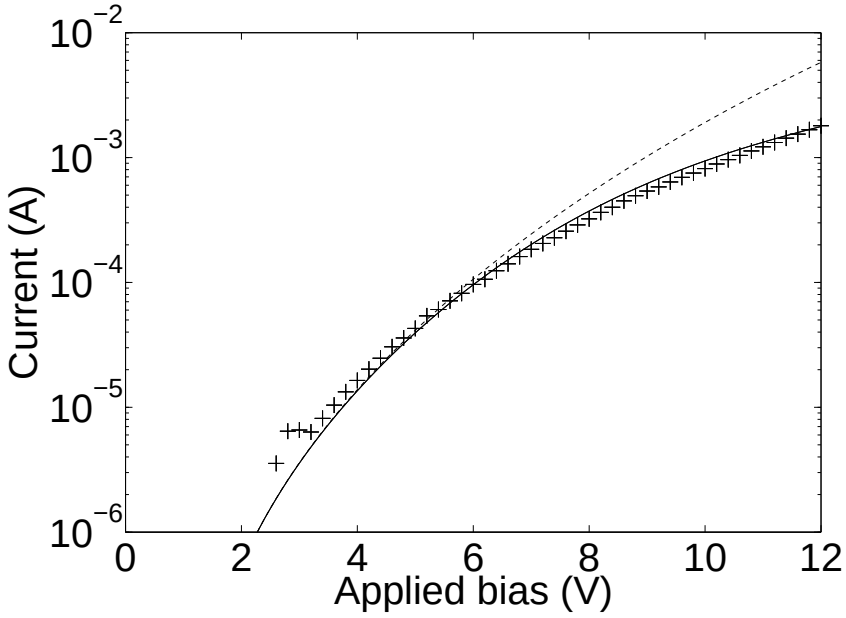

Figure 4.5: Experimental (+) and simulation fits to the current-voltage characteristics of an ITO/dendrimer **1**/Al device with (solid line) and without (dashed line) a series resistance of $1.2 \times 10^3\Omega$. The solid line fits the data considerably better, however at low bias the difference is small.

4.3 Results

Table 4.3 summarises all data that is considered in this chapter and an example of how the fitting of an experimental IV curve can be improved with the addition of R_I is shown in figure 4.5. It is clear that the addition of the series resistance decreases the current for a given applied bias as expected and justifies the use of this method as a fitting procedure. The difference between the two fits in figure 4.5 becomes increasingly marked at higher values of the applied bias since the correction due to the resistance is proportional to the current, given by equation 4.1. Many of the experimental data sets had curvature (that is $\frac{\mathrm{d}I}{\mathrm{d}V}$) which are considerably smaller than those obtained using the model with the experimental data for μ_{p0} and γ. These results will therefore benefit from having a series resistance term in their equivalent circuit.

4.4 Dendrimer 1 results

In table 4.4, the data describing the hole only devices for dendrimer **1** are given. Due to the large number of simulations carried out, it is not deemed necessary to show every fit obtained and therefore only one current-voltage characteristic for each injecting electrode material considered is shown in figure 4.6.

	ϕ_{Bp} (eV)	$\phi_{Bp}^{(SM)}$ (eV)	R_I (Ω)
ITO/**1**/Al*	0.4	0.5	1.2×10^3
ITO/**1**/Au	0.48	0.5	7×10^3
ITO/**1**/Pt	0.74	0.5	7×10^7
Au/**1**/Au	0.64	0.4	1×10^8
Au/**1**/Au	0.57	0.4	1.1×10^8
Au/**1**/Au	0.5	0.4	4×10^6
Au/**1**/Al*	0.69	0.4	0
Pt/**1**/Au	0.65	0.4	2×10^6
Au/**1**/Pt	0.7	0.4	5×10^6
ITO-Au/**1**/Au*	0.76	0.4 (Au)	0
ITO-Au/**1**/Au	0.76	0.4 (Au)	0
Au/**1**/Al*	0.64	1.3	0
ITO-Au/**1**/Al	0.55	1.3	2×10^6
Pt/**1**/Au*	0.61	0.1	0
Au/**1**/Pt	0.67	0.1	7×10^6

Table 4.4: Simulated hole injection barrier heights, ϕ_{Bp} (compared with values calculated from the Mott-Schottky model, $\phi_{Bp}^{(SM)}$) and the series resistance R_I for dendrimer **1**-based devices. The injecting electrode material is underlined in each case and the results marked with an asterisk are plotted in figure 4.6.

4.4.1 ITO injecting electrodes

Firstly considering Al as an electrode material, there will be a large barrier to hole injection into dendrimer **1** because there is a large offset of 1.3eV between the Al work function of 4.3eV and the dendrimer HOMO level of 5.6eV. The barrier for electron injection is expected to be roughly 1.8eV and therefore, the injection of electrons and holes is expected to be suppressed. The barrier for hole injection in the ITO case is expected to be just 0.5eV. Because of these two effects, the device current is expected to be hole only. This makes an important assumption, i.e. that the barrier for injection of electrons (holes) is given by the difference between the metal work function and the dendrimer LUMO (HOMO). This is the Mott-Schottky model which will be considered in further detail below. Table 4.4 shows that the value of the hole injection barrier at the ITO/dendrimer **1** interface is fitted as 0.4eV, this is smaller than the 0.5eV value given by the Mott-Schottky model and may be attributable to the fact that the work function of ITO can be altered depending on the way it is prepared [129].

In this same device structure, figure 4.6 shows that a significant current was recorded. However, no electroluminescence was present and therefore the device was not functioning as an OLED. This indicates that the electron injection is sufficiently poor to prevent significant bimolecular charge recombination occurring, which will in turn give

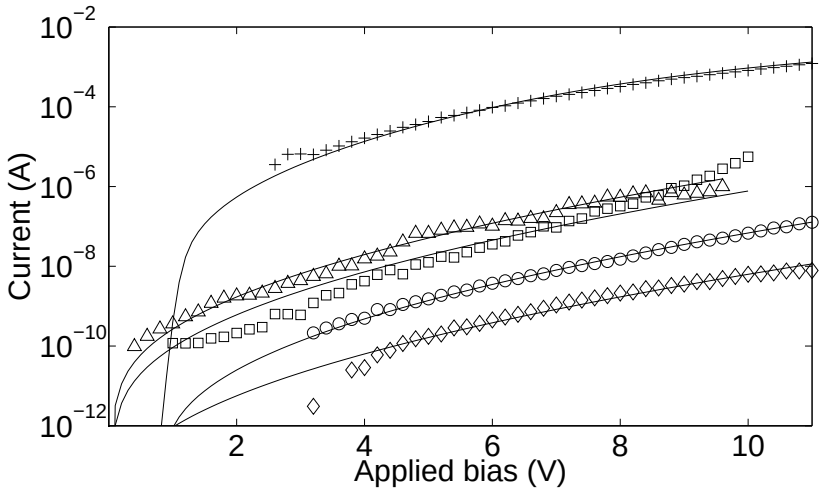

Figure 4.6: Current-voltage characteristics for dendrimer **1**. The different injecting contact materials are underlined, ITO/dendrimer **1**/Al (+), Pt/dendrimer**1**/Au (△), Au/dendrimer **1**/Al(□), Au/dendrimer **1**/Al (◯), ITO-Au/dendrimer**1**/Au (⋄). The symbols are the experimental data and the solid lines are the simulation data.

rise to light emission. This justifies the above assumption made above that the Al cathode gives rise to negligible electron injection.

To further investigate this, an ITO/dendrimer **1**/Au device was fabricated. In substituting Al for Au, the increase in the cathode work function of ∼1eV is expected to decrease any electron injection still further due to the larger injection barrier. The same anode material is expected to keep the hole injection properties unchanged. However, it can be seen from table 4.4 that the fitted barrier for hole injection increases by almost 0.1eV. As mentioned above, it is found that an increase of the barrier height of this magnitude gives rise to a decrease in the current of roughly a factor of 10 in the simulation. It is therefore clear that the counter electrode material has a significant effect on device performance. Additionally, it is also possible that there exists a finite barrier layer through which holes must be extracted at the Au cathode. This could be due to contamination of the interface from air borne particulates incurred during device fabrication, which may also affect the Au work function [123]. The increase in the fitted value of the series resistance for the Au cathode device adds weight to this hypothesis that the counter electrode is somehow hindering hole transport.

The fact that the current is reduced by roughly a factor of 10 in moving from an Al to an Au cathode further gives further weight to the assumption that the current in these devices is hole only. This is because, to give such a marked decrease, 90% of the current in the former case would need to have been due to electron transport, which is unphysical here. It can therefore be said with some confidence that the devices considered thus far are hole only in nature.

The area of the devices considered throughout this work is $\sim 10^{-6}\mathrm{m}^2$ and therefore the sheet resistance of the ITO anode devices considered thus far compares well with previously reported results for conjugated polymer systems of $\sim 10^{8}\Omega\mathrm{m}^{-2}$ [127].

4.4.2 Au injecting electrodes

Devices with Au injecting contacts are now considered in detail to see what effect reducing the expected barrier height for hole injection has on the device characteristics. Replacing an ITO injecting anode with the higher work function metal Au would give an increase in the current assuming Mott-Schottky theory holds as is frequently assumed in organic device models [75]. With the exception of the third ITO anode device (where the counter electrode is Pt) the converse is seen however and the barrier is higher in the cases with Au injecting electrodes. This is unexpected from the above analysis and shows that the Au/dendrimer interface is of poorer quality than that between the dendrimer and the ITO.

The unusual properties of Au/organic polymer contacts have been noted before and were explained in terms of interfacial dipoles, which lower the Au work function and thereby increase the hole injection barrier [130, 131, 132].

The first three runs for Au injecting contacts in table 4.4 are of the structure Au/dendrimer **1**/Au. For these devices, values of the injection barrier of 0.64, 0.57 and 0.5eV respectively were obtained. For these values of the injection barrier, values of the R_I of between $10^6\Omega$ and $10^8\Omega$ were found. This large variation in both the values of ϕ_{Bp} and R_I is a further indication of the effect contamination can have on device performance. For the fourth run in table 4.4 (Au/dendrimer **1**/Al), a good fit can be obtained with a barrier of $\phi_{Bp} = 0.69$eV without the need for a series resistance. This indicates that the presence of a second Au contact further deteriorates the device performance. The fifth and sixth runs having an Au injecting contact have Pt counter electrodes and will be considered later.

4.4.3 ITO-Au injecting electrodes

The next electrode is a hybrid of the two previous materials; where Au is deposited on the ITO coated substrate to form the injecting contact. The counter electrode in these cases is Au as previously considered. This device structure requires the highest fitted value of the injection barrier height for any of the devices considered in this work using dendrimer **1**, thus giving a very low current, figure 4.6. It is again clear that Au

is hindering the device performance and that the presence of the ITO underlayer does not help to increase the current, but decreases it still further.

4.4.4 Pt as an injecting electrode and counter electrode material

The inclusion in this work of Pt as an electrode material is interesting because its work function has been reported to be very close to that of the HOMO level of dendrimer **1**. Reference [123] gives a value of 5.5V for its work function and the HOMO level of dendrimer **1** lies at 5.6eV. If this were the case in a device configuration then the injection of holes from Pt into the dendrimer would be barrierless [74] and should be simulated as an ohmic contact in contrast to the Schottky method used thus far (see table 4.4 for numerical details). Simulations with ohmic injecting electrodes, however, gave currents which were too large to be fitted even with a large value of R_I. The use of an injection barrier at the Pt/dendrimer **1** interface was therefore needed to fit the data. Two device structures were considered using Pt as the injecting contact; Pt/dendrimer **1**/Au and Au/dendrimer **1**/Pt. The values of the fitted barrier heights (0.61eV and 0.67eV respectively) are sufficiently similar to give confidence that this fitting method is suitable. In addition to these devices, 3 devices with Pt counter electrodes were also examined. Of these, the 2 Au devices were fitted with ϕ_{Bp} values of 0.65eV and 0.7eV and very similar values of R_I. Finally an ITO/dendrimer **1**/Pt device was fitted with a 0.74eV barrier and a high series resistance of $7\times10^7\Omega$.

Why the ITO/dendrimer **1**/Pt device should have such poor performance is not clear. However, it is of note that the series resistance is required for a good fit for all of the devices where Pt is present as the counter electrode but not where it is the injecting electrode. This raises the interesting possibility that there is a finite barrier for the extraction *and* injection of holes at a Pt electrode. This is because a large series resistance is required for Pt used as the counter electrode, and also that the devices with a Pt injecting electrode cannot be fitted with ohmic contacts.

For the device structure Pt/dendrimer **1**/Au, the experiment needs to be run in reverse bias (negative bias on Pt side) for Au to constitute the injecting contact. From a simulation point of view, this is no different from applying a positive bias to the Au contact. Therefore, the two experiments Pt/dendrimer **1**/Au (reverse bias) and Au/dendrimer **1**/Pt (forward bias) were simulated identically. The hole injection barrier heights and series resistances for these two cases can be seen to agree favourably (see table 4.4). This further supports the use of the modelling methodology employed here.

	ϕ_{Bp} (eV)	ϕ_{Bp}^{SM} (eV)	R_I (Ω)
<u>ITO</u>/**2**/Al	0.4	0.6	0
<u>ITO</u>/**2**/Au*	0.54	0.6	7×10^5
<u>ITO</u>/**2**/Al	0.68	0.6	1×10^5
ITO/**2**/<u>Au</u>	0.55	0.5	4×10^6
Au/**2**/<u>Au</u>	0.80	0.5	0
<u>Au</u>/**2**/Au	0.80	0.5	0
<u>Au</u>/**2**/Au	0.82	0.5	1×10^8
<u>Au</u>/**2**/Al	0.6	0.5	3×10^5
<u>Au</u>/**2**/Al*	0.71	0.5	0
<u>ITO-Au</u>/**2**/Al*	0.48	0.5 (Au)	4×10^4
Au/**2**/<u>Al</u>	0.72	1.4	0
ITO-Au/**2**/<u>Al</u>*	0.56	1.4	6×10^4

Table 4.5: Simulated hole injection barrier heights, ϕ_{Bp} (compared with values calculated from the Mott-Schottky model, $\phi_{Bp}^{(SM)}$) and the series resistance R_I for dendrimer **2**-based devices. The injecting electrode material is underlined in each case and the results marked with an asterisk are plotted in figure 4.7.

4.4.5 Al injecting electrodes

Lastly, devices consisting of an Al injecting electrode were considered. A very large injection barrier was expected to be found because the difference between the vacuum work function of the Al and the dendrimer **1** HOMO is 1.3eV. However, values of 0.55eV and 0.64eV were found. This result adds further weight to the hypothesis that the Mott-Schottky model is not valid under many of the situations considered herein.

4.5 Dendrimer 2 results

Several similar device structures are now considered using dendrimer **2** as the active layer and the parameters obtained from simulation are given in table 4.5.

4.5.1 ITO and Au injecting contacts

As before, ITO injecting electrodes are considered first. Upon substitution of different counter electrodes, no immediate pattern is seen. However, the same general increase in fitted barrier heights (noted above for dendrimer **1**) is seen when ITO is replaced by Au as the injecting contact. The device structure Au/dendrimer **2**/Au requires a larger barrier height than that of any of the other devices where Au is only present

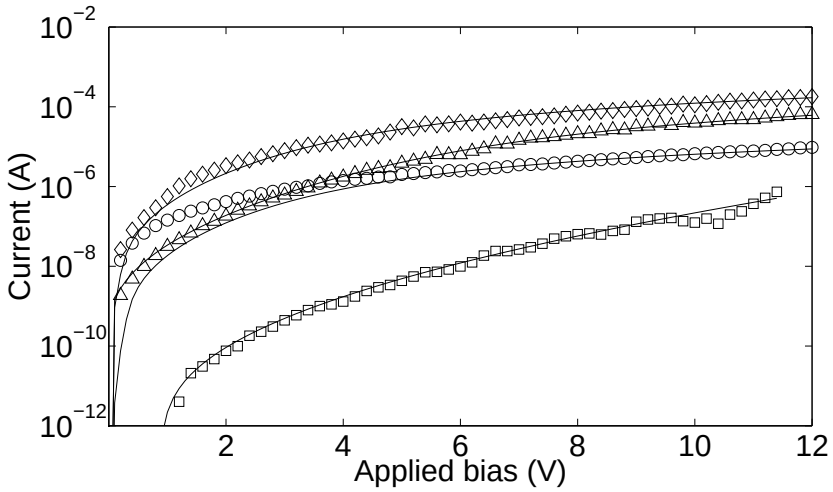

Figure 4.7: Current-voltage characteristics for dendrimer **2**. The different injecting contact materials are underlined, ITO-Au/dendrimer **2**/Al (⋄), ITO-Au/dendrimer **2**/Al (△), ITO/dendrimer **2**/Au (◯)and Au/dendrimer **2**/Al (□). The symbols are the experimental data and the solid lines are the simulation data

as the injecting contact. This gives increased weight to the hypothesis given above for dendrimer **1** that there exists a thin barrier layer for extraction at Au and Pt counter electrodes.

4.5.2 ITO-Au injecting contacts

For an ITO-Au injecting anode, the fitted value of the barrier height is unexpectedly low at just 0.48eV. This was a surprising result for two reasons. Firstly, a barrier for hole injection of 0.76eV at the ITO-Au/Dendrimer **1** interface has already been fitted and secondly, the dendrimer **2** HOMO lies at 5.7eV compared to 5.6eV for dendrimer **1**. In this case, an *increase* in the barrier would therefore be expected, not the observed decrease. A significant difference between these results however is that for the dendrimer **1** case, the counter electrode is Au, whereas in this case it is Al. This is in agreement with the results presented above which show worse device performance when Au is used as the counter electrode.

There are examples in the literature of a barrier for the extraction of electrons from organic optoelectronic devices [133, 134] and in fact, these studies have shown this to be beneficial to device performance. The reason for this is that the electrons build up at the extraction barrier and increase the electric field strength there, thereby increasing hole injection. An extraction barrier has not been considered herein, however it would be an interesting addition to the modelling procedure to do so and would be a departure from the frequently used assumption that the counter electrode has little or no effect

on device performance. The conclusions reached in references [133] and [134] will not be directly relevant here since only unipolar devices have been considered thus far. However, consideration of related space charge effects in bipolar dendrimer devices are considered below.

4.5.3 Al injecting contacts

The final hole-only device structures to be considered have an Al injecting contact and has been fitted with a barrier for hole injection very much smaller than that expected from the Mott-Schottky model. This further emphasises the inability to predict the barrier heights from literature values of electrode work functions and organic material frontier orbital levels as consistently noted above and is in agreement with the results found for dendrimer **1** attached to Al injecting contacts.

4.5.4 Comparison between the dendrimers for the device structure Au/dendrimer/Al

An interesting comparison between the current-voltage characteristics of the two dendrimers can be seen for the structure Au/dendrimer/Al, where Au is the injecting contact. The current for the dendrimer **1** device (fitted without a series resistance) is smaller than when the dendrimer is swapped for dendrimer **2**. This is the case even though the fitted barrier height for the former device is the smaller of the two. This counterintuitive conclusion can be rationalised by noting that dendrimer **2** has a higher value of μ_{p0}. This is also evidence for the differing ways holes are transported in the two dendrimers; that is, hopping between localised states in the molecular core for dendrimer **1** and between the branches, or dendrons, of dendrimer **2** [119, 120].

4.6 Bipolar device performance

All of the devices considered thus far have contained only holes as mobile charges. Therefore, to be able to model the transport characteristics of devices containing electrons *and* holes with confidence, the properties of devices containing only electrons need to be considered first. The bipolar devices considered later have the struture ITO/dendrimer/Ca-Al and Ca has a work function of just 2.9eV, which is considerably smaller than the electrodes considered thus far. Since the two dendrimers have a common LUMO level of 2.5eV, a large number of electrons can be expected to be injected

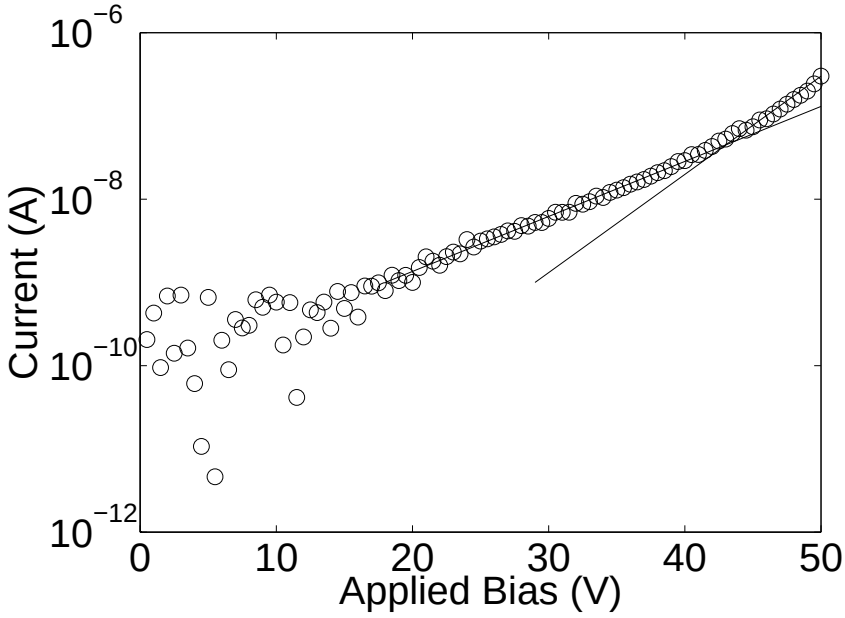

Figure 4.8: A current-voltage characteristic for a Ca-Al injecting contact into dendrimer **1**. The solid lines represent the change in slope at the onset of tunneling.

over the 0.4eV barrier. Devices with two Ca-Al contacts were therefore considered to be electron only and their current-voltage characteristics were examined to try to obtain the relevant material parameters.

Due to significant noise in the experimental currents, considerably larger biases were needed to be applied to the electron only devices to obtain currents which increase monotonically with applied bias over a bias range of roughly 10V or more. The highest bias in these cases were roughly 50V, much larger than the maximum of 15V for the hole only devices. At these large applied voltages, tunneling will tend to be the largest component of the device current [77]. An abrupt change in the slope of the current-voltage curve at high voltage is the signature of tunneling controlling the device behaviour and is evident in figure 4.8 where Ca-Al is the injecting contact into a dendrimer **1**-based device.

4.6.1 Electron injection barrier height

Because a tunneling component to the injected current is not considered, the fitting algorithm as described above for fitting hole only device currents cannot be used for the electrons. The Fowler-Nordheim method was therefore used, which gives the barrier height for charge injection into a semiconductor given a tunneling current, I, and associated electric field, E [135]. In this method, $\ln\left(\frac{I}{E^2}\right)$ is plotted against $\frac{1}{E}$. The

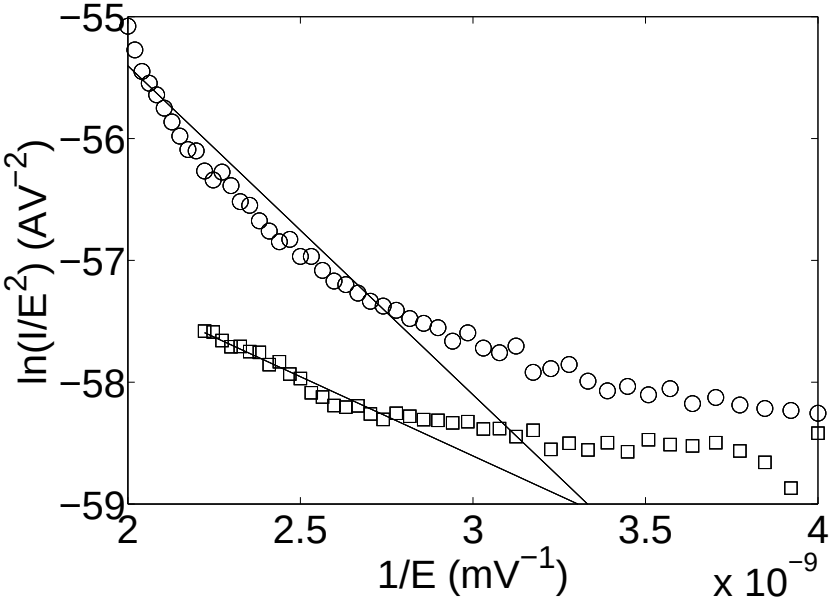

Figure 4.9: Fowler-Nordheim plots for dendrimer **1** (◯) and dendrimer **2** (□). The devices are assumed to be electron only with Ca-Al injecting electrodes. Equation 4.17 is assumed to hold in the region indicated by the the solid lines.

gradient, κ, yields the barrier for injection, ϕ_{Bn}, from equation 4.17

$$\kappa = \frac{8\pi \left(2m^*\right)^{1/2} \phi_{Bn}^{3/2}}{6\pi\hbar e}, \tag{4.17}$$

where m^* is the effective mass (taken to be equal to the free electron value here). Figure 4.9 shows the relevant Fowler-Nordheim graphs for dendrimers **1** and **2**.

The fitted barrier heights were 0.6eV for dendrimer **1** and 0.3eV for dendrimer **2**. Since the two materials have the same LUMO level of 2.5eV, it was expected that the value of the injection barrier would be the same for both dendrimers considered. The fact that this is not the case is a further indication that the Mott-Schottky model is not necessarily a good indicator of the actual barrier height for charge injection in a real device. This also shows that this is possibly the case for electrons as well as holes, as found previously. It should be noted however, that the gradient of the Fowler-Nordheim graph for dendrimer **1** in figure 4.9 is not as constant as that of dendrimer **2**. Since the premise of the method is that the current is dominated by tunneling, this non-linearity in figure 4.9 may be an indication that there is a finite thermionic emission component to the injection current in the dendrimer **1** case.

The other parameters needed for the simulation of the bipolar devices are the electron

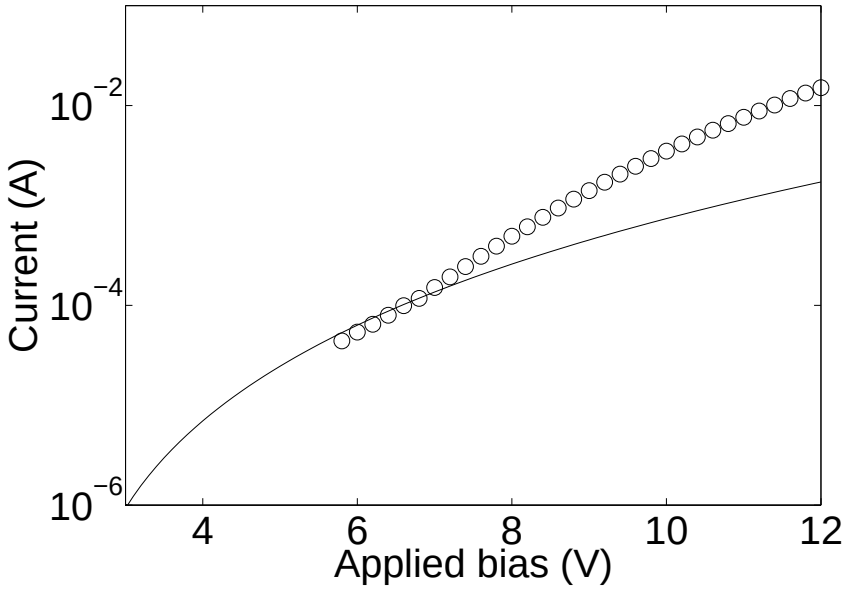

Figure 4.10: Simulated (solid line) and experimental (◯) current-voltage characteristics for an ITO/**2**/Ca-Al device.

mobility factors μ_{n0} and γ_n. These parameters have not been experimentally obtained for either dendrimer, it is therefore postulated that $\gamma_n = \gamma_p$ and that $\mu_{n0} = \mu_{p0}/100$ since both materials are preferentially hole transporting. This latter assumption has been used previously for the relationship between majority and minority carrier mobilities in organic polymers [136, 137, 138]. Figure 4.10 shows the simulated and experimental current-voltage characteristic for an ITO/dendrimer **2**/Ca-Al device.

The fit of the simulation in figure 4.10 is encouraging since the model gives the same order of magnitude for the current as seen experimentally. However, the slope of the experimental curve is higher than that obtained with the model. This means that the fit cannot be improved by the addition of a series resistance as this will always tend to reduce the gradient of the simulated data. The electron component of the simulated current here is significantly larger than the hole component and therefore better agreement could be found by using a larger value of γ_n. As mentioned above, $\gamma_n = \gamma_p$ here since no experimental value exists in the literature at present.

The simulation of the ITO/dendrimer **1**/Ca-Al device was not successful in that the predicted device current was ∼2 orders of magnitude too low. In light of the large barrier for electron injection into the device fitted above (0.6eV c.f. 0.3eV for the dendrimer **2** device), this is further indication that tunneling may not be the dominant current component in figure 4.9 above for the dendrimer **1** data and that the fitted barrier height is significantly too high.

4.6.2 Comparison of experimental bipolar device results

Now considering the bipolar results for the two dendrimers together, the current-voltage and external quantum efficiency characteristics obtained from experiment can be seen in figure 4.11. The currents given in figure 4.11 were higher than any other result containing either dendrimer respectively. This is indicative of a large electron component of the device current in both devices considered and justifies the use of Ca-Al as an electron injecting electrode material.

The external quantum efficiency in emissive devices will depend not only on the current (that is, the transport properties of the organic layer) but also the balance between transport and charge injection [74]. It has been found experimentally that, when the intensity of light emission is equal to 100 cdm^{-2}, the external quantum efficiency of dendrimer **1** is 0.21% and that of dendrimer **2** is lower at 0.14%. Biases of 6V and 8.8V need to be applied to the dendrimer **1** and **2** devices respectively to achieve this brightness level. Efficiencies as high as 16% have been reported for dendrimer **1** [139], significantly higher than those obtained herein, which is further evidence for the crucially important balance between injection and transport in OLEDs.

The bipolar devices considered here are of the structure ITO/dendrimer/Ca-Al. The hole mobility of dendrimer **1** has been experimentally shown to be smaller than that of dendrimer **2** and it is therefore assumed that the electron mobility in dendrimer **1** is also smaller. If this is the case, it is surprising that the current is larger for the dendrimer **1**-based device since the two have identical electrode materials.

The fitted electron barrier height for dendrimer **1** gave a simulated current which was significantly too low, so if it is assumed that the two devices have equal electron injection barrier heights, then the lower current for the dendrimer **2** device may be ascribed to a larger *hole* barrier height. Although it has been experimentally established that the hole mobility is larger in dendrimer **2**, the dendrons in this material are larger, and it is therefore possible that this deteriorates the electron transport. This would lower the electron mobility value in dendrimer **2** and may therefore give rise to a lower bipolar device current in spite of its higher hole mobility.

4.6.3 Space charge effects in bipolar devices

The charge densities and the electric field inside the dendrimer devices has also been considered in order to examine what rôle space charge effects play in device performance. Firstly, the bipolar device which was more successfully simulated is considered,

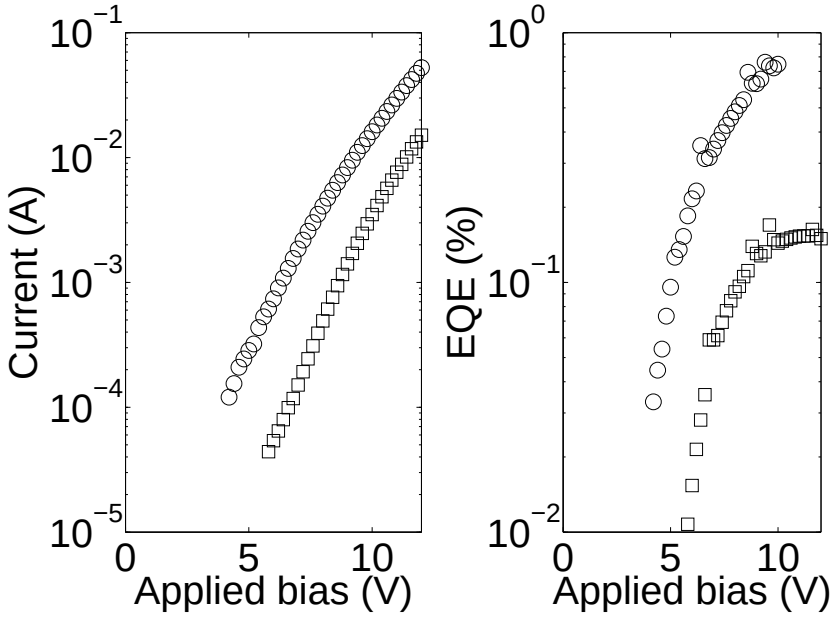

Figure 4.11: Current-voltage and external quantum efficiency plots for ITO/dendrimer/Ca-Al devices, where the active layer is dendrimer **1** (◯) and dendrimer **2** (□). The current-voltage curve for dendrimer **2** is the same as shown in figure 4.10.

that is, the ITO/dendrimer **2**/Ca-Al device. Figure 4.12 shows the electron and hole densities at an applied bias of 12V for the data considered in figure 4.10. It has been noted above that the current is dominated by the electrons because of the low electron injection barrier height and therefore the higher density of electrons seen in figure 4.12 is expected. The contribution of the holes to the resultant electric field profile is negligible because their density is so much lower than that of the electrons and a negative gradient in the electric field everywhere is therefore evident and is shown in figure 4.13.

Considering figures 4.12 and 4.13, it is clear that the electron density is exerting a noticeable influence upon the electric field in the device. It is interesting to note that the electron density exhibits a peak at the anode (left hand side) even though there is no barrier for extraction, as considered in the work of Murata *et al.* [133]. This is because the extraction rate for charge carriers in these simulations is proportional to their mobility [80]. Since the electron mobility is assumed to be only 1% of that of the holes, the electrons tend to accumulate at the extracting electrode. The fall in the hole density at the other side of the device in figure 4.12 is conversely due to the larger value of the hole mobility. If the electric field in the device were constant, it would be equal to 100MVm^{-1}. The fact that the deviation in figure 4.13 from the uniform electric field is relatively small implies that the increase in electron density at the left hand side will only have a minor effect on the device behaviour.

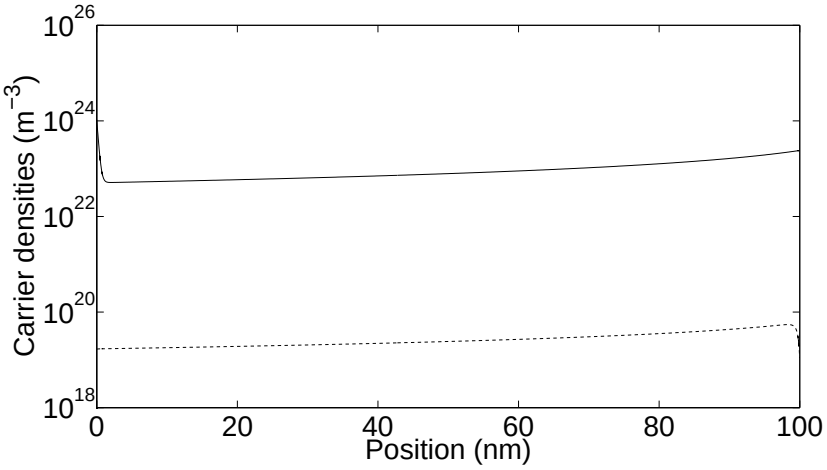

Figure 4.12: Electron (solid line) and hole (dashed line) densities for an ITO/dendrimer **2**/Ca-Al device at 12V forward bias. The anode (cathode) contact is on the left (right) hand side of the device.

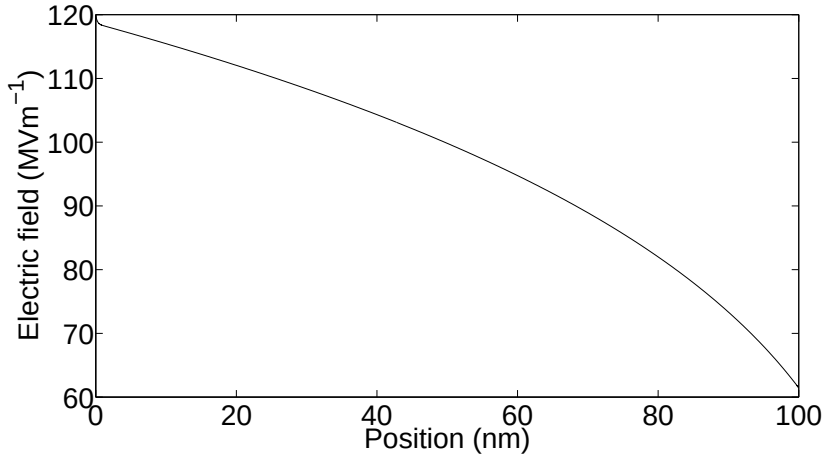

Figure 4.13: Resultant electric field for the carrier densities shown in figure 4.12.

Although the fitting of the ITO/dendrimer **1**/Ca-Al current-voltage characteristic was not successful, the carrier densities and electric field profiles in the device should be considered also. This is done at the same applied bias of 12V as for the ITO/dendrimer **2**/Ca-Al above in order to note any similarities or differences between the two bipolar devices. The electron and hole profiles are shown in figure 4.14. Firstly, the electron density is ∼4 orders of magnitude lower in this device compared to that when dendrimer **2** is the active layer. This can be attributed to the larger electron injection barrier of 0.6eV compared to 0.3eV for dendrimer **2**. The densities of electrons and holes are relatively low compared to the electron density for the dendrimer **2** device in figure 4.12 and therefore the electric field was found to be uniform across the device, with a value of 100MVm^{-1}. The peak in the electron density at the anode and the fall in the hole density at the cathode (due to the factor of 100 difference in their mobilities) are

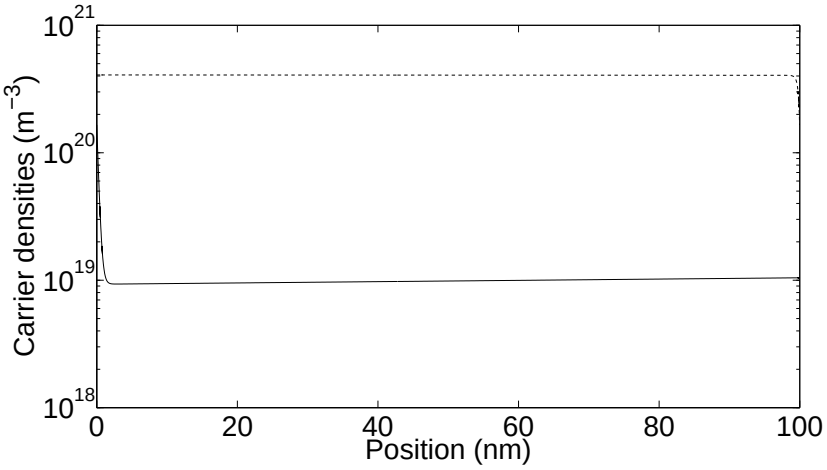

Figure 4.14: Electron (solid line) and hole (dashed line) for the structure ITO/dendrimer **1**/Ca-Al at 12V applied bias. The carrier densities are significantly lower than the electron density in figure 4.12 for an ITO/dendrimer **2**/Ca-Al device.

again evident in figure 4.14.

4.7 Invariance of effective electrode work function in hole only devices

It was mentioned above that the fitted barrier heights for many of the hole only devices were significantly different from the Mott-Schottky model. To probe this further, every hole-only current-voltage characteristic was fitted again without any additional series resistance in order to obtain values for the hole barrier heights (and hence, effective electrode work functions) with no further adjustable parameters. As can be seen from figure 4.5, the absence of R_I will mean that the quality of some of the simulated current-voltage characteristics will be worsened. However the large number of devices considered will give a better overall picture of the interface behaviour using different electrode materials. The injecting contact work functions, Φ were calculated using

$$\Phi = \text{HOMO} - \phi_{Bp}. \tag{4.18}$$

and the average value was found to be 5 ± 0.1eV with only 3 data points lying outside of the error bounds. The error bounds, $\pm\Delta$, are given by standard error equation,

$$\Delta = \frac{\sigma}{\sqrt{N_{trials}}}, \tag{4.19}$$

where σ is the standard deviation and N_{trials} is the number of devices considered. A similar conclusion has been reported recently [123] for junctions between the organic polymer α-sexithiophene and electrode materials which have vacuum work functions varying in excess of 1eV. By studying the barrier for the injection of holes in this case, it was found that the effective electrode work function changed by just 0.2eV.

A key similarity between the work in reference [123] and that presented here is that both sets of devices contained electrode-organic interfaces which had not been kept exclusively under vacuum. All the hole only devices presented here were tested under ambient conditions and the dendrimer layers were not deposited in vacuum, therefore leaving them open to contamination. The hole-only device characteristics are therefore expected to be substantially affected by the presence of contaminants. Reference [123] shows that an expected change in barrier height of $\sim$1eV is reduced to $\sim$0.2eV by the presence of impure contacts. However, the results presented here indicate that this effect may give rise to even more uniform injection barrier heights than given in reference [123]. This is because the difference between the work functions of Al and Pt has been reported to be as high as 1.2eV, but the results given above show a standard error of just 0.1eV.

4.8 Conclusions and further work

The current-voltage characteristics of phosphorescent dendrimer-based OLEDs have been considered using a detailed device model. The significant difference between the molecular structure of the active materials is that the dendrons of dendrimers **1** and **2** incorporated phenylene and carbazole respectively. The model contains realistic boundary conditions and drift-diffusion transport to simulate the device currents in order to extract the barrier height for the injection of majority carriers and the equivalent circuit series resistance.

It has been shown from inspection of many different device structures that the prediction of the injection barrier height from the Mott-Schottky model will invariably give substantially different results compared to those obtained from simulation. Au was found to be consistently deleterious to device performance, even when used as a counter electrode material. This is interesting because modelling studies of organic devices frequently ignore the effect of the extracting electrode on device performance.

Pt was found to form a blocking, Schottky, contact at interfaces with dendrimer **1**. This result is unexpected from consideration of the value of the vacuum work function for Pt, which has been reported to lie just 0.1eV above the dendrimer **1** HOMO level.

The transport characteristics of the two active materials considered here have been shown to be noticeably different from one another. For example, the higher bipolar device current for dendrimer **1** in spite of its significantly lower hole mobility. However, both materials show invariance of the injection barrier height with changing electrode work function, in agreement with recent literature reports.

The large electron density in a dendrimer **2** device containing electrons and holes has been shown to have a noticeable effect on the internal electric field. This will, however, not greatly affect the device performance because the deviation from uniformity is small. Additionally, the low electron mobility reduces the extraction rate at the anode, causing a peak in the density there. This is analogous to literature results which attribute electron accumulation to a physical barrier for electron extraction, which is not present in these studies.

The counter electrode has been shown to have a significant effect on device performance and future work on modelling these devices should consider charge extraction explicitly, perhaps including a barrier for charge injection as in references [133] and [134]. It would also be prudent to consider more electron only devices, especially at low applied bias, with a view to better understanding the bipolar properties of these materials. This would enable the fitting of electron barrier heights and series resistances without the need to resort to the Fowler-Nordheim formalism. This does rely on the availability of experimental data for the values of μ_{n0} and γ_n however, which are currently lacking.

The advantages of being able to tune different properties of dendrimers by alteration of different parts of their underlying structure is shown to be a unique advantage in the device physics of organic materials. This is in agreement with the literature and this work has been submitted for publication [118].

Chapter 5

Overall conclusions and their relation to future experimentation

This work has considered the simulation of excitonic solar cells and OLEDs using the Finite Element Method. To the authors' knowledge, this is the first such study of these devices using this modelling technique. A recurring theme throughout this work has been the effect of electric fields on device behaviour. In part I, the inability of a field-free model to accurately describe diffusion-limited photovoltage rise times has been, in part, attributed to the lack of consideration of the bandstructure at the TiO_2/substrate interface. It has also been shown that high doping densities could improve device performance by, firstly, reducing recombination by keeping electrons away from the grain surfaces, and secondly by the formation of a back surface field at the counter electrode. The author is unaware of any experimental studies where the device performance of a DSSC has been examined in terms of the TiO_2 doping density. This would be a fruitful avenue of further study in this field, as well as the examination of the bandstructure and electric field at the extracting electrode in such devices. The amount of band bending in the grains has been shown to increase with their radius and therefore, studies of the effect of grain size on device performance would also be instructive.

Part II was concerned with purely organic-based solar cells and LEDs. The study of ideal morphology polymer solar cells has quantified the effect of polaron pairs for the first time, showing that they can lead to significant losses in the open circuit voltage, the fill factor and the efficiency at maximum power point. Therefore, any processes

which aid their dissociation into free charges would be beneficial to device performance. Again it is the electric field which plays the most significant rôle here since it has been shown that the reduction of its magnitude at open circuit by space charge effects can increase the open circuit voltage if the finger length is long enough. Therefore, future experimental studies should consider the measurement of the electric field in these devices and the effect of the amount of interpenetration between the donor and acceptor phases with a view to the observation of field screening. A very interesting parameter to vary in experiment would be the dielectric constant. The polaron pair dissociation rate increases with this quantity for positive electric fields, which occur at open circuit in this model. Additionally, the recombination rate is inversely proportional to it. The increase of the dielectric constant may therefore act as a positive feedback loop at open circuit whereby reduction of interfacial recombination is accompanied by an increase in polaron pair dissociation. This effect should be particularly marked in devices where inorganic acceptor materials are used since their dielectric constants tend to be higher compared to prototypical organic polymers and dendrimers.

There are two main conclusions of the research into dendrimer-based OLEDs. The first is that the Mott-Schottky model for the height of the injection barrier into OLEDs is not adhered to in devices which are prepared, at least partly, under ambient conditions. The second is that Au is consistently deleterious to device performance as a hole injection and extraction material. These conclusions lead to two potentially very important corollaries. Firstly, that it is not crucial which material is chosen for the injection of charges into devices which are not entirely prepared under vacuum. This is because the effective electrode work function is found to be highly invariant. Secondly, that Au should be avoided as a hole injection and extraction material altogether in devices prepared in this way. It is generally accepted that interfaces between metallic electrodes and conjugated organic materials should be barrierless, that is, ohmic, in order for device performance to be optimised. However, it has been shown conclusively, in agreement with the recent literature, that the Mott-Schottky model cannot be used to predict which materials will form ohmic contacts in these devices. This may enable the use of more cost-effective electrode materials to be used in these applications since the use of a potentially more expensive metal to achieve ohmic injection will ultimately not lead to better injection properties. This is because of the invariance of the injection barrier upon alteration of the injecting contact material. The rôle of electric fields has been found to be small in the bipolar devices considered herein. This has been found from simulations which do not take the possible existence of an extraction barrier into account however. Barriers of this kind have been shown to have a significant effect on device performance in the literature. The results presented here have shown that there may be a barrier of this kind at some counter electrodes and so future experimental studies should examine the space charge effects present in such devices. This work could be accompanied by related simulations to those considered here with the

presence of an extraction barrier explicitly included.

Appendix A

Derivation of field dependent behaviour of metal-organic currents

Equations 3.16 and 3.19 are now derived [63] using the nomenclature in reference [80]. Near a metal-organic interface the total potential, ψ, is described by,

$$\psi = \phi_{Bn} - Ex - \frac{e^2}{16\pi\epsilon x}, \tag{A.1}$$

from equation 3.9, where $\epsilon = \epsilon_0\epsilon_r$. The maximum of the potential is obtained from the null differential, where $x = x_{ME}$,

$$\frac{\partial\psi}{\partial x} = -eE + \frac{e^2}{16\pi\epsilon x^2} = 0, \tag{A.2}$$

so

$$x_{ME} = \sqrt{\frac{e}{16\pi\epsilon E}}. \tag{A.3}$$

Therefore

$$\psi\left(x_{ME}\right)=\phi_{Bn}-eE\sqrt{\frac{e}{16\pi\epsilon E}}-\frac{e^2}{16\pi\epsilon}\sqrt{\frac{16\pi\epsilon E}{e}}=\phi_{Bn}-\frac{2e^{3/2}E^{1/2}}{\left(16\pi\epsilon\right)^{1/2}}. \tag{A.4}$$

The potential at x_c is

$$\psi\left(x_c^{\pm}\right)=\psi\left(x_{ME}\right)-k_BT, \tag{A.5}$$

therefore

$$\phi_{Bn}-eEx_c-\frac{e^2}{16\pi\epsilon x_c}=\phi_{Bn}-\frac{2e^{3/2}E^{1/2}}{\left(16\pi\epsilon\right)^{1/2}}-k_BT, \tag{A.6}$$

and

$$eEx_c^2=\left(\frac{2e^{3/2}E^{1/2}}{\left(16\pi\epsilon\right)^{1/2}}+k_BT\right)x_c=\frac{e^2}{16\pi\epsilon}=0. \tag{A.7}$$

Now, since $\frac{e^2}{16\pi\epsilon}=\frac{r_ck_BT}{4}$,

$$eEx_c^2-\left(\left(r_ck_BTe\right)^{1/2}+k_BT\right)x_c+\frac{r_ck_BT}{4}=0. \tag{A.8}$$

Multiplying the first term in equation A.8 by $\frac{r_c^2k_BT}{r_c^2k_BT}$ and the second term by $\frac{r_c}{r_c}$ gives

$$\left(\frac{eEr_c}{k_BT}\right)\left(\frac{x_c}{r_c}\right)^2r_ck_BT-\left(\left(\frac{eEr_c}{k_BT}\right)^{1/2}r_ck_BT+r_ck_BT\right)\frac{x_c}{r_c}+\frac{r_ck_BT}{4}=0. \tag{A.9}$$

Using the reduced field, $f=\frac{eEr_c}{k_BT}$,

$$f\left(\frac{x_c}{r_c}\right)^2-\left(f^{1/2}+1\right)\frac{x_c}{r_c}+\frac{1}{4}=0. \tag{A.10}$$

Therefore

$$\frac{x_c^{\pm}}{r_c} = \frac{1}{2f}\left\{\left(1+f^{1/2}\right) \pm \sqrt{\left(1+f^{1/2}\right)^2 - f}\right\} = \frac{1}{2}\left\{f^{1/2} + f^{-1} - f^{-1}\left(1+2f^{1/2}\right).\right\} \tag{A.11}$$

Now using to the definition of the recombination velocity in reference [80],

$$\begin{aligned}
S(E) &= \frac{J_{rec}(E)}{ne} = \mu E_{tot} = \mu\left(-E + \frac{e}{16\pi\epsilon x_c^2}\right) && \text{(A.12)}\\
&= \left(\mu\left[\frac{16\pi\epsilon\left(k_BT\right)^2}{e^3}\right]\right)\frac{er_ck_BT}{4}\frac{1}{\left(k_BT\right)^2}\left(-E + \left(\frac{r_ck_BT}{4e}\right)\frac{1}{x_c}^2\right) && \text{(A.13)}\\
&= S(0)\left[\frac{-eEr_c}{4k_BT} + \frac{r_c}{4}\frac{k_BTe}{\left(k_BT\right)^2}\frac{r_c\left(k_BT\right)}{4ex_c^2}\right] && \text{(A.14)}\\
&= \left[\frac{-f}{4} + \frac{1}{16}\left(\frac{r_c}{x_c}\right)^2\right] && \text{(A.15)}\\
&= S(0)\left\{\frac{-f}{4} + \frac{1}{\frac{16}{4}\left[f^{-1/2} + f^{-1} - f^{-1}\left(1+2f^{1/2}\right)^{1/2}\right]^2}\right\} && \text{(A.16)}\\
&= \frac{S(0)}{4}\left\{-f + \frac{1}{\psi(f)^2}\right\}. && \text{(A.17)}
\end{aligned}$$

The final two identities yield equations 3.16 and 3.19, which are equations (7) and (9) in reference [80].

Appendix B

The finite element method

Throughout this work, the finite element method is used to solve systems of partial differential equations. This Appendix gives a brief introduction to the method.

B.1 Introduction

Methods of discretisation of continuum equations grew up around the turn of the last century with mathematicians and engineers approaching the problem from different angles [140]. Mathematicians were interested in solutions to fundamental problems in differential, finite difference equations. Engineers on the other hand, were concerned with solutions to real world problems where the situation of interest was made of actual discrete parts, such as trusses [141].

A basic definition of the finite element method (FEM) is,

> "The finite element method is a numerical technique that gives approximate solutions to differential equations that model problems arising in physics and engineering [142]."

This method has only existed in its current mathematical form since the 1950s and one of its first applications was in the field of aircraft design [142]. Since then it has become one of the widely used numerical techniques in structural engineering. FEM remains a relatively unknown discipline outside of the engineering sciences however.

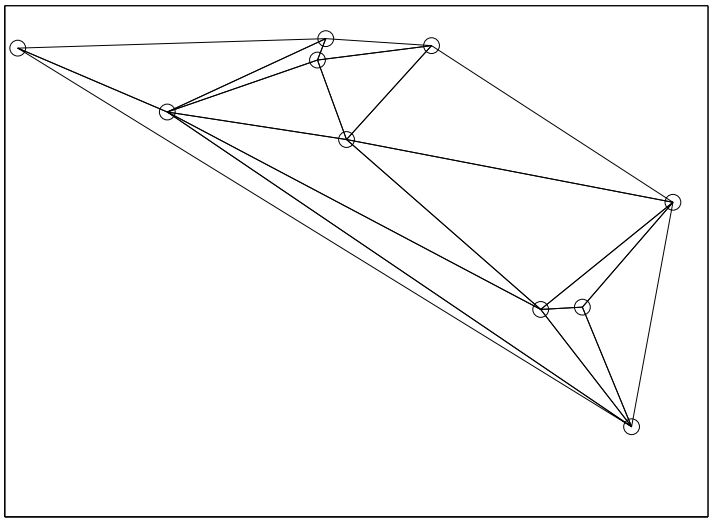

Figure B.1: An example Delaunay mesh, generated using MATLAB

The first step in performing an FEM simulation is setting up the mesh upon which to solve the equations. The simulation method used here uses an algorithm based on Delaunay triangulation. Given an arbitrary set of vertices on a 2D plane, a Delaunay mesh is one where the circle through the vertices of an element does not contain any other vertices [143]. Figure B.1 shows a generic example using the

```
delaunay
```

command in MATLAB. Throughout the Appendices in this work, any text written in the above font surrounded by spacing above and below signifies that it is computer code.

After the specification of the mesh, it is now possible to look at how the finite element method yields approximations to the underlying equations. The basic premise is to be able to approximate the actual solution, u say, by a combination of a finite number of parameters: the degrees of freedom. Consider an example consisting of just two mesh elements joined by three points or nodes [144]. The two intervals exist over $0 < x < 1$ and $1 < x < 2$ respectively and that the function u is linearly varying between the nodes. This latter assumption corresponds to so-called linear elements. In this example, all that is needed to completely define the solution are the values of the function at the nodes x_1, x_2 and x_3. Using the notation $u(x = x_1 = 0) = U(0)$, the degrees of freedom are U_i,

$$u(x) = U_1\phi_1(x) + U_2\phi_2(x) + U_3\phi_3(x) = \sum_i U_i\phi_i. \tag{B.1}$$

In equation B.1, ϕ_i have the property that they are equal to unity at node i and zero at all other nodes. They are known as basis functions and higher order polynomials can be used to interpolate between the nodes to achieve higher accuracy. Consider quadratic, second order, functions for example. In this case, two more nodes at the midpoints of the previous three are required, $x_4 = 0.5, x_5 = 1.5$,

$$u(x) = U_1\phi_1(x) + U_2\phi_2(x) + U_3\phi_3(x) + U_4\phi_4(x) + U_5\phi_5(x). \tag{B.2}$$

The function $u(x)$ between point 1 and 2, say, is defined by the degrees of freedom at the end points (1 and 2) *and* at the midpoint (point 4). In the general, N-dimensional space, the basis functions are known as shape functions and they will be referred to as such in the remainder of this work. Once the equations have been discretised in the manner described above, the Galerkin method is used to solve the problem.

B.2 The Galerkin Method

In this section, the example given in chapter 2 of reference [142] is considered to illustrate the assumptions implicit in the Galerkin method. As a generic example, consider equation B.3 below for the conduction of heat as a function of x in a medium with thermal conductivity κ, absolute temperature T and a rate of heat generation Q,

$$-\kappa\frac{\mathrm{d}^2T}{\mathrm{d}x^2} = Q. \tag{B.3}$$

This can be discretised as set out above to give,

$$T(x) = \sum_{i=1}^{n+1} a_i\phi_i(x), \tag{B.4}$$

where the ϕ_i are the shape functions. Since equation B.4 is an approximation, it will never yield the exact solution to a problem with a finite number of terms. Mathematically, if the actual solution is T^* and the approximate solution as T, then

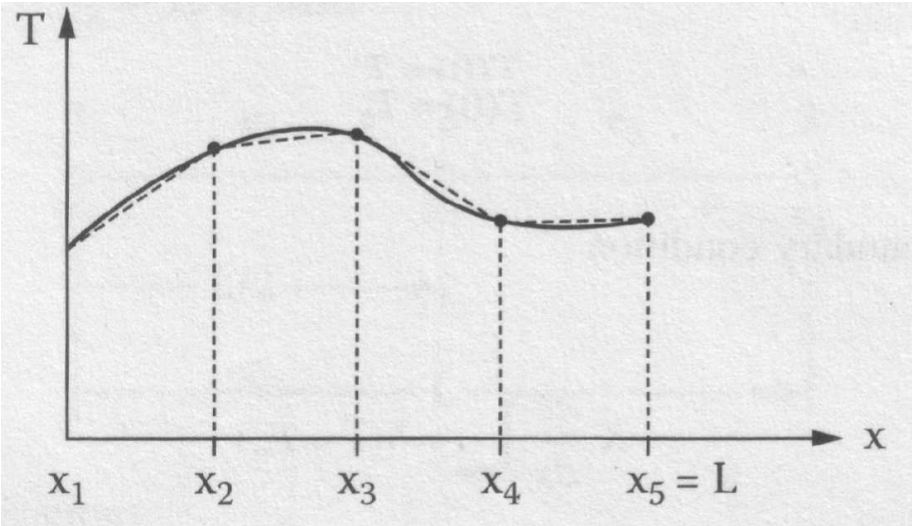

Figure B.2: Example linear interpolation function for an arbitrary temperature profile T as function of x. From [142]

$$\kappa \frac{\mathrm{d}^2 T}{\mathrm{d}x^2} + Q \neq 0 \equiv R(T, x), \tag{B.5}$$

where $R(T, x)$ is a *residual* function with the property $R(T^*, x) \equiv 0$. It is impossible to force the residual to be equal to zero everywhere. It is therefore assumed that the residual can be multiplied by a *weighting function*, $W(x)$, and the integral of the product set to zero,

$$\int_0^L W(x) R(T, x) dx = 0. \tag{B.6}$$

The Galerkin method is therefore also known as the method of weighted residuals. The choice of weighting function depends on the technique used. In the Galerkin method, they are chosen to be equal to the shape functions, ϕ_i. So, in summary,

$$\int_0^L W(x) R(T, x) dx = \int_0^L \phi(x) \left\{ -\kappa \frac{\mathrm{d}^2 T}{\mathrm{d}x^2} - Q \right\} dx = 0. \tag{B.7}$$

The problem is now one of finding appropriate forms for the ϕ_i. $T(x)$ must be continuous, so the obvious first guess is linear interpolation between nodes of the simulation domain as shown in figure B.2. It becomes clear however upon examination of the governing equation that this method will not yield physically realistic results without some modification.

In the integral form of the Galerkin weighted residuals method, it is assumed that the resulting integrals are integrable [140]. It is therefore necessary to only use integrals which have finite solutions. Consider figure B.2. It is clear that at the nodes between the elements, the first derivative of the linear fit is discontinuous and the second derivative is undefined. However, the *integral* of the first derivative is integrable. This Ansatz gives the trivial result that $\frac{\mathrm{d}^2T}{\mathrm{d}x^2} = 0$ everywhere, which is unsatisfactory. In the general case, it is clear that for equations containing derivatives of the form $\frac{\mathrm{d}^n}{\mathrm{d}x^n}$, the derivative $\frac{\mathrm{d}^{n-1}}{\mathrm{d}x^{n-1}}$ must be continuous. Often, integration by parts can be used to lower the derivative order by one since, in general

$$\int udv = uv - \int vdu. \tag{B.8}$$

Now the continuity is only required in $\frac{\mathrm{d}^{n-2}}{\mathrm{d}x^{n-2}}$. It should be noted here that the above mentioned integration by parts is simply an implementation of the divergence theorem [145],

$$\int\int\int_V \nabla \cdot \mathbf{F} dV = \int\int_S \mathbf{F} \cdot \mathbf{dS}, \tag{B.9}$$

where the divergence of a vector field, $\mathbf{F}$, within a bounded volume, $\mathbf{V}$ is evaluated by considering the normal flux, $\mathbf{F}\cdot\mathbf{dS}$ over the surface, $\mathbf{S}$ of the volume [145, 141]. Equation B.9 is the three-dimensional case of the theorem but is equally valid in n-dimensions.

Furthermore, applying the condition that $\frac{\mathrm{d}^2T}{\mathrm{d}x^2}$ must exist everywhere is incompatible with another analytically soluble situation of interest, such as equation B.10,

$$-\kappa\frac{\mathrm{d}^2T}{\mathrm{d}x^2} = \delta(x - x_{source}). \tag{B.10}$$

Here $\delta(x - x_{source})$ is the Dirac delta function, which has the property of being equal to unity when $x = x_{source}$ and zero otherwise. It also has an infinite first derivative. This can be resolved by using integration by parts. From equation B.7,

$$\int_0^L \phi\frac{\mathrm{d}^2T}{\mathrm{d}x^2}dx = \phi\frac{\mathrm{d}T}{\mathrm{d}x}\bigg|_0^L - \int_0^L \frac{\mathrm{d}\phi}{\mathrm{d}x}\frac{dT}{dx}dx, \tag{B.11}$$

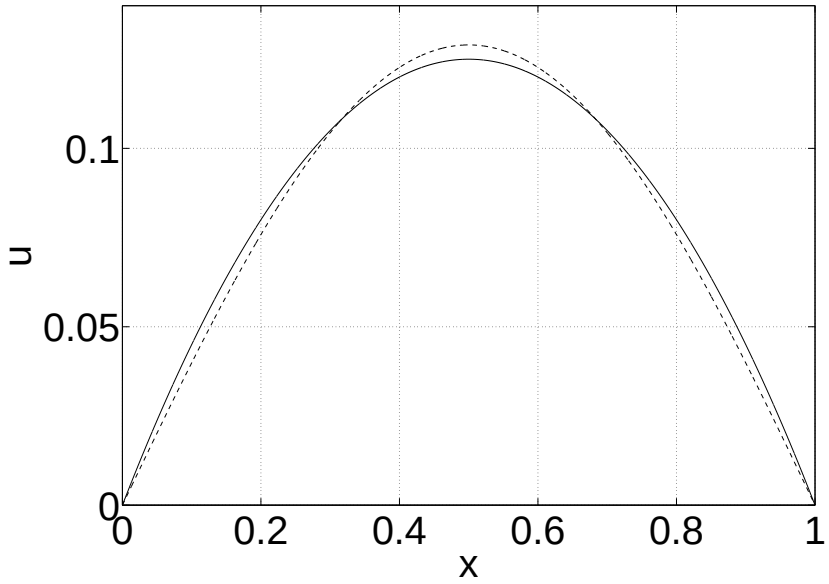

Figure B.3: Comparison between the analytical (solid line) and finite element (dashed line) solutions to equation B.13.

and therefore

$$\int_0^L \kappa \frac{\mathrm{d}\phi}{\mathrm{d}x}\frac{\mathrm{d}T}{\mathrm{d}x}dx - \int_0^L \phi Q dx - \kappa\phi\frac{\mathrm{d}T}{\mathrm{d}x}\bigg|_0^L = 0. \tag{B.12}$$

Equation B.12 is very important and is known as the *weak* form of equation B.7; the highest derivate has been lowered, or weakened by one.

A beautifully simple example of the implementation of this method can be seen by consideration of equation B.13 over the interval between zero and one, with the boundary conditions $J(0) = J(1) = 0$.

$$-\frac{\mathrm{d}^2 J}{\mathrm{d}x^2} = 1. \tag{B.13}$$

Trying a solution, $J(x) = a_1 \sin \pi x$, the Galerkin form of equation B.13 is

$$\int_0^1 \sin \pi x \left(-\frac{\mathrm{d}^2}{\mathrm{d}x^2} \left[a_1 \sin \pi \right] x - 1 \right) dx = 0. \tag{B.14}$$

Splitting the integral into its constituent terms and integrating the first term by parts gives the weak form,

$$
\begin{aligned}
& -\sin \pi x \frac{\mathrm{d}}{\mathrm{d}x} \sin \pi x \,|_0^1 + \int_0^1 \left(\frac{\mathrm{d}}{\mathrm{d}x} a_1 \sin \pi x \right)^2 dx - \int_0^1 \sin \pi x dx && \text{(B.15)} \\
= \; & 0 + \int_0^1 a_1 \pi^2 \cos^2 \pi x dx - \int_0^1 \sin \pi x dx && \text{(B.16)} \\
= \; & \frac{a_1 \pi^2}{2} - \frac{2}{\pi} && \text{(B.17)} \\
= \; & 0. && \text{(B.18)}
\end{aligned}
$$

Therefore $a_1 = \frac{4}{\pi^3}$. A comparison between the analytical and finite element solutions to the problem can be found in figure B.3 and illustrates the power and underlying simplicity of the Finite Element Method.

Appendix C

COMSOL Multiphysics Manual

COMSOL is commercially available and it is the aim of this section of the thesis to act as a 'manual' for solving electrical problems in the systems considered herein. For ease of reading, when a term specific to **COMSOL** is used, it will be printed in **bold** font. Begin by typing

```
comsol &
```

at a command line, followed by

```
ps aux | grep comsol | grep -v flexlm |grep -v grep |
```

```
awk '{print $2}' |  xargs renice +10
```

which increases the stability of the simulations by increasing the value of the Unix 'nice' parameter. The Model Navigator now appears on screen, figure C.1.

In creating a new model, the dimension of the problem must be chosen, 1-3. In addition, radially symmetric problems can be considered. The **Application Modes** from the given list are then chosen; for example **COMSOL Multiphysics → Convection and Diffusion → Convection and Diffusion → Steady-state analysis** for dealing with time independent charge distributions where electric fields and diffusion gradients affect the transport. An arbitrary name for variable to be solved for is then chosen.

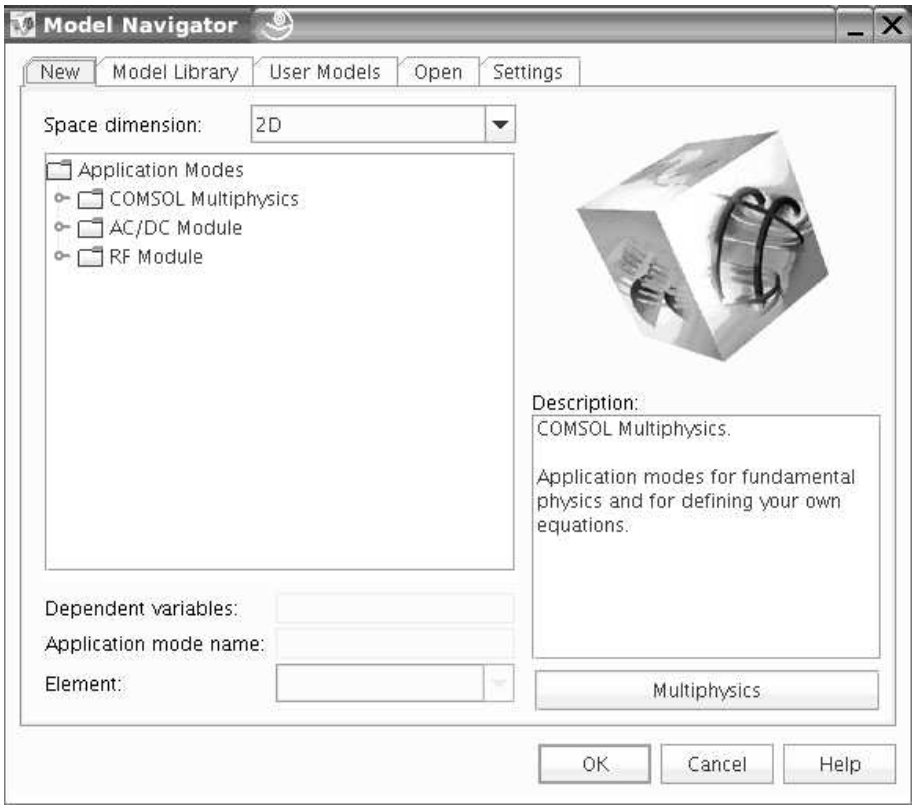

Figure C.1: The COMSOL Multiphysics Model Navigator

One of the main selling points of the COMSOL software is its ability to deal with so-called **Multiphysics** simulations; that is, interacting equations which can be coupled together. An example of this is the coupling between charge density and electric potential, i.e., the gradient of the electric field is proportional to the charge density, but the flux of charges is dependent on the electric field. By clicking on the Multiphysics button on the lower right hand side of the Model Navigator as many different **Application Modes** as desired can be chosen. The term **Application Mode** refers to the solution of each dependent variable.

For some of the **Application Modes**, the default **Application mode properties** must be altered. For example, for **Convection-Diffusion** the **Equation Form** must be changed to **Conservative** from **Non-Conservative**. Also, this is where the **Weak Constraints** are activated or de-activated. These are important for calculation of the flux of particles and can only be used in conjunction with Dirichlet boundary conditions.

Pressing OK opens the main **COMSOL** window. There are many different expressions, fields, constraints and couplings which can be filled in here but only relatively few will be explored here. The alteration of the explicit equation system which is solved is possible (that is, the actual underlying form of the equations themselves), however this is not encountered in this work. The **CAD** interface of the software is used to generate

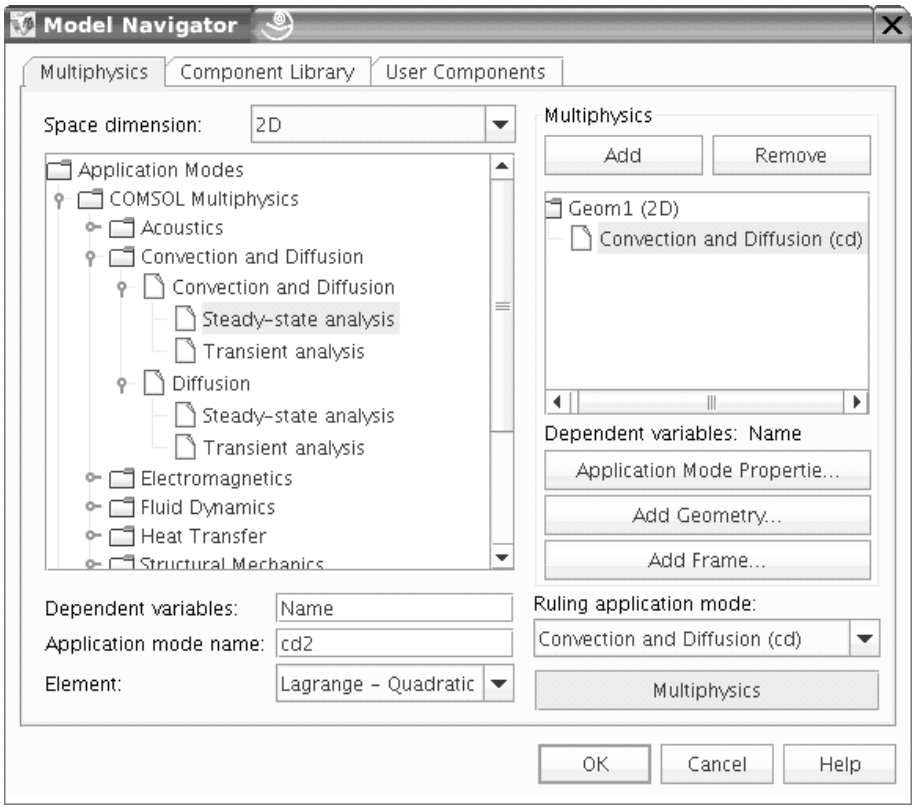

Figure C.2: Choosing Multiphysics application modes.

the simulation subdomain which is to be simulated and this should be the first task undertaken in *any* simulation. The **Draw** mode is accessed by clicking on **Draw** → **Draw Mode**, which gives a default grid of extent -1 → 1. However, the domains of interest here are of sizes in the range nm to μm so this must be reduced. This is done by going to **Options** → **Axes/Grid Settings**. Here the extent of the modelling domain and the grid settings can be altered. To draw the shape of interest, click on the relevant shape on the far left hand side of the window and click-and-drag with the mouse. Fine tuning of the size and position of the selected shape can be achieved by clicking on **Draw** → **Object Properties**. This is shown in figure C.3. To draw an arbitrary shaped polygon using straight lines, first select the **Line** option from the drawing bar and click on the grid points to define the desired shape. The shape is complete by right-clicking at the final desired vertex. If the initial and final points are not coincident then **COMSOL** will connect them with another line.

After the drawing of the relevant figures it is necessary to set up the equation system. Constants are set by clicking on **Options** → **Constants**. Position dependent quantities or those which are only valid on boundaries, or on certain subdomains must also be specified. These are specified in **Options** → **Expressions** → **Boundary Expressions** or **Subdomain Expressions**. The treatment of each variable is done using the name given in the model navigator and derivatives are specified using the simple syntax for the

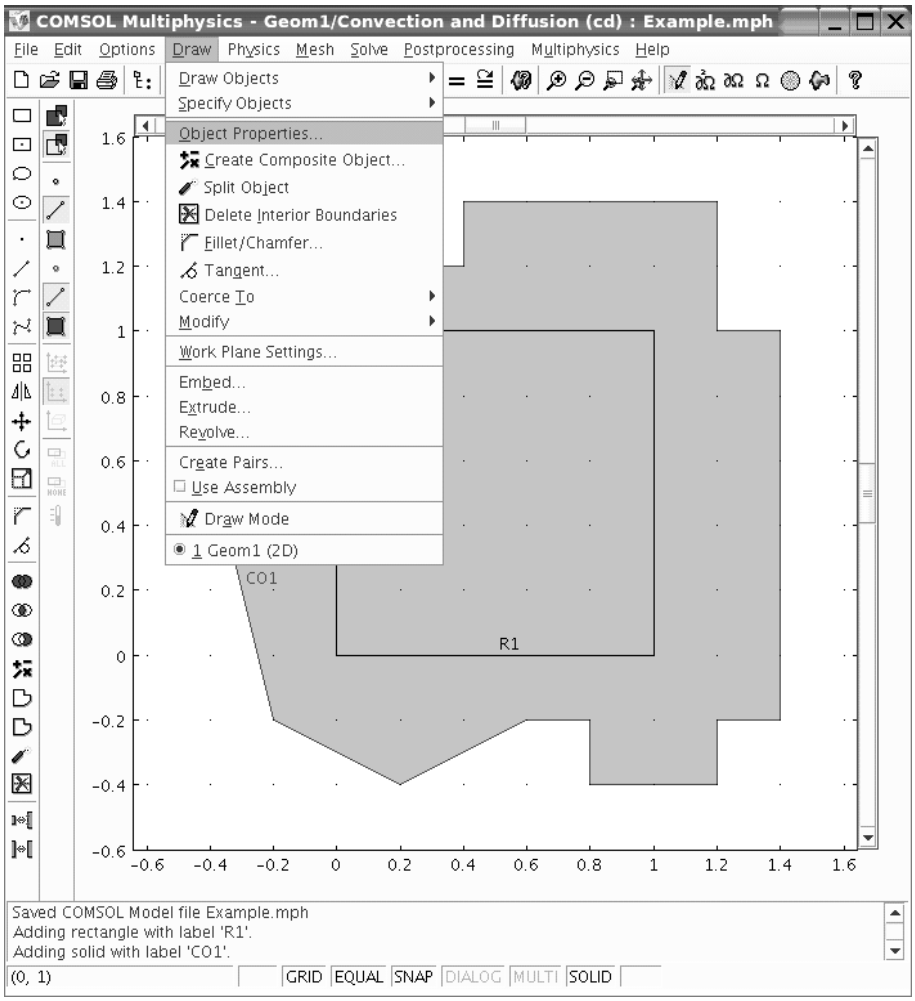

Figure C.3: Example of a rectangle drawn inside an arbitrary shaped polygon drawn with straight lines. The **Object Properties** option is shown from the **Draw** menu from where the dimension, geometrical origin and rotational orientation can be specified.

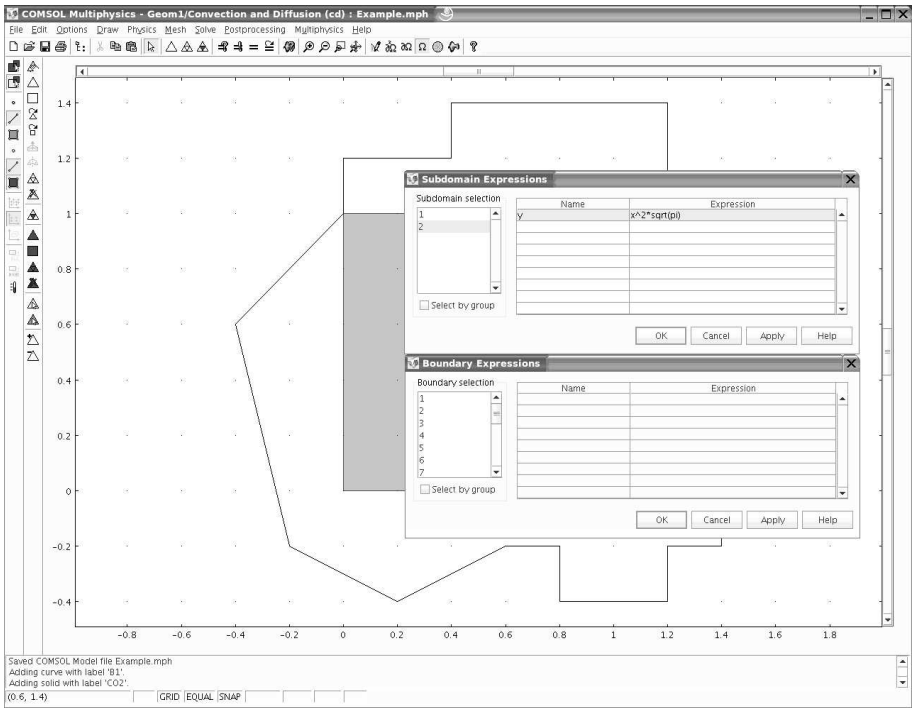

Figure C.4: Example of the Boundary Expressions and Subdomain Settings dialogue boxes. Clicking between the two boxes changes the view mode. This can be done manually using the Ω and $\partial\Omega$ buttons on the top of the window for Subdomains and boundaries respectively.

generic variable $J(x, y, z, t)$. An example of the Boundary and Subdomain Expressions dialogue boxes are shown in figure C.4

`Jx, Jy, Jz, Jxy, Jt, Jtt...`

where these quantities represent $\frac{\partial J}{\partial x}$, $\frac{\partial J}{\partial y}$, $\frac{\partial J}{\partial z}$, $\frac{\partial^2 J}{\partial x \partial y}$, $\frac{\partial J}{\partial t}$ and $\frac{\partial^2 J}{\partial t^2}$.

This description of the general mathematical language used by **COMSOL** is now explored further using the **Convection-Diffusion** solver as an example. Fundamentally, all **COMSOL** requires as an input is for the user to enter parameters and/or expressions in the fields **Physics** $\rightarrow$ **Boundary Settings**, and **Physics** $\rightarrow$ **Subdomain Settings**, as in figure C.5.

Specifically, all the solver needs to know for calculation of the bulk transport properties is the diffusion coefficient and the speed of 'convection'. In semiconductor device physics, this is almost always called the drift velocity. One can either enter the desired expression directly into the dialogue box or use the name of an expression given in the **Subdomain Expressions** box, for example. In the case of the **Diffusion Coefficient**, D and **velocity** (in one dimension),

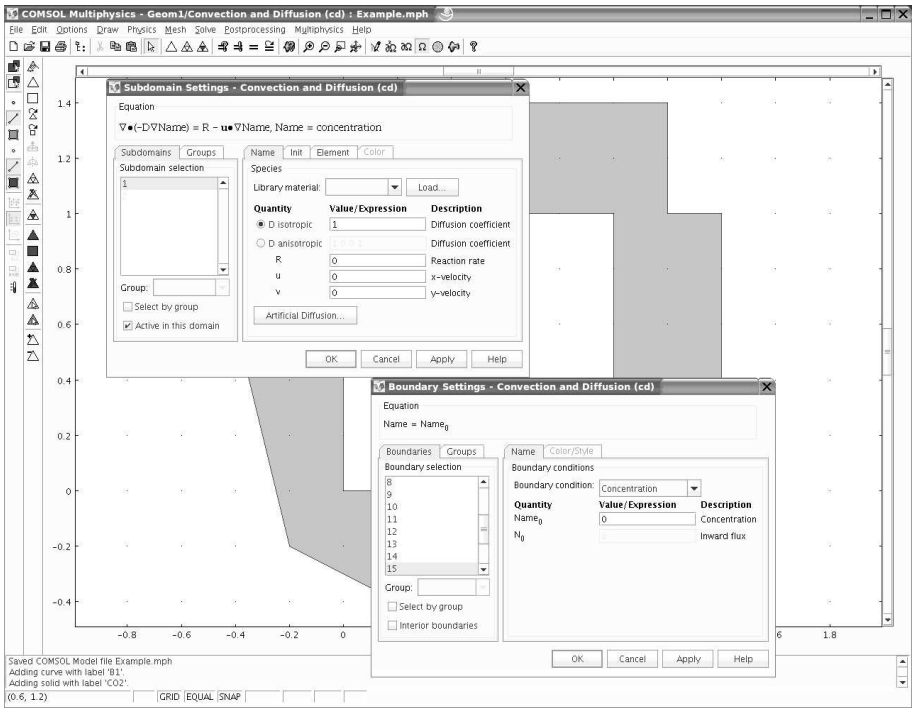

Figure C.5: Example of the **Boundary Expressions** and **Subdomain Settings** dialogue boxes.

```
D=kT/e*mu
```

using the Einstein relation (k, T, mu and e are Boltzmann's constant, the temperature, the mobility and the electronic charge respectively) and

```
velocity=-mu*psix or mun*E
```

the alternative expression can only be used once 'E' has been defined in the **Subdomain Expressions** dialogue for example,

```
E=-psix
```

The **Reaction Rate** box in the **Subdomain Expressions** dialogue needs more careful consideration; this is where the form of the charge generation and/or recombination profile is specified. Because of the way **COMSOL** expects input, generation terms *must* be positive and recombination terms *must* be negative. The solution is for the density of charge carriers, not the charge density, so it is crucial that the **Reaction Rates** have the units of inverse metres cubed, velocities have units of metres per second,

and diffusion coefficients units of metres squared per second. The units are however arbitrary in a generic model as long as they are internally consistent. Other unit systems can be specified in the **Physics → Model Settings → Base Unit System** field, although 'None' is used throughout this work and SI units are used internally throughout. All that is left to specify in the Convection-Diffusion **Subdomain Settings** is the **Initial Condition** tab. This is the initial guess of the solution at the beginning of the simulation. It should be mentioned at this point that for modelling pure diffusion (as used for modelling exciton transport) the method of setup is the same but one does not need to specify a drift velocity. The **Convection-Diffusion** solver could be used instead with zero drift velocity. The **Element** tab in the **Subdomain Settings** box should be left unchanged.

A very important aspect of the **Subdomain Settings** box is the **Active in this domain** check box. This determines whether or not the solver gives a solution in a particular subdomain. This is crucial for the consideration of **Internal Boundary Conditions**. Consider the geometry in figure C.3, if the interior rectangle is considered active then boundary conditions on its edges cannot be specified *unless* the **Interior boundaries** check box is ticked in the **Boundary Settings** dialogue.

The **Boundary Settings** dialogue for the **Convection-Diffusion** solver is now considered. There are essentially two types of boundary condition which are considered here; Dirichlet and Neumann. In the former, the flux of carriers is specified, which corresponds to a Schottky boundary condition. In the latter case the density is specified, which is an Ohmic condition. In the case of flux boundary conditions it is again very important to notice that since the solution is for the number density of electrons we need to give the flux (current) in the units of inverse metres squared per second. This corresponds to a flux density; specifying a current density would give a flux which is 1.6×10^{-19} (the electronic charge) times too small. Generally, any parameters to be used in the **Boundary Settings** dialogue are specified in the **Boundary Expressions** field.

The Poisson equation solver is now considered. This is included in the **Multiphysics** form by selecting **COMSOL Multiphysics → PDE Modes → Classical PDEs → Poisson's Equation** in the **Model Navigator**. In the **Subdomain Settings** dialogue the Poisson equation is given in the following form,

$$\nabla \cdot (c\nabla \mathrm{psi}) = \mathrm{f}, \tag{C.1}$$

where f is the 'source term'. This is in comparison to the standard electrostatic form,

$$-\nabla^2\psi = \frac{e\rho}{\epsilon_0\epsilon_r} = \frac{e\,(p-n)}{\epsilon_0\epsilon_r}, \tag{C.2}$$

where ρ is the total charge density.

The parameter c in equation C.1 is called the **Diffusion Coefficient** in the **COMSOL** nomenclature and enables the user to specify anisotropic diffusion (this is also possible in the **Convection-Diffusion**, and **Diffusion application** modes). This **Diffusion Coefficient** is set equal to ϵ_r (isotropic diffusion) in this work and the source term, f, is specified as

$$f = \frac{e\,(p-n)}{\epsilon_0}. \tag{C.3}$$

This enables the recovery of the standard electrostatic form, equation C.2 from equation C.1. Since ϵ_r is a constant the **Diffusion Coefficient** could be set equal to unity and replace ϵ_0 with $\epsilon_0\epsilon_r$ in equation C.3 without any loss of generality, assuming isotropic diffusion.

This invokes an interesting property of **COMSOL**; that is, the same equation can be solved in several different ways. As long as the solver used is set up to deal with the Subdomain and Boundary Expressions the user wishes to use, then a solution can proceed. An interesting example of this was found when dealing with interacting populations of conduction band and trapped electrons in the modelling of dye-sensitised solar cells, as will be described later in this Appendix. The boundary conditions for the Poisson equation are of the Dirichlet form and the potential at the electrodes is equal to the barrier to electron injection from the metal work function into the semiconductor LUMO level.

In a simulation with multiple subdomains (boundaries), navigating between them to ascribe different properties is achieved either by clicking with the mouse or by selecting from the numbered list on the left hand side of the **Boundary Settings/Expressions** dialogue. Any parameter specified on a subdomain (boundary), **1** say, will only be valid on that one subdomain (boundary) unless multiple subdomains (boundaries) are selected when typing the relevant expression. Expressions entered in the **Options** → **Expressions** → **Scalar Expressions dialogue**, however, are universally recognised and can be considered 'global' variables.

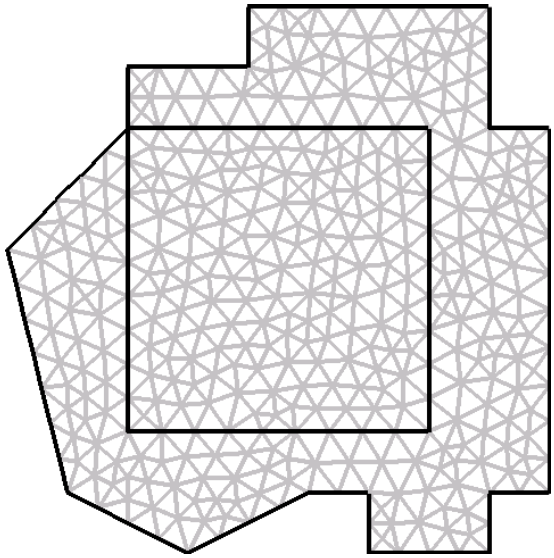

Figure C.6: The default mesh for the geometry in figures C.3-C.5.

The meshing used in this modelling is straightforwardly implemented by pressing **Initialize Mesh** button or from the **Mesh** menu. Considering the geometry in figures C.3-C.5, the default mesh is shown in figure C.6.

Mesh→Free Mesh Parameters brings up a dialogue box enabling the definition of the size of the mesh on boundaries on subdomains. The mesh may need to be refined, for example, at material interfaces where material properties may vary strongly with position. Alternatively, the mesh can be globally refined using the **Refine Mesh** button or select from the **Mesh** menu.

The relationship between two interacting populations of electrons in a DSSC is now considered, as alluded to above. The different populations are free, conduction band electrons and those which are trapped and therefore immobile. Neglecting any recombination or so-called 'back reaction' between the electrons and the electrolyte or substrate, then it is clear that the reaction rates for the two electron densities must be equal and opposite. This is because the act of trapping one electron will remove it from the conduction band and place it in a trap. As seen earlier, the traps are distributed in energy below the conduction band in an exponential distribution such that there are more shallow traps (near conduction band) than deep traps. The coupled equations describing the conduction band (n_c) and trapped (n_t) electrons are

$$\frac{\partial n_c}{\partial t} = -\frac{\partial n_t}{\partial t} = \langle \text{detrapping} - \text{trapping} \rangle \,. \tag{C.4}$$

The precise mathematical interpretation of equation C.4 is given elsewhere as it is only the implementation in **COMSOL** that is of concern here. The point is that the amount of trapping at each trap level needs to be weighted by the appropriate number of traps at that particular level. This is important because the rate of trapping into any level is independent of its depth but the detrapping rate is dependent thereon. The triangular brackets in equation C.4 denote an integration over energy. This is to ensure that the total number of trapping states is the same as if they were all at one energy. The form of equation C.4 means that a system of integro-differential equations results, which **COMSOL** is unable to solve without modification. **COMSOL** is however capable of solving some integral equations, but only those which deal with spatial or temporal integrals [146]. The way around this is to discretise the trap levels from the continuous exponential distribution and solve for each trap level separately.

If there is just one trapping energy [58], no integration would be necessary. The trapping term will be negative (positive) in the conduction (trapped) electron application mode and the detrapping term will be positive (negative). Photogenerated electrons leave through the substrate side of the device via a flux boundary condition and the electrolyte side is insulating (zero flux). Since the trap distribution is normalised, the continuous trap distribution can be separated into N discrete levels and transform the integral into a sum, that is,

$$\int_{E_{Fneq}}^{E_C} g(E_T) dE_T \approx \sum_{i=1}^{N} g(E_T)_i \Delta E_T. \tag{C.5}$$

What this amounts to in terms of implementing the equations in **COMSOL** is that N **Application Modes** are needed to describe N trap levels of different depths. The weighting of the trap number density is achieved by firstly assuming that each and every trap level has the same number of traps as the whole system in reality, $N_{t,0}$. No weighting of the trapping-detrapping **Reaction Rates** in the N traps level application modes is considered. Each trap level reaction rate is then multiplied by the appropriate factor as described in equation C.5 and then summed to give the total trapping-detrapping **Reaction Rate** for the conduction band electron density. This gives identical results found in reference [61] obtained using a Chebyshev numerical integration scheme [63]. Another way of thinking about the total trapped electron density is that the trap occupation probability is given by the total density of trapped electrons divided by $N_{t,0}$.

The form of the equation for the trapped electron density can be described in terms of the same solver as used for the conduction band electrons but with zero diffusion coefficient. This is because the trapped electrons are immobile and hence to do not contribute to the current in the device. This reduces the continuity equation for trapped electrons to the following form,

$$\text{rate of change} = \text{reaction rate}. \tag{C.6}$$

The implementation of the optical modelling in polymer blend solar cells is now considered. Simulation of the optical interference pattern in a multilayered structure requires the use of one of the add-on modules of **COMSOL**. Until 2006, this was called the **Electromagnetics** module, but has subsequently been split in two (the **RF** module and the **AC/DC** module). The **RF** module is considered exclusively here. From the **Model Navigator** the solver is found from **RF Module** → **In-Plane Waves** → **TE Waves** → **Harmonic propagation**. For simulations of blended polymer solar cells, a device architecture similar to that of reference [84] is considered. A problem arises in the implementation of the equations because the thickness of the glass layer is orders of magnitude thicker than the rest of the device. This means that complex amplitudes cannot be summed as in the multilayer stack without the glass. Therefore transmitted *intensities* (amplitudes) must be summed instead [84, 98]. Therefore, the reflectance of the multilayer stack (not including the glass layer) is calculated as well as that due to the glass/air interface. The glass/air interface is straightforwardly calculated from the standard Fresnel relations [1]. However, the reflectance of the stack is more complicated and must be solved numerically.

The back contact on the device is assumed to be aluminium and is therefore highly reflecting. Electromagnetic radiation at the wavelength of interest, 459nm, only penetrates a very short distance into aluminium [100] so the **Impedance** boundary condition at the organic/aluminium interface is used. This boundary condition is invoked when the radiation is known to penetrate only a small distance and negates having to use a further subdomain in the modelling. The **Surface Electric Field**, E_{sz}, can be used to specify a surface current at this interface, but this is not considered here.

In practice, two optical electric field solvers are required,

1. To find the reflectance of the multilayer stack (not including the glass substrate).
2. To calculate the actual value of the optical electric field in the stack given the electric field at the glass/stack interface, calculated from the former solution.

To calculate the reflectance of the stack, every interface in the device must be considered. It is therefore necessary to have a layer with a refractive index equal to that of glass included. This layer should be thin because it is assumed that the light which is incident on the glass/stack interface is incoherent [147]. The **Port** boundary condition is then applied to the extreme left boundary, which outputs the **S-parameters** [148]. The S-parameter, S_{11} gives the power reflection coefficient $\tilde{R}$ [146],

$$\tilde{R} = |S_{11}|^2, \tag{C.7}$$

which is used in the calculation of the optical electric field at the glass/stack interface.

There are several properties of the **Port** boundary condition which require consideration. Only one **Port** is considered and so the **Wave excitation at this port** check box should be ticked. The value of the **Port power level** box is immaterial since the value of S_{11} is not dependent on the value of this power. The **User Defined** option from the **Mode Specification** drop-down list is chosen and E_{oz} is set to an arbitrary value because S_{11} is independent thereof. Finally the **Cut-off Frequency** is set to zero which implies that the waves of interest can propagate down zero frequency [146]. Since this solver can only be used in dimensions greater than one, to negate variation in the direction perpendicular to the illumination direction, the **Perfect Magnetic Conductor** boundary condition is used at the boundaries perpendicular to this direction [146].

For the **RF** module **Subdomain Settings**, all that is required is the (complex) refractive index in the form

$$\text{refractive index} = \text{real part} - \text{imaginary part} \times i, \tag{C.8}$$

where $i = \sqrt{-1}$. Note the negative sign of the imaginary part, in contrast to most texts on this subject. The refractive index is almost always wavelength dependent. So if the illumination is monochromatic, then a numerical value can be entered. However a more general case has been implemented here enabling any wavelength in a given range to be used. This is implemented using a **Function**. These can be defined in **Options** → **Functions**.

The task of these functions is to interpolate between known values of a desired quantity held in an external text file of the form given in table C.1. **COMSOL** can also interpolate from numerical data entered manually or from user defined mathematical

functions.

When the function dialogue box appears, the desired function name is entered and the interpolation option selected. If interpolating from a file of data, select **File**, from the **Use Data From** drop down menu and enter the location of the file. On the next screen choose an **Extrapolation Order** and an **Extrapolation Method**. This latter option is used when the independent variable lies outside of the given range and can be set to a constant value, an interpolation function or a specific number. To evaluate a function, the following syntax is used,

$$\text{numerical value} = \text{function name}\,(\text{value of dependent variable})\,. \tag{C.9}$$

For example, for a function named Function1, to evaluate it for its argument equal to π, the code is written

```
Function1($\pi$)
```

The optical modelling presented here uses the free space wavelength as the independent variable (Alternatively, the frequency can be specified here). These variables are automatically created in the **Physics** → **Scalar Variables** dialogue box. Note that the names given to these variables indicate to which application mode they refer to. For example, the free space wavelength will be called

```
lamda0_Example
```

A full list of these built-in variables can be found in the **COMSOL** documentation. This allows access to the many variables which the **Application Modes** solve for by default and saves the user valuable time in **Postprocessing**.

As with any modelling procedure there are certain conditions under which a simulation may not converge. There are ways to improve the convergence of a simulation. One of the most often used is to solve for a simpler case than finally needed and then use this simpler case as a starting value for the more complicated model. This can be achieved in a number of different ways. For example, if solving for multiple application modes, then solving for a smaller subset of these first will aid convergence. These settings can be changed in the **Solve** → **Solver Manager** dialogue box. In the **Initial Value** tab, different starting conditions can be specified. These will be the settings that are used if the **Solve** button is used to start the solver. This is illustrated by the '='

Line number	Contents of line
1	%
2	values of the independent variable go here separated by spaces (for example wavelength)
3	%
4	values of the dependent variable go here separated by spaces (for example the real part of the refractive index)

Table C.1: Example of an input file for defining a **Function** in COMSOL

button seen in figure C.5, for example. However, if the **Restart** button is used ('=' sign with curving arrow above), then the solver uses the current solution as the initial condition. Note that this will give the same results as if the **Current Solution** option in the **Initial Value** tab of the **Solver Manager** is checked and the **Solve** button is used. For example, in the most complex **Multiphysics** model considered in this work there are 9 **Application Modes**; 4 **Convection-Diffusion**, 2 **Diffusion**, a **Poisson's Equation** solver and two **RF** optical electric fields. First, the **Poisson's Equation** and the two **RF** modules are solved alone. Then the two **Convection-Diffusion** variables containing charge generation at the heterojunction are solved for (pertaining to majority carriers in both phases). However, the term describing the charge generation due to exciton dissociation is, at first, not included. This is done by introducing a parameter Ξ (which is initially set to zero) such that the charge continuity equation is of the form

$$\text{Reaction rate} = \Xi \times \text{generation from exciton dissociation} - \text{recombination to form excitons.} \tag{C.10}$$

After this has been solved, the remaining **Application Modes** are solved for (still for $\Xi = 0$). Only after this has converged is Ξ set to unity, which recovers the full equation system. Indeed, using the **Parametric** solver, intermediate values of Ξ could be used to aid convergence further. This has been found to be a very reliable way of obtaining solutions to complex problems where other, simpler, methods had failed.

Other conditions where COMSOL models tend to have difficulty are where there are particularly high **Reaction Rates** or abrupt, large changes in material properties, such as dielectric constant. This is particularly acute in simulations involving titanium dioxide, TiO_2 mixed with an organic material. This is because TiO_2 has a dielectric constant approximately an order of magnitude higher than that of standard conjugated polymers.

Now the solver used throughout this work is considered. The different solvers are accessed from the **solve→Solver Parameters** dialogue box. Fundamentally there are four different types of solver available; **Stationary**, **Eigenvalue**, **Time-dependent** and **Parametric**. In this work only the final two of these are considered. For both of these solution types, the same, default, **UMFPACK** solver is used. This is the **U**nsymmetric-pattern **M**ulti**F**rontal **Pack**age. This uses the matrix equation solution method known as LU decomposition for sparse matrices [144, 149]. In all the time independent modelling the **Parametric** solver is used, which enables the user to vary one parameter and keep all the results together for analysis. The parameter most

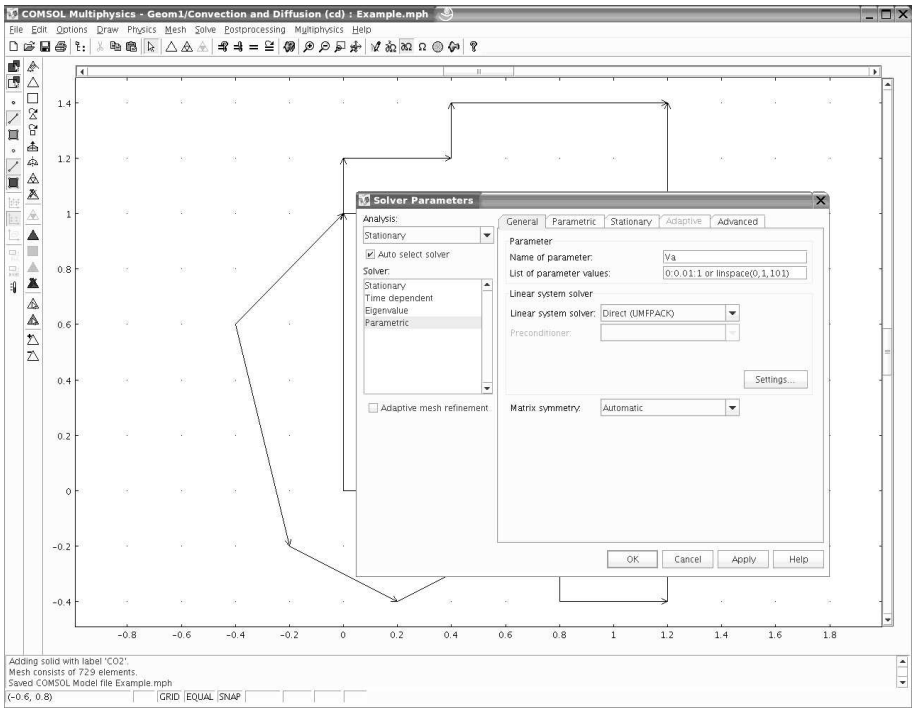

Figure C.7: The **Solver Parameters** dialogue box, showing the methods of entering desired parameter values.

often varied is the applied bias, enabling current-voltage characteristics to be obtained. Figure C.7 shows the **Solver Parameters** dialogue box.

Values of the parameter to be solved can be entered in several forms; as single numbers, as a list of number separated by commas, as vector of the form

```
starting value:stepping value:end value
```

as a vector of linearly spaced values of the form

```
linspace(starting value, end value, number of steps)
```

or as a vector of logarithmically spaced values of the form

```
logspace(log10(starting value), log10(end value), number of steps)
```

The Parametric solver uses the value of the solution 'active' in the mode as the initial guess for the solution. This solver is also an excellent way of attaining convergence on

difficult problems as illustrated above for the example of the interdigitated polymer solar cell model. Using the parametric solver, the solution could be obtained using any combination of values of Ξ from 0 to 1 as long as they increase monotonically.

For the time dependent simulations, all that is necessary is to enter the value of the time(s) to be used in the **Times** field after selecting the **Time-dependent** solver on the left hand side of the **Solver Parameters** dialogue box.

With both of these solvers, there are many other parameters which can be changed, however, it has been found time and time again that application of the correct mathematical and physical data obviates the changing of these fields and they are left at their default settings as often as possible. In the **Solver Manager** dialogue, the variables to be solved for are chosen. This is also where the initial estimate of the solution variable is specified. It is opened from the **Solver Manager** button, or from **solve→Solver Manager**. In the left hand **Initial Value** tab, The value of the initial solution is chosen. Any expressions defined elsewhere in the model can be used here, or alternatively the **Current Solution**, or a **Stored Solution** can be used.

Any solution can be stored for future use and this is useful when trying to find a particular type of solution with an unknown value of a particular parameter. For example, a very frequently used example of this used throughout this work is to find the open circuit voltage in a solar cell. This will occur at some finite positive bias, generally somewhere between 0 and 1.5V. Therefore, a step size of lower precision than finally required is used first. The solution required (that is, a change of sign of the current in the case of the V_{oc}) is found to fall between two solution parameters, $i \longleftrightarrow j$, say. Therefore either i or j can be used as the starting parameter by storing them using the **Stored Solution** option in the **Initial Value** tab. It is then *essential* to use the **solve** option *not* the **Restart** option. This is because using the **Restart** option always ignores anything in the **Initial Value** tab and just uses the current solution as the initial estimate for the solution. The next two tabs (**Solve For** and **Output**) simply denote which parameters are found from the solution and which are available for post-processing. Throughout this work the contents of these two tabs is identical. Some other miscellaneous capabilities of **COMSOL** are now explored.

Integration Coupling Variables are extremely useful in several ways. For example, to find the average value of a quantity along a boundary, a **Boundary Integration Variable** can be used. These are defined in **Options→Integration Coupling Variables→Boundary Variables**. These variables are defined in exactly the same way as normal **Boundary Expressions** except that the variable expression is now integrated along the boundary. For example, if the expression is unity, the output of the variable will be the length of the boundary in question. Therefore, to find the average of a

Name	Expression
Length	1
Jbar	**J/Length**

Table C.2: Example of an Boundary Integration Variable

quantity **J**, **Jbar**, the formalism in table C.2 is used.

Whenever the variable **Jbar** is called in the simulation, it will return the average value of the variable **J** along the boundary of interest. Note that this can be applied across as many *connected* edges as required. Construction of the **Subdomain Integration Variables** is handled in a completely analogous way.

Extrusion Coupling Variables are a way of accessing the value of a variable at a point removed from where the quantity is defined. An example of this is in the consideration of a bilayer organic solar cell, as considered in reference [55]. In this example, the **Reaction Rate** of free charges within a finite distance of the interface depends on the charge densities and electric field at the junction. Mathematically, this means the evaluation of a Dirac-delta function outside where it is defined. This requires the use of a **Boundary Extrusion Variable**. These are accessed via **Options→ Extrusion Coupling Variable→ Boundary Variables**. Again, they are formulated in the same way as the standard **Boundary Expressions** but this time with some additional information denoting *where* the variable is to be accessed. This amounts to choosing whether there is a **Linear Transformation** or a **General Transformation**. A linear transformation is used for mapping between regions of the same spatial order, line to line for example. In the **Source** tab the variable name and its mathematical form are defined and the **Linear Transformation** option is selected. Next, on the **Destination** tab, the line where the variable is required to be accessed is chosen, checking the **Use selected boundaries as destination** check box. In the **Source Vertices** tab, the ends of the source line are chosen, and they are moved into the **Source Vertices** list using the arrows. Finally the **Destination Vertices** are added*in the same order* as the **Source Vertices** [144]. In the case of a **General Transformation**, extrusion to other dimensions is possible, and this is exactly what is necessary in the case considered in reference [55], where extrusion from a vertex to a subdomain is required. Opening the **Options→ Extrusion Coupling Variable→ Point Variables** dialogue box, the variable to extrude is selected and the **General Transformation** option at the bottom is checked. On the **Destination** tab, the variable can be made available at another point, at a boundary, or on a subdomain from the **Level** drop down menu by checking the appropriate box on the left hand side menu.

Application Mode	Natural Boundary Condition
Convection-Diffusion	Insulation/Symmetry
Electrostatics	Zero Charge/Symmetry
Poisson's Equation	Neumann Boundary Condition with null coefficients

Table C.3: Examples of Natural Boundary Conditions [146]

Periodic Boundary Conditions are a particular implementation of the extrusion coupling variable considered in the previous section and are accessed via **Physics**→ **Periodic Conditions** →**Periodic Boundary Conditions**. In this case, any flux *out* of the left hand side of the modelling domain, for example, will be accompanied by an equal flux *in* at the right hand side. One important technical consideration in the implementation of these boundary conditions is that standard boundary conditions still need to be applied to the boundaries under consideration in the **Boundary Settings** dialogue. Specifically, the **Natural Boundary Condition** needs to be specified for all solvers. Examples of Natural Boundary Conditions are given in table C.3.

Once the periodic conditions have been specified, COMSOL does not use the Natural Boundary Conditions, but they must be specified in this way [146]. In the **Source** tab, the variable to be solved for is specified; for example the electron density, n. **COMSOL** conserves the flux here so it is important to specify n here *not* ∇n. COMSOL provides a default name for the constraint variable of the form, pconstr[num], where [num] is the number of the constraint. Next, on the **Destination** tab, the boundary where the coupling is desired is chosen and the same expression in the **Expression** edit field is specified, making sure that the correct pconstr[num] is selected in the drop down **Constraint Name** menu. The addition of **Source Vertices** and **Destination Vertices** proceeds analogously to the **Extrusion Coupling Variables** considered above.

Ordinary differential equations can also be solved using **COMSOL**. An ordinary differential equation has only one variable, as opposed to the *partial* case of more than one. The specific case considered herein is that of the extracted current in the transient photovoltage modelling in dye-sensitised solar cells. Here, a flux boundary condition which depends on the time integral of the flow up to that point in time is used. Specifically, the time-dependent current $j(t)$ is given by

$$j(t) = ek_{ext}\left(n_c(x=0,t) - n_{c,eq}\exp\left(\frac{eV_{oc}}{k_BT}\right)\exp\left(\frac{eQ(t)}{C_{sub}k_BT}\right)\right), \tag{C.11}$$

as described previously, where

Name(u)	Equation	Init(u)	Init (ut)
Q	Qt-OutFlux	0	0

Table C.4: Implementation of an ordinary differential equation.

$$Q(t) = \int_0^t j(t')dt', \tag{C.12}$$

is the amount of charge collected in a time interval, $t = 0 \rightarrow t'$. To implement this, go to **Physics→ ODE Settings**. Table C.4 shows how to enter this in the COMSOL Graphical User Interface.

In table C.4, the far left column defines the variable name (here the integrated current, or charge, $Q(t)$). The next defines the equation to be solved, that is, $\frac{\mathrm{d}}{\mathrm{d}t}\mathrm{Q} - \mathrm{OutFlux} = 0$ and the last two columns give the initial ($t = 0$) values of Q and $\frac{\mathrm{d}}{\mathrm{d}t}Q$ respectively. Note here the use of the **COMSOL** shorthand $Q \equiv \frac{\mathrm{d}}{\mathrm{d}t}\mathrm{Q}$. The variable OutFlux is defined via **Options→ Integration Coupling Variables→ Boundary Variables**, and is set equal to the current density, $j(t)$. Therefore, in summary

$$j(t) = ek_{ext}\left(n_c(x=0,t) - n_{c,eq}\exp\left(\frac{eV_{oc}}{k_BT}\right)\exp\left(\frac{e\int_0^t j(t')dt'}{C_{sub}k_BT}\right)\right). \tag{C.13}$$

Extensive information on all aspects of the implementation of the **COMSOL** software can be found in the electronic and paper documentation which is shipped with it. It is not the aim of this Appendix to supercede this but to summarise the relevant information needed for the modelling of organic and excitonic devices.

References

[1] S. M. Sze. *Physics of Semiconductor Devices, 2nd Edition.* Wiley, Hoboken, NJ, 1981.

[2] J. Nelson. *The Physics of Solar Cells.* Imperial College Press, London, 2003.

[3] A.J. Heeger. Nobel lecture: Semiconducting and metallic polymers: The fourth generation of polymeric materials. *Reviews of Modern Physics*, 73:681, 2001.

[4] C. K. Chiang, C. R. Fincher, Y. W. Park, A. J. Heeger, H. Shirakawa, E. J. Louis, S. C. Gau, and A. G. MacDiarmid. Electrical conductivity in doped polyacetylene. *Phys. Rev. Lett.*, 39:1098, 1977.

[5] B. O'Regan and M. Grätzel. A low cost, high efficiency solar cell based on dye-sensitised colloidal TiO_2 films. *Nature*, 353:737, 1991.

[6] L. M. Peter and D. Vanmaekelbergh. *Advances in electrochemical science and engineering*, volume 6, chapter 2. Wiley-VCH, Weinheim, 1999.

[7] US Department of Energy web site, accessed May 2007, http://www.eia.doe.gov/.

[8] US Department of Energy, Annual Energy Review - July 2006, Accessed May 2007, http://www.eia.doe.gov/.

[9] A. Slaoui and R. T. Collins. Advanced inorganic materials for photovoltaics. *MRS Bull.*, 32:211, 2007.

[10] J. R. Brodrick, US Department of Energy Technical Report, Solid State Lighting Status and Future, 2004, Accessed May 2007, http://www.netl.doe.gov/ssl/PDFs/Brodrick.pdf.

[11] The Solid State Lightning and Display Center of the University of California, Santa Barbara, Accessed May 2007, http://www.ssldc.ucsb.edu/.

[12] M. D. Archer and R. Hill, editors. *Clean Electricity From Photovoltaics*, volume 1, chapter 9, pages 377–445. Imperial College Press, London, 2001.

[13] A. L. Fahrenbruch and R. H. Bube. *Fundamentals of solar cells.* Academic Press, New York, 1983.

[14] D. M. Chapin, C. S. Fuller, and G. L. Pearson. A new silicon p-n junction photocell for converting solar radiation into electrical power. *J. Appl. Phys.*, 25:676, 1954.

[15] D. C. Reynolds, G. Leies, L. L. Antes, and R. E. Marburger. Photovoltaic effect in cadmium sulphide. *Phys. Rev*, 96:533, 1954.

[16] S. E. Shaheen, D. S. Ginley, and G. E. Jabbour. Organic-based photovoltaics: Toward low-cost power generation. *MRS Bull.*, 30:10, 2005.

[17] M. A. Green. Third generation photovoltaics: Ultra-high conversion efficiency at low cost. *Prog. Photovoltaics: Research and Applications*, 9:123, 2001.

[18] W. Shockley and H. J. Queisser. Detailed balance limit of efficiency of p-n junction solar cells. *J. Appl. Phys.*, 32:510, 1961.

[19] J. Nelson. Organic photovoltaic films. *Curr. Opin. Solid State Mater. Sci.*, 6:87, 2002.

[20] C. J. Brabec, J. A. Hauch, P. Schilinsky, and C. Waldauf. Production aspects of organic photovoltaics and their impact on the commercialization of devices. *MRS Bull.*, 30:50, 2005.

[21] L. M. Peter. Dye-sensitised nanocrystalline solar cells. *Phys. Chem. Chem. Phys.*, 9:2630, 2007.

[22] M. Grätzel. Dye-sensitised solid-state heterojunction solar cells. *MRS Bull.*, 30:23, 2005.

[23] B. A. Gregg. Excitonic solar cells. *J. Phys. Chem. B*, 107:4688, 2003.

[24] Lectures on organic polymers given by Alan Heeger at the Johannes Kepler University, Linz, Austria, Accessed May 2007, http://www.ipc.uni-linz.ac.at/os/HeegerLinz.html.

[25] H. Kalman and M. Pope. Photovoltaic effect in organic crystals. *J. Chem. Phys*, 30:585, 1959.

[26] G. A. Chamberlain. Organic solar cells: A review. *Solar Cells*, 8:47, 1983.

[27] C. W. Tang. Two-layer organic photovoltaic cell. *Appl. Phys. Lett.*, 48:183, 1986.

[28] J. J. M. Halls, C. A. Walsh, N. C. Greenham, E. A. Marseglia, R. H. Friend, S. C. Moratti, and A. B. Holmes. Efficient photodiodes from interpenetrating polymer networks. *Nature*, 376:498, 1995.

[29] G. Yu and A. J. Heeger. Charge separation and photovoltaic conversion in polymer composites with internal donor/acceptor heterojunctions. *J. Appl. Phys.*, 78:4510, 1995.

[30] G. Yu, J. C. Hummelen, F. Wudl, and A. J. Heeger. Polymer photovoltaic cells: Enhanced via a network of internal donor-acceptor heterojunctions. *Science*, 270:1789, 1995.

[31] K. M. Coakley and M. D. McGehee. Conjugated polymer photovoltaic cells. *Chem. Mater.*, 16:4533, 2004.

[32] K. M. Coakley, Y. Liu, C. Goh, and M. D. McGehee. Ordered organic - inorganic bulk heterojunction photovoltaic cells. *MRS Bull.*, 30:37, 2005.

[33] G. A. Buxton and N. Clarke. Predicting structure and property relations in polymeric photovoltaic devices. *Phys. Rev. B*, 74:085207, 2006.

[34] US Photovoltaic Industry Roadmap, as at December 2004, US Department of Energy.

[35] M. Reichmuth and C. F. Hünnekes. Monitoring results of the German 100,000 roofs programme. *Proceedings of the 3rd world conference on photovoltaic energy conversion*, page 2115, 2003.

[36] E. F. Schubert. *Light emitting diodes*. Cambridge University Press, Cambridge, 2003.

[37] H. J. Round. A note on carborundum. *Electrical world*, 49:309, 1907.

[38] S. Nakamura, G. Fasol, and S. J. Pearton. *The Blue Laser Diode : The Complete Story, 2nd edition*. Springer, Heidelberg, 2000.

[39] J. H. Burroughes, D. D. C. Bradley, A. R. Brown, R. N. Marks, K. Mackay, R. H. Friend, P. L. Burns, and A. B. Holmes. Light-emitting diodes based on conjugated polymers. *Nature*, 347:539, 1990.

[40] C. W. Tang, S. A. VanSlyke, and C. H. Chen. Electroluminescence of doped organic thin films. *J. Appl. Phys.*, 65:3610, 1989.

[41] C. W. Tang and S. A. VanSlyke. Organic electroluminescent diodes. *Appl. Phys. Lett.*, 51:913, 1987.

[42] M. Pope, H. P. Kallman, and P. Magnante. Electroluminescence in organic crystals. *J. Chem. Phys*, 38:2042, 1963.

[43] Cambridge Display Technology, Cambridge, UK, Accessed May 2007, www.cdtltd.co.uk.

[44] A. P. H. J. Schenning and E. W. Meijer. Supramolecular electronics; nanowires from self-assembled π-conjugated systems. *Chem. Comm.*, page 3245, 2005.

[45] J.-L. Bredas. Conjugated polymers and oligomers: Designing novel materials using a quantum chemical approach. *Adv. Mater.*, 7:263, 1995.

[46] J.-L. Bredas. Relationship between bandgap and bond length alternation in organic conjugated polymers. *J. Chem. Phys.*, 82:3808, 1985.

[47] C. Winder, G. Matt, J. C. Hummelen, R. A. J. Janssen, N. S. Sariciftci, and C. J. Brabec. Sensitization of low bandgap polymer bulk heterojunction solar cells. *Thin Solid Films*, 403-404:373, 2002.

[48] S. R. Forrest. The limits to organic photovoltaic cell efficiency. *MRS Bull.*, 30:28, 2005.

[49] G. L. Araujo and A. Marti. Absolute limiting efficiencies for photovoltaic energy conversion. *Sol. en. mater. sol. cells*, 33:213, 1994.

[50] J. J. M. Halls, J. Cornil, D. A. dos Santos, R. Silbey, D.-H. Hwang, A. B. Holmes, J. L. Brédas, and R. H. Friend. Charge- and energy-transfer processes at polymer/polymer interfaces: A joint experimental and theoretical study. *Phys. Rev. B*, 60:5721, 1999.

[51] B. A. Gregg and M. C. Hanna. Comparing organic to inorganic photovoltaic cells: Theory, experiment and simulation. *J. Appl. Phys.*, 93:3605, 2002.

[52] B. A. Gregg, S. Chen, and R. A. Cormier. Coulomb forces and doping in organic semiconductors. *Chem. Mater.*, 16:4586, 2004.

[53] B. Gregg. The photoconversion mechanism of excitonic solar cells. *MRS Bull.*, 30:20, 2005.

[54] L. M. Peter. Transport, trapping and interfacial transfer of electrons in dye-sensitised nanocrystalline solar cells. *J. Electroanal. Chem.*, 599:233, 2007.

[55] J. A. Barker, C. M. Ramsdale, and N. C. Greenham. Modeling the current-voltage characteristics of bilayer polymer photovoltaic devices. *Phys. Rev. B.*, 67:075205, 2003.

[56] C. M. Ramsdale, J. A. Barker, A. C. Arias, J. D. Mackenzie, and R. H. Friend. The origin of the open-circuit voltage of polyfluorene-based photovoltaic devices. *J. Appl. Phys.*, 92:4266, 2002.

[57] B. A. Gregg. Interfacial processes in the dye-sensitised solar cell. *Coord. Chem. Rev.*, 248:1215, 2004.

[58] M. J. Cass, F. L. Qiu, A. B. Walker, A. C. Fisher, and L. M. Peter. Influence of grain morphology on electron transport in dye sensitized nanocrystalline solar cells. *J. Phys. Chem. B*, 107:113, 2003.

[59] J. Bisquert and V. S. Vikhrenko. Interpretation of the time constants measured by kinetic techniques in nanostructured semiconductor electrodes and dye-sensitised solar cell. *J. Phys. Chem. B*, 108:2313, 2004.

[60] B. C. O'Regan, K. Bakker, J. Kroeze, H. Smit, P. Sommeling, and J. R. Durrant. Measuring charge transport from transient photovoltage rise times. a new tool to investigate electron transport in nanoparticle films. *J. Phys. Chem. B*, 110:17155, 2006.

[61] A. B. Walker, L. M. Peter, K. Lobato, and P. J. Cameron. Analysis of photovoltage decay transients in dye-sensitized solar cells. *J. Phys. Chem. B.*, 110:25504, 2006.

[62] L. M. Peter, Department of Chemistry, University of Bath. Private communication with the author.

[63] A. B. Walker, Department of Physics, University of Bath. Private communication with the Author.

[64] H. K. Dunn, Department of Chemistry, University of Bath. Private communication with the Author.

[65] K. Iwata, T. Tayaka, H. Hamaguchi, A. Yamakata, T. Ishibashi, and H. Karoda. Carrier dynamics in TiO_2 and Pt/TiO_2 powders observed by femtosecond time-resolved near-infrared spectroscopy at a spectral region of 0.9-1.5 microns with the direct absorption method. *J. Phys. Chem. B*, 108:20233, 2004.

[66] B. O'Regan. Influence of the $TiCl_4$ treatment on nanocrystalline TiO_2 films in dye-sensitised solar cells 2: Charge density, band edge shifts, and quantification of recombination losses at short circuit. *J. Phys. Chem. C.*, 111:14001, 2007.

[67] S. Rühle and D. Cohen. Electron tunneling at the TiO_2/substrate interface can determine dye-sensitized solar cell performance. *J. Phys. Chem. B*, 108:17946, 2004.

[68] J. Bisquert, G. Garcia-Belmonte, and F. Fabregat-Santiago. Modelling the electric potential distribution in the dark in nanoporous semiconductor electrodes. *J. Solid. St. Electrochem.*, 3:337, 1999.

[69] Hyperphysics database (Georgia State University) entry on the solution of the LaPlace equation, accessed November 2007, http://hyperphysics.phy-astr.gsu.edu/hbase/electric/laplace.html.

[70] L. M. Peter. Characterization and modeling of dye-sensitized solar cells. *J. Phys. Chem.C*, 111:6601, 2007.

[71] L. Pauling. *The Nature of the Chemical Bond*. Oxford University Press, Oxford, 1952.

[72] Y. Roichman and N. Tessler. Generalised Einstein relation for disordered semiconductors-implications for device performance. *Appl. Phys. Lett.*, 80:1948, 2002.

[73] L. J. A. Koster, E. C. P. Smits, V. D. Mihailetchi, and P.M.W. Blom. Device model for the operation of polymer/fullerene bulk heterojunction solar cells. *Physical Review B*, 72:085205, 2005.

[74] B. K. Crone, P. S. Davids, I. H. Campbell, and D. L. Smith. Device model investigation of single layer organic light emitting diodes. *J. Appl. Phys.*, 84:833, 1998.

[75] B. K. Crone, I. H. Campbell, P. S. Davids, D. L. Smith, C. J. Neef, and J. P. Ferraris. Device physics of single layer organic light-emitting diodes. *J. Appl. Phys.*, 86:5767, 1999.

[76] B. K. Crone, P.S Davids, I. H. Campbell, and D. L. Smith. Device model investigation of bilayer organic light emitting diodes. *J. Appl. Phys.*, 87:1974, 2000.

[77] P. S. Davids, I. H. Campbell, and D. L. Smith. Device model for single carrier organic diodes. *J. Appl. Phys.*, 82:6319, 1997.

[78] D. H. Dunlap, P. E. Parris, and V. M Kenkre. Charge-dipole model for the universal field dependence of mobilities in molecularly doped polymers. *Phys. Rev. Lett.*, 77:542, 1993.

[79] D. Smith, Los Alamos National Laboratory, New Mexico, USA. Private communication, April 2005.

[80] J. C. Scott and G. G. Malliaras. Charge injection and recombination at the metal-organic interface. *Chem. Phys Lett.*, 299:115, 1999.

[81] G. G. Malliaras and J. C. Scott. Numerical simulations of the electrical characteristics and the efficiencies of single-layer organic light emitting diodes. *J. Appl. Phys.*, 85:7426, 1999.

[82] S. Lacic and O. Inganäs. Modeling electrical transport in blend heterojunction organic solar cells. *J. Appl. Phys*, 97:124901, 2005.

[83] H. R. Kerp, H. Donker., R. B. M. Koehorst, T. J. Schaafsma, and E. E. van Faassen. Exciton transport in organic dye layers for photovoltaic applications. *Chem. Phys. Lett.*, 298:302, 1998.

[84] L. A. A. Pettersson, L. S. Roman, and O. Inganäs. Modeling photocurrent action spectra of photovoltaic devices based on organic thin films. *J. Appl. Phys.*, 86:487, 1999.

[85] P. Peumans, A. Yakimov, and S. R. Forrest. Small molecular weight organic thin-film photodetectors and solar cells. *J. Appl. Phys.*, 93:3693, 2003.

[86] A. C. Morteani, P. Sreearunothai, L. M. Herz, R. H. Friend, and C. Silva. Exciton regeneration at polymeric semiconductor heterojunctions. *Phys. Rev. Lett.*, 92:247402, 2004.

[87] P. Langevin. *Ann. Chim. Phys.*, 28:433, 1903.

[88] L. J. A. Koster, V. D. Mihailetchi, and P. W. M. Blom. Bimolecular recombination in polymer/fullerene bulk heterojunction solar cells. *Appl. Phys. Lett*, 88:052104, 2006.

[89] M. G. Harrison, J. Grüner, and G. C. W. Spencer. Analysis of the photocurrent action spectra of MEH-PPV polymer photodiodes. *Phys. Rev. B*, 55:7831, 1997.

[90] R. H. Friend, R. W. Gymer, A. B. Holmes, J. H. Burroughes, R. N. Marks, C. Taliani, D. D. C. Bradley, D. A. Dos Santos, J. L. Bredas, M. Lögdlund, and W. R. Salaneck. Electroluminescence in conjugated polymers. *Nature*, 397:121, 1999.

[91] N. J. Turro. *Molecular Photochemistry*. W. A. Benjamin, New York, 1967.

[92] M. A. Baldo, S. Lamansky, P. E. Burrows, M. E Thompson, and S. R. Forrest. Very high-efficiency green organic light-emitting devices on electrophosphorescence. *Appl. Phys. Lett.*, 75:4, 1999.

[93] A. K. Jonscher. Electronic properties of amorphous dielectric films. *Thin Solid Films*, 1:213, 1967.

[94] C. L. Braun. Electric field assisted dissociation of charge transfer states as a mechanism of photocarrier production. *J. Chem. Phys.*, 80:4157, 1984.

[95] L. Onsager. Deviations from Ohm's law in weak electrolytes. *J. Chem. Phys.*, 2:599, 1934.

[96] L. Onsager. Initial recombination of ions. *Phys. Rev.*, 54:554, 1938.

[97] P. Peumans and S. R. Forrest. Separation of geminate charge-pairs at donor-acceptor interfaces in disordered solids. *Chem. Phys. Lett.*, 398:27, 2004.

[98] N. K. Persson, H. Arwin, and O. Inganäs. Optical optimization of polyfluorene-fullerene blend photodiodes. *J. Appl. Phys.*, 97:034503, 2005.

[99] H. Hoppe, N. Arnold, D. Meissner, and N. S. Sariciftci. Modeling of optical absorption in conjugated polymer/fullerene bulk-heterojunction plastic solar cells. *Thin Solid Films*, 451-452:589, 2004.

[100] I. S. Grant and W. R. Phillips. *Electromagnetism.* Wiley, Chichester, 1999.

[101] C. J. Brabec, A. Cravino, D. Meissner, N. S. Sariciftci, T. Fromherz, M. T. Rispens, L. Sanchez, and J. C. Hummelen. Origin of the open circuit voltage of plastic solar cells. *Adv. Func. Mater.*, 11:374, 2001.

[102] V. D. Mihailetchi, P. W. M. Blom, J. C. Hummelen, and M. T. Rispens. Cathode dependence of the open-circuit voltage of polymer:fullerene bulk heterojunction solar cells. *J. Appl. Phys.*, 94:6849, 2003.

[103] P. M. W. Blom, V. D. Mihailetchi, L. J. A. Koster, and Denis E. Markov. Device physics of polymer:fullerene bulk heterojunction solar cells. *Adv. Mater.*, 19:1551, 2007.

[104] L. J. A. Koster, V. D. Mihailetchi, R. Ramaker, and P. M. W. Blom. Light intensity dependence of open-circuit voltage of polymer:fullerene solar cells. *Appl. Phys. Lett.*, 86:123509, 2005.

[105] H. Hoppe, N. S. Sariciftci, and D. Meissner. Optical constants of conjugated polymer/fullerene-based bulk-heterojunction organic solar cells. *Molec. Cryst. Liq. Cryst.*, 385:113, 2002.

[106] C. M. Ramsdale and N. C. Greenham. The optical constants of emitter and electrode materials in polymer light-emitting diodes. *J. Phys. D. Appl. Phys*, 36:L29, 2003.

[107] H. Hoppe, S. Shokhovets, and G. Gobsch. Inverse relation between photocurrent and absorption layer thickness in polymer solar cells. *Phys. Stat. Solidi: Rapid Research Letters*, 1:R40, 2006.

[108] P. Peumans, S. Uchida, and S. R. Forrest. Efficient bulk heterojunction photovoltaic cells using small-molecular-weight organic thin films. *Nature*, 425:158, 2003.

[109] P. K. Watkins and A. B. Walker. Dynamical Monte Carlo modelling of organic solar cells: Dependence of internal quantum efficiency on morphology. *Nano Letters*, 5:1814, 2005.

[110] C. M. Martin, V. M. Burlakov, and H. E. Assender. Modeling charge transport in composite solar cells. *Sol. en. mater. sol. cells*, 90:900, 2006.

[111] C. M. Martin, V. M. Burlakov, H. E. Assender, and D. A. R. Barkhouse. A numerical model for explaining the role of the interface morphology in composite solar cells. *J. Appl. Phys.*, 102:104506, 2007.

[112] G. A. Buxton and N. Clarke. Computer simulation of polymer solar cells. *Modelling Simul. Mater. Sci. Eng.*, 15:13, 2007.

[113] M. Halim, I. D. W. Samuel, J. N. G. Pillow, A. P. Mankman, and P. L. Burn. Control of colour and charge injection in conjugated dendrimer/polypyridine bilayer LEDs. *Synth. Met.*, 102:1571, 1999.

[114] J. N. G. Pillow, P. L. Burn, I. D. W. Samuel, and M. Halim. Synthetic routes to phenylene dendrimers. *Synth. Met.*, 102:1468, 1999.

[115] M. Halim, I. D. W. Samuel, J. N. G. Pillow, and P. L. Burn. Conjugated dendrimers for LEDs: Control of colour. *Synth. Met.*, 102:1113, 1999.

[116] M. Halim, J. N. G. Pillow, I. D. W. Samuel, and P. L. Burn. Conjugated dendrimers for light-emitting diodes: Effect of generation. *Adv. Mat.*, 11:371, 1999.

[117] M. Halim, J. N. G. Pillow, I. D. W. Samuel, and P. L. Burn. The effect of dendrimer generation on LED efficiency. *Synth. Met.*, 102:922, 1999.

[118] S. G. Stevenson, I. D. W. Samuel, S. V. Staton, K. Knights, P. L. Burn, J. H. T. Williams, and A. B. Walker. Current-voltage characteristics of dendrimer light emitting diodes. Submitted to Organic Electronics, January 2008.

[119] J. P. J Markham, I. D. W. Samuel, S. Lo, P. L. Burn, M. Weiter, and H. Bässler. Charge transport in highly efficient iridium cored electrophosphoresecent dendrimer. *J. Appl. Phys.*, 95:438, 2004.

[120] S. G. Stevenson, Department of Physics and Astronomy, University of St Andrews, Private communication, 2006.

[121] Y. Park, V. Choong, Y. Gao, B. R. Hsieh, and C. W. Tang. Work function of indium tin oxide transparent conductor measured by photoelectron spectroscopy. *Appl. Phys. Lett.*, 68:2699, 1996.

[122] K. Furukawa, Y. Terasaka, H. Ueda, and M. Matsumura. Effect of a plasma treatment of ITO on the performance or organic electroluminescent devices. *Synth. Met.*, 91:99, 1997.

[123] M. Grobosch and M. Knupfer. Charge-injection barriers at realistic metal/organic interfaces: Metals become faceless. *Adv. Mater*, 19:754, 2007.

[124] G. Greczynski, T. Kugler, and W. R. Salaneck. Energy level allignment in organic-based three-layer structures studied by photoelectron spectroscopy. *J. Appl. Phys.*, 88:7187, 2000.

[125] P. A. Tipler and R. A. Llewellyn. *Modern Physics, 3rd edition.* W.H. Freeman, 1999.

[126] S. J. Martin, A. B. Walker, A. J. Campbell, and D. D. C. Bradley. Electrical transport characteristics of single-layer organic devices from theory and experiment. *J. Appl. Phys.*, 98:063709, 2005.

[127] R. U. A. Khan, D. D. C. Bradley, M. A. Webster, J. L. Auld, and A. B. Walker. Degradation in blue-emitting conjugated polymer diodes due to loss of ohmic hole injection. *Appl. Phys. Lett.*, 84:921, 2004.

[128] S. J. Martin, G. L. B. Verschoor, M. A. Webster, and A. B. Walker. The internal electric field distribution in bilayer organic light emitting diodes. *Org. Elec.*, 3:129, 2002.

[129] C. C. Wu, C. I. Wu, J. C. Sturm, and A. Kahn. Surface modification of indium tin oxide by plasma treatment: An effective method to improve the efficiency, brightness, and reliability of organic light emitting devices. *App. Phys. Lett.*, 70:1348, 1997.

[130] X. Crispin, V. Geskin, A Crispin, J. Cornill, R. Lazzaroni, W. R. Salaneck, and J. L. Bredas. Characterization of the interface dipole at organic/metal interfaces. *J. Am. Chem. Soc.*, 124:8131, 2002.

[131] W. Osikowicz, M. P. de Jong, S. Braun, C. Tengstedt, M. Fahlman, and W. R. Salaneck. Energetics at Au top and bottom contacts on conjugated polymers. *Appl. Phys. Lett.*, 88:193504, 2006.

[132] N. Koch, A. Kahn, J. Ghijsen, J.-J. Pireaux, J. Schwartz, R. L. Johnson, and A. Elschner. Conjugated organic molecules on metal versus polymer electrodes: Demonstration of a key energy level alignment mechanism. *Appl. Phys. Lett.*, 82:70, 2003.

[133] K. Murata, S. Cinà, and N. C. Greenham. Barriers to electron extraction in polymer light-emitting diodes. *Appl. Phys. Lett.*, 79:1193, 2001.

[134] K. J. Reynolds, J. A. Barker, N. C. Greenham, R. H. Friend, and G. L. Frey. Inorganic solution-processed hole-injecting and electron-blocking layers in polymer light-emitting diodes. *J. Appl. Phys.*, 92:7556, 2002.

[135] A. K. Thakur, A. K. Mukherjee, D. M. G. Preethichandra, W. Takashima, and K. Kaneto. Charge injection mechanism across the Au-poly (3-hexylthiophene-2, 5-diyl) interface. *J. Appl. Phys.*, 101:104508, 2007.

[136] C. D. J. Blades. *Simulation of organic light emitting diodes.* PhD thesis, University of Bath, 2000.

[137] S. J. Martin. *Simulations of charge transport in organic light emitting diodes.* PhD thesis, University of Bath, 2002.

[138] S. J. Martin, J. M. Lupton, I. D. W. Samuel, and A. B. Walker. Modelling temperature-dependent current voltage characteristics of an MEH-PPV organic light emitting device. *J. Phys. Cond. Mat.*, 14:9925, 2002.

[139] S. C. Lo, N. A. H. Male, J .P. J. Markham, S. W. Magennis, P. L. Burn, O. V. Salata, and I. D. W. Samuel. Green phosphorescent dendrimer for light-emitting diodes. *Adv. Mater*, 14:975, 2002.

[140] O. C. Zienkiewicz and R. L. Taylor. *Finite element method 1: The basics.* Arnold, 2000.

[141] C. J. K. Williams, Department of Architecture and Civil Engineering, University of Bath. Private communication with the author.

[142] D. W. Pepper and J. C. Heinrich. *The finite element method: Basic concepts and applications, second edition.* Taylor and Francis, 2006.

[143] R. W. Lewis, Y. Zheng, and A. S. Usmani. Aspects of adaptive mesh generation based on domain decomposition and Delaunay triangulation. *Finite elements in analysis and design*, 20:47, 1995.

[144] COMSOL User's Guide.

[145] D. S. Burnett. *Finite Element Analysis: From concepts to applications.* Addison-Wesley, Reading, MA, 1987.

[146] Private communication with COMSOL technical support, September 2005.

[147] H. Hoppe, N. Arnold, N. S. Sariciftci, and D. Meissner. Modeling the optical absorption within conjugated polymer/fullerene-based bulk-heterojunction organic solar cells. *Solar energy Materials and Solar Cells*, 80:105, 2003.

[148] COMSOL RF Module User's Guide.

[149] T. A. Davis. *Direct methods for sparse linear systems.* SIAM, Philadelphia, PA, 2006.